Computational Studies of Novel Phenomena on the Surface of Graphite

by

Mohammed Salah Mohammed Moaied

Supervised by

Juan José Palacios

Departamento de Física de la Materia Condensada, Facultad de Ciencias

Universidad Autónoma de Madrid

This dissertation is submitted for the degree of

Doctor of Philosophy in Science of Physics

Faculty of Science

Madrid, 2014

I would like to dedicate this thesis to my loving parents ...
for their unending support and encouragement

“What I cannot compute, I do not understand”

(adapted from Richard P. Feynman)

Acknowlegements

And I would like to thank all of my family, friends, and collaborators who have been a part of my life. You have not only made it possible for me to complete graduate school and my dissertation, but also made it a personally and professionally rewarding part of my life.

My advisor, Dr. **Juan José Palacios**, has dedicated enormous energy and countless hours to helping me through every step of my dissertation. His advice and encouragement have been unending and invaluable, guiding me to define the direction of my research. His attention to detail has helped me hone my ideas and improve the quality of my dissertation.

I also would like to thank Dr. José Soler, Dr. Felix Yndurain, and Dr. José Vicente Álvarez, Ivan Brihuega, and all the staff in the Departamento de Física de la Materia Condensada has also been invaluable during my time at Universidad Autónoma de Madrid. I consider each of them my friends and colleagues; their daily support has kept me grounded and focused during my work.

I also would like to thank Dr. María José Caturla, and Dr. Carlos Untiedt Lecuona Universidad de Alicante for their cooperation and support has kept me grounded and focused during my work.

Special thanks to my colleagues Guillermo Román-Pérez, Michelle Fritz, María Soriano, and Carlos Salgado for their support to complete my work.

All the staff in the Departamento de Física de la Materia Condensada has also been invaluable during my time at Universidad Autónoma de Madrid. I consider each of them my friends and colleagues; their daily support has kept me grounded and focused during my work.

I would like to thank Dr. Abdul Rahman Al-Dali, Dr. Ahmed Al-Falki, Dr. Said Mazen, Dr. Mohammad Al-Ghazali, and Dr. Asmaa Fahim at Faculty of Science, Zagazig University they opened the door for me to research in physics. The knowledge and the way of conducting scientific research I learned from them are invaluable and priceless.

This work was funded by grants from the Spanish Ministry of Science and Innovation (MICINN) and the Ministry of Education through grant F1S2009-12721.

I would like to thank Ehab Yousef, Safwat, Fouad Zahran, Walid Fouad, Hitham Al-ashry, Hitham Elhosiny, Yasmin khairy, Ehab Ahmed, Khaled Hassanein, Adel Mady, Youssef Ra-

madan and all my friends in Spain who make me feel like I'm in my own home.

Also, I would like to thank my dear friends living in Egypt Ahmed Zaki, Ayman Saber, Mohamed Desoky, Mohamed Madkour, Mohamed Samier, Mohamed Srour, Ahmed Faid, Hitham Gouda, and Mohamed Nasr for their continuous encouragement to make it possible to write this dissertation.

Lastly, and most importantly, I wish to thank my wonderful family, My Father, My Mother, My brothers Osama, Ashraf, Ahmed, and my lovely sister Enas, the completion of this work would not have been possible without your encouragement, love and support. Thanks for provided me with so many great memories, opportunities and experiences.

I've left off many important friends and family members in order to keep these acknowledgements shorter than the remainder of my dissertation, so a special thank you to the rest of the people who have been important in my life throughout my education.

Abstract

Using a first-principle calculation within Density Functional Theory, we investigate the effect of external static charge on the graphite flakes structure. As a result, the charges relocate and repulsive forces are generated, in compliance with classical theories. Even more remarkable is that the Coulomb repulsion exfoliates the graphene layers from both surfaces of a positively charged graphite slab. Once the charging exceeds a threshold value, the outermost layers are exfoliated. This result is used to develop a method for intact exfoliation of graphene. Modeling a process of electrostatic exfoliation requires, in principle, a non-equilibrium calculation since the STM tip induces charges on the surface of graphite. Alternatively one can use equilibrium calculations and simple electrostatic models as we explain here.

We calculate the electronic structure and magnetic properties of hydrogenated graphite surfaces using van der Waals density functional theory and model Hamiltonians. We find, as previously reported, that the interaction of hydrogen atoms on graphene single-layer favors adsorption on different sublattices along with an antiferromagnetic coupling of the induced magnetic moments. On the contrary, when hydrogenation takes place on the surface of graphite or graphene multilayer (Bernal stacking), the interaction between hydrogen atoms competes with the different adsorption energies for different sublattices. This translates into ferromagnetism for low concentrations. Based on the exchange couplings obtained from the DFT calculations, we have also evaluated the Curie temperature through a Ising-like model. Remarkably, the long-range nature of the magnetic coupling in these systems makes the Curie temperature size dependent and easily larger than room temperature.

We present a theoretical study of the different mechanisms resulting in the sublattice selective adsorption of atomic hydrogen on graphite surfaces. First, through density functional theory calculations, we obtain the desorption energy barriers and the diffusion energy landscape for a single hydrogen atom on a graphene bilayer. Second, we perform kinetic Monte Carlo simulations to study the evolution of a random distribution of H atoms on the surface. The calculated desorption and migration barriers along with the energetics of H pairs on single layer graphene are used as ingredients in the simulations. These reveal that the time scale for all the atoms to redistribute on the same sublattice is of the order of seconds and much

shorter than typical desorption rates at room temperature. This translates into an spontaneous sublattice unbalanced distribution of adsorbed H, as recently observed experimentally.

Resumen

El uso del primer principio de cálculo de la Teoría Funcional de la Densidad, hemos investigado el efecto de la carga estática externa de la estructura de las escamas de grafito. Como resultado, la reubicación de las cargas y la generación de la fuerza de repulsión están en conformidad con las teorías clásicas. Aún más notable es que la repulsión de Coulomb exfolia las capas de grafeno de ambas superficies de carga positiva de las de grafito. Una vez que la carga excede un valor de umbral, las capas más externas son exfoliadas. Este resultado se utiliza para desarrollar un método para la exfoliación intacta de grafeno.

Calculamos la estructura electrónica y propiedades magnéticas de la superficie de grafito hidrogenados utilizando van der Waals Teoría Funcional de la Densidad y modelos hamiltonianos. Hemos obtenido, como se informó anteriormente, que la interacción de los átomos de hidrógeno en el grafeno de una sola capa favorece la adsorción en diferentes sub-retículas junto con un acoplamiento antiferromagnético de los momentos magnéticos inducidos. Por el contrario, cuando el hidrogenación tiene lugar en la superficie de grafito o de múltiples capas de grafeno (Bernal de apilamiento), la interacción entre átomos de hidrógeno compite con las diferentes energías de adsorción para diferentes sub-retículas. Esto se traduce en ferromagnetismo para bajas concentraciones. Basado en los acoplamientos de cambio obtenidos a partir de los cálculos DFT, también hemos evaluado la temperatura de Curie a través de un modelo de Ising-like. Sorprendentemente, la naturaleza de largo alcance del acoplamiento magnético en estos sistemas hace que el tamaño de la temperatura de Curie dependa y sea fácilmente mayor que la temperatura ambiente.

Se presenta un estudio teórico de los diferentes mecanismos que resultan de la adsorción selectiva subred de los atomos de hidrógeno sobre la superficie de grafito. En primer lugar, a través de cálculos de la teoría funcional de la densidad, se obtienen las barreras de energía de desorción y el panorama energético de difusión para un solo átomo de hidrógeno sobre una bicapa de grafeno. En segundo lugar, realizamos las simulaciones de cinético de Monte Carlo para estudiar la evolución de una distribución al azar de los átomos de H en la superficie. La desorción y migración de las barreras calculadas junto con la energía de pares de H en grafeno de una sola capa, se utilizan como ingredientes en las simulaciones. Estos revelan que la escala

de tiempo para todos los átomos para redistribuir en el mismo subred en orden de segundos y mucho más corto que las tasas de desorción típicos a temperatura ambiente. Esto se traduce en una distribución expontanea de subred que desequilibrada la adsorción H, como se observó recientemente en el experimento.

Publications and Conferences

Publications included in this thesis

- "Atomic-scale selective adsorption of atomic hydrogen: a simple route towards magnetizing graphene layers"
  Iván Brihuega, Miguel M. Ugeda, Mohammed Moaied, Héctor González-Herrero, José M. Gómez-Rodríguez, Juan-José Palacios.
  Departamento Física de la Materia Condensada, Universidad Autónoma de Madrid, E-28049 Madrid, Spain.

- "Hydrogenation-induced ferromagnetism on graphite surfaces"
  Mohammed Moaied, José Vicente Álvarez, and Juan-José Palacios.
  Departamento Física de la Materia Condensada, Universidad Autónoma de Madrid, E-28049 Madrid, Spain.

- "A theoretical study of diffusion and desorption processes of atomic hydrogen on graphite surfaces"
  Mohammed Moaied, María José Caturla, and Juan-José Palacios.
  Departamento Física de la Materia Condensada, Universidad Autónoma de Madrid, E-28049 Madrid, Spain.

- "Graphene Exfoliation from Graphite Layers"
  Carlos Untiedt Lecuona, Mohammed Moaied, María José Caturla, and Juan-José Palacios.
  Departamento Física de la Materia Condensada, Universidad Autónoma de Madrid, E-28049 Madrid, Spain.

Publications not included in this thesis

- "Stability, Adsorption, and Diffusion of CH_4, CO_2, and $\mathbf{H}_2$ in Clathrate Hydrates"
  Román-Pérez, Guillermo and Moaied, Mohammed and Soler, Jose M. and Yndurain, Felix
  Phys. Rev. Lett. 105, 145901 (2010)

Conference contribution

- First-Principles Computational Methodologies for 2D Materials
  Date: 14-16 September, 2011
  Place: Lancaster University, United Kingdom.

- Graphene for Future Emerging Technologies
  Date: 18 October, 2011
  Place: CSIC auditorium, Madrid, Spain.

- 1st Workshop on Fabrication and Properties of Nanostructures
  Date: 8-9 November, 2012
  Place: Universidad de Alicante, Alicante, Spain.

Contents

List of Figures

List of Tables

Nomenclature

Greek Symbols

$\imath$	unit imaginary number $\sqrt{-1}$
π	$\simeq 3.14\ldots$

Acronyms / Abbreviations

T_c	Curie temperature
AFM	Antiferromagnetic
BZ	Brillouin Zone
DFT	Density function theory
DOS	density of states
FM	Ferromagnetic
GGA	generalized gradient approximation
HF	Hartree-Fock
HK	Hohenberg-Kohn
HOPG	Highly oriented pyrolytic graphite
KS	Kohn-Sham
LDA	local density approximation
MP	Monkhorst-Pack
OKMC	Kinetic Monte Carlo

PBE Perdew-Burke-Ernzerhof

TB Tight-Binding

vdW van der Waals

Chapter 1

Introduction

Carbon is a chemical element with symbol C, is the sixth element in the periodic table, and is listed at the top of the sixth column, ranks twelfth in order of natural abundance. Each carbon atom has six electrons with the electronic configuration $1s^2, 2s^2, 2p^2$ [1]; in this way the carbon atom is defined.

Carbon is an element of multi-faces, why?
In the carbon atom the $1s$ orbital contains two strongly bound electrons, and they are called the core electrons. However, the four electrons in $2s$, and $2p$ orbitals are more weakly bound electrons called valence electrons. Since the energy difference between the $2s$, and $2p$ energy levels in carbon is small compared with the binding energy of the chemical bonds, this gives the carbon the ability for mix the electronic wave functions for these four electrons, thereby changing the occupation of the $2s$ and three $2p\,(2p_x, 2p_y, 2p_z)$ atomic orbitals which is called hybridization, whereas the mixing of a single $2s$ electron with i=1, 2, 3 $2p$ electrons is called sp^i hybridization [1–3]. In carbon the three possibilities hybridizations are available; sp^1, sp^2, and sp^3 orbitals, as shown in figure (1.1).

This in turn gives carbon the ability to adapt into various molecular and crystalline structures. There are different forms of pure carbon, called allotropes, which have very different bonding structures the nature of these bonds underlies the varied chemical properties and physical properties of the carbon allotropes. Moreover, carbon has an ability for bonding with other small atoms, including other carbon atoms, and is capable to form multiple stable covalent bonds with such atoms. As a result, carbon is known to form almost ten million different compounds; the large majority of all chemical compounds [3].

The two main allotropes forms of carbon are graphite, and diamond. The stable bonding form of carbon atom at ambient condition is graphite, while under application of high pressure and high temperature a transformation to the diamond structure occurs as shown in figure (1.2),

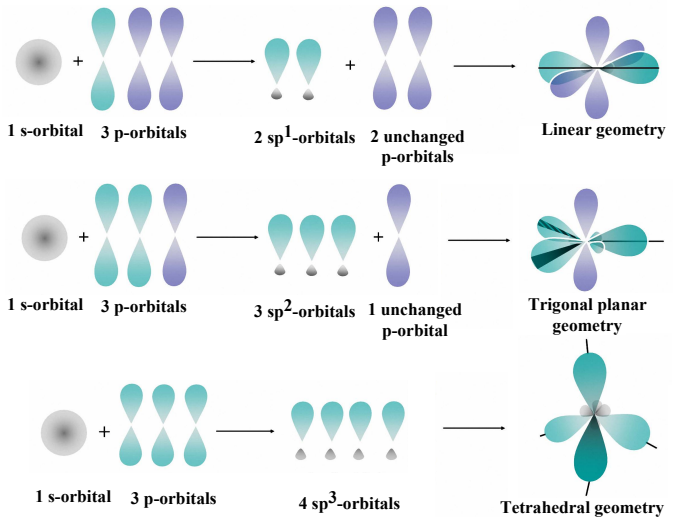

Fig. 1.1 Hybridization of carbon atom expressed as a combination of atomic orbitals.

with an energy difference between the graphite and the diamond of ≈ 0.02 eV per atom. Due to the high energetic barrier between the two phases of carbon, the transition from diamond to the most stable phase of graphite at normal conditions is extremely slow [4, 5]. The electron mobility in diamond is only 1800 cm^2/V-s were as the in-the plane graphite electron mobility is 20×10^3 cm^2/V-s. The band gap in diamond is 5.47 eV while in semi-metallic graphite is only -0.04 eV.

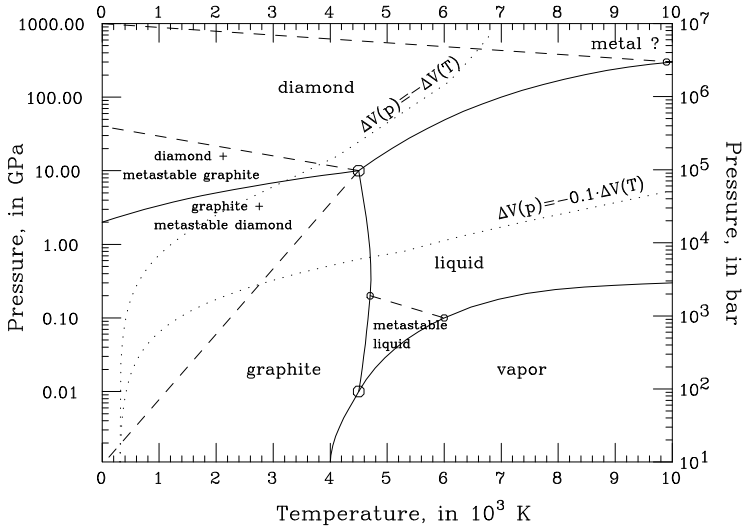

Fig. 1.2 Phase and transition diagram for carbon

The phase diagram (p,T) of carbon was controversial for many years, and only recently well-established experimentally - up to now, within the temperature range up to about 10000 K and the pressure range up to about 100 Gpa; the higher region being still poorly understood. The diagram is shown in Figure (1.2), as based on [6]. Carbon has the highest melting and sublimation point of all elements. At atmospheric pressure it has no actual melting point as its triple point is at 10 MPa (100 bar) [7, 8] so it sublimates above 4000 K [6, 9]. Carbon sublimes in a carbon arc which has a temperature of about 5800 K. Thus, irrespective of its allotropic form, carbon remains solid at higher temperatures than the highest melting point metals such as tungsten or rhenium. Although thermodynamically prone to oxidation, carbon resists oxidation more effectively than elements such as iron and copper that are weaker reducing agents at room temperature.

1.1 Crystalline forms of carbon

1.1.1 Diamond

Diamond has a crystalline structure where each sp^3 carbon atom is bonded to four others in a tetrahedral arrangement by σ-bonds, each at an angle of 109.5° to the other [10]. The tetrahedral bonding characteristic of the diamond structure is shown in Figure (1.3).

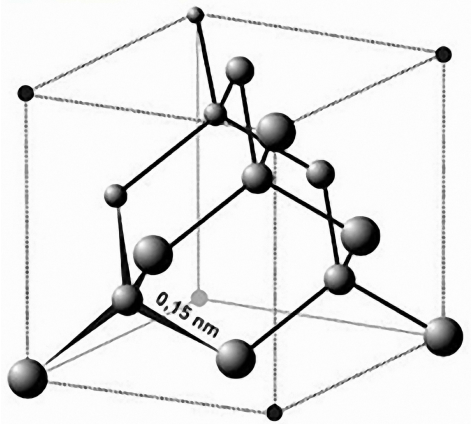

Fig. 1.3 Diamond structure

Diamond is one example of a structure that satisfies this bonding arrangement. The symmetry of the diamond lattice is cubic and the atom arrangement can be described by two face-centered cubic (fcc) lattices with one lattice displaced by one-quarter of the unit cell (a = 0.3567 nm) along the [111] direction [11]. As it is shown the diamond structure is relatively

empty; the maximum proportion of the available volume which may be filled by hard spheres is only 0.34. The diamond structure is an example of directional covalent bonding with lattice constant 0.3567 nm [11]. The crystalline network gives the diamond its hardness and excellent heat conduction properties. The band structure of diamond is characterised by a large energy gap of 5.5 eV between valence band maximum and the conduction band minimum. This makes it, in the undoped case, an insulator with a resistivity of $\sim 10^{20}$ Ω.cm at room temperature. The sp^3 hybridized bonds account for its electrically insulating property and optically transparent [10]. The large carrier mobility and the thermal properties make diamond an interesting material for electronic applications [12, 13].

1.1.2 Graphite

The word graphite means in Greek (to write). Graphite is a soft black carbon based mineral, naturally occurring. Graphite is a stacked structure of layers wherein each layer has a hexagonal lattice structure of carbon atoms. The layers are stacked parallel to each other, and perpendicular to the principal axis (C-axis) in a tetragonal or hexagonal structure. The layer is constructed in a planar hexagonal network, constituted by a honeycomb lattice of sp^2-hybridized carbon atoms. The chemical bonds within the layer are covalent bonds with sp^2 hybridization; each hexagonal form 6 σ-bonds and the remaining p-orbitals, which are at right angles at the layer planes, no take part in σ-hybridization. The p-orbitals of two neighbouring carbon atoms overlap sideways and form π-orbitals [14]. The bond length between each carbon 0.142 nm, with an angle 120° from its three nearest neighbours, and the lattice unit vector a= 0.246 nm [14], as shown in Figure (1.4 - from ref. [15]). These bonds are very short and extremely strong in the plane (in compared with the long bonds in diamond which are 0.154 nm).

Therefore, a single-layer graphite is stronger than diamond. An isolated graphitic layer is known as graphene, and it has longer bonds with C-C bond length of 0.144 nm, and the lattice unit vector a= 0.249 nm. The remaining electron $2p_z$ plays a role in the binding inter-planar (these longer σ bond such as very weak) and forming the co-planar π-bonds are delocalized, hence providing a donor site for the electrical and thermal conductivity. The interaction of the delocalized π electrons with light causes the graphite appear black [16]. The forces that hold the layers together and keep them parallel consist of van der Waals forces (weak electrostatic attraction) as well as some loose overlap of the $2p_z$ orbitals perpendicular to the planer layers [17]. This mechanism is what the graphite layers are easily moved past each other; thereby causing some of the outward characteristics, such as it being a soft, highly durable, low fric-

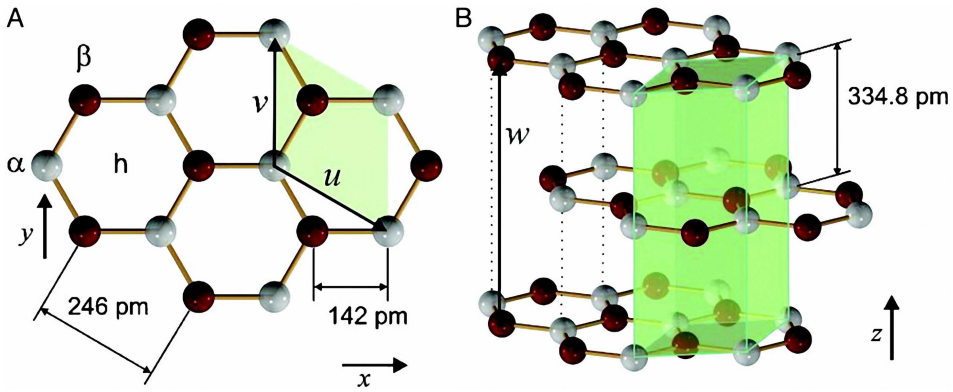

Fig. 1.4 Crystal structure of graphite. The unit cell is shaded in green. (A) Top view on the surface layer. (B) Perspective view, showing the layered structure. The α-atoms (white); the β-atoms (red). The unit vector w is parallel to the z-axis with a length of 669.6 pm.

tion, slippery, opaque and electrically semiconducting material in most common environments [10]. Therefore, graphite is an excellent material for use in Pencils, in high temperature industrial applications, and as a dry lubricant. The normal structure of graphite is the AB stacking sequence honeycomb layers with an average inter-planar distance $\frac{1}{2}$c= 0.33539 nm. Graphite is a hexagonal structure with D_h^6 symmetry was apparently first proposed by Hull in 1917 [18]. Graphite was one of the first materials studied by X-ray diffraction. Bernal et. al. [19] using the X-ray diffraction, to determine a graphite structure is actually hexagonal planes are in a planar stacking sequence (ABABA...), henceforth called Bernal stacking, which, when Flat has a space group $P6_3/mmc$ [20]. The atomic sites in Bernal stacked graphite in fractions of a unit cell dimensions are a, b, and c, see Figure (1.4). The AB stacked unit cell is almost twice the volume of the simple hexagonal stacking AA [17, 21, 22].

1.2 Graphite Properties

The density of states (DOS) of graphite, is shown in Figure (1.5). Near the Fermi level, the DOS consists exclusively of delocalized π-electrons. These states are related directly to the presence of sp^2-bonded carbon and spectral weight in photoemission spectra context, e.g. the determination of the proportion of sp^2-bonded carbon, amorphous carbon [23].

The two-dimensional dispersion relation for the π-electron system are calculated within the tight-binding approximation [24], as shown in Figure (1.6 - from ref. [25]). If the interaction between the graphite layers neglected (treatment of a single layer of graphite called graphene), the DOS at the Fermi level E_F equal to zero. This is due to the fact that the π-bands

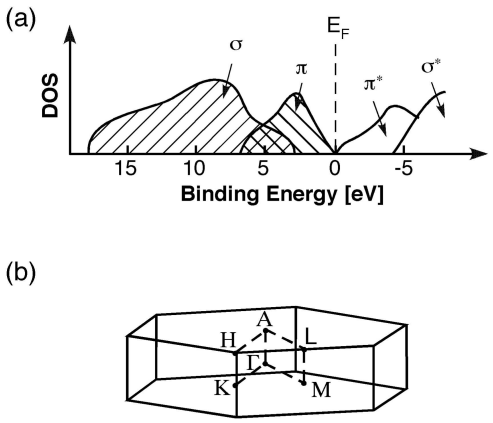

Fig. 1.5 (a) Schematic representation of the DOS of graphite showing the energy position of the π- and σ-derived states relative to the Fermi level E_F. (b) First Brillouin zone of graphite showing the special points in the reciprocal lattice.

occupied, and the vacant π-bands touching only at the corners of the first Brillouin zone, at points called the **K** points, this making the graphene zero bandgap. The Fermi-surface in this case consists of six **K** points. The occupied and the unoccupied π-bands are symmetrical with respect to the Fermi energy E_F. The hexagon shown displays the two-dimensional Brillouin zone and defines the plane with $E = E_F$. The overlap of the π-orbitals on adjacent atoms of the same layer is the reason for the shift of π-states and is responsible for the high charge carrier mobility in graphite.

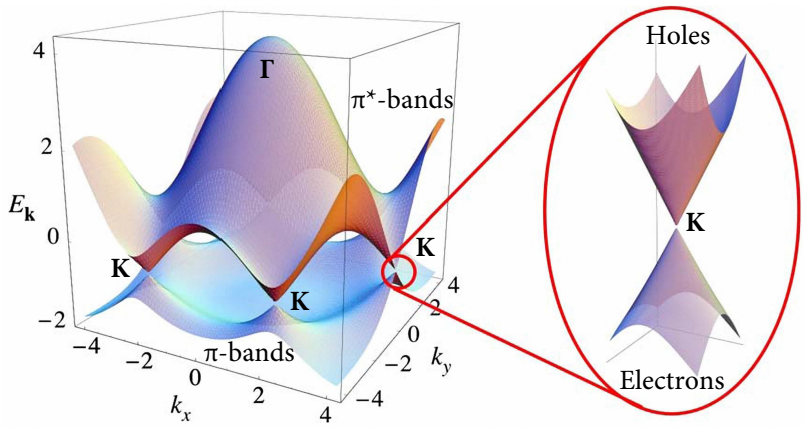

Fig. 1.6 Band dispersion of the occupied and unoccupied π-bands in the first Brillouin zone of the honeycomb lattice.

However, the description of the graphene is not sufficient in order to understand the properties of three-dimensional graphite, particularly with regard to the π-states at the Fermi level.

The weak interlayer bonding of graphite, which is often mistakenly referred to as Van der Waals bond, comes from the small overlap of the π-orbitals between atoms of adjacent layers. As a result, two types of atoms as stacked in the ABA graphite, only one half of the atoms, known as α-atoms are arranged on an atom of the adjacent layer. The result of the electronic structure is that the degeneracy of the π-band is raised.

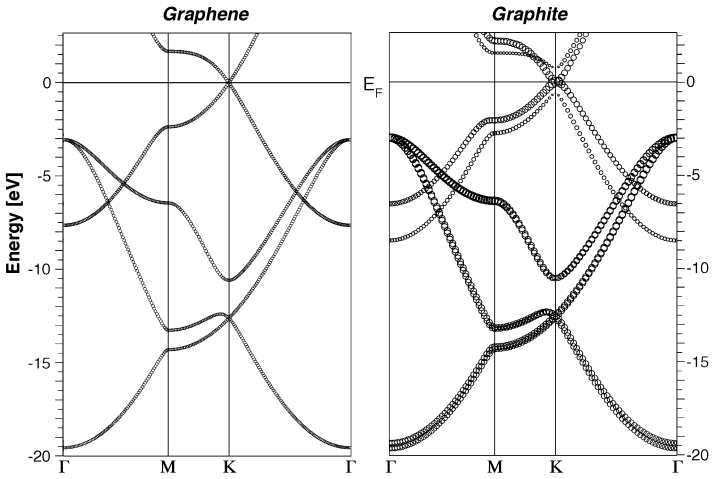

Fig. 1.7 Band structure of graphite and graphene as calculated using the WIEN code.

Figure (1.7) shows band structure calculations for different distances between adjacent graphene layers. The calculation was performed with the WIEN97 code [26] using the generalized gradient approximation (GGA). Calculating with a large distance between the layers of 8 Å is obtained, the band structure of two-dimensional graphite, that is, the interaction between adjacent layers can be neglected, and to touch the occupied and unoccupied π-bands only at the corners of the Brillouin zone. However, when the distance layer with a graphite (3.35 Å), the interaction between the π-electrons of the subsequent layers as the reducing splitting of the bands at the most for the π-band observed pronounced. The size of the graphite marker in the bandplot was selected character around the band with respect to the load value that reflects from the β-atom. This figure shows that only the π-electrons that with respect to the β-atoms to the DOS near the Fermi level E_F. The bands associated with the α-atom showing an energy gap of $\sim$1.4 eV at **K** point. The remaining bands show a slight overlap of 40 meV at the **K**-points and transform the Fermi surface of the graphene for six points in six small pockets around the **K** points for three-dimensional graphite. It is this small π-electron interaction between the adjacent layers of the three-dimensional semi-metal is graphite. The large asymmetry between the π-band related to the α and β-atoms observed in the real space and charge distribution. For probes that are sensitive to the local density of states (LDOS) near

the E_F, such as STM, maxima in the tunneling current are exclusively detected in the β-atoms.

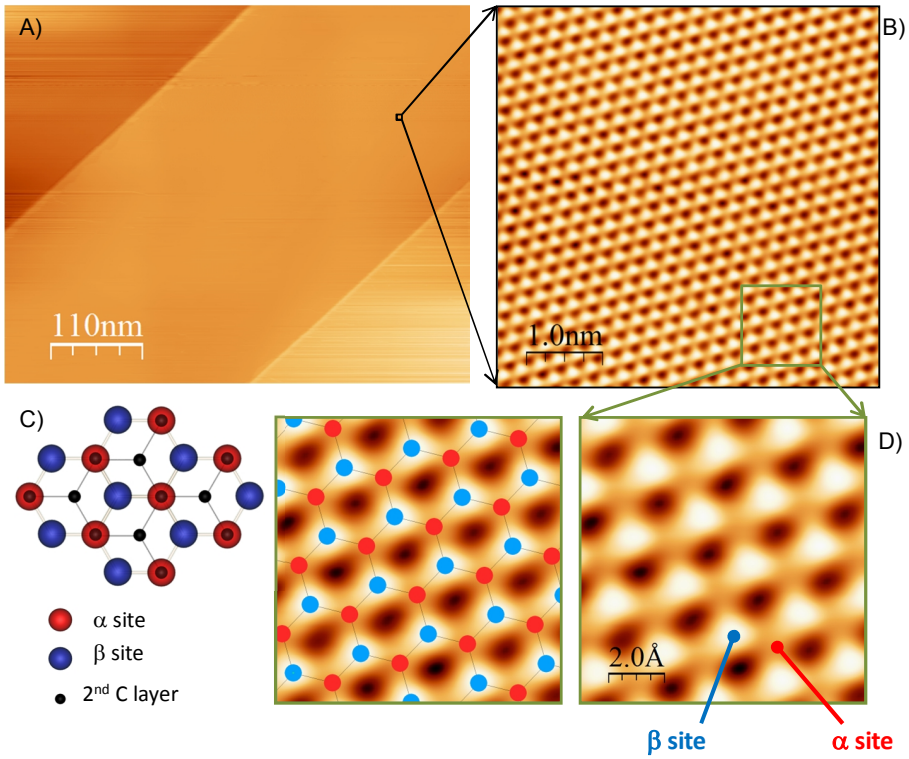

Fig. 1.8 General morphology of the pristine graphite surface. A) Large scale overview measured at 6K. Size 570×470nm^2. B) 5x5nm^2 zoom in to atomically resolved the outlined square region. C) Schematic diagram of the graphite structure. D) 1×1 nm^2 STM image to show the difference intensity of a and b sites.

An experimental current image in Figure (1.8), which was recorded by Ivan Brihuega et. al., they use highly ordered pyrolytic graphite (HOPG) samples, which present the AB Bernal stacking. Thus, at the surface, one atom of the honeycomb unit cell (α) is located directly above a C atom of the second layer and the other one (β) is on top of a hollow site (see Fig. 1.8-C). Instead of the hexagonal structure expected from the honeycomb arrangement of the carbon atoms in a layer, a trigonal symmetry consisting of maxima in the tunneling current observed on every second atom only is imaged (see Fig. 1.8-D). Figure (1.8-D), show high resolution STM images of the HOPG surface where both atoms of the honeycomb lattice are resolved; the one on β site showing a higher intensity than the one on α site. This intensity difference between both sites is due to the presence of the underlying carbon atom, which decreases the DOS at the Fermi Energy of α sites [27].

Figure (1.9), shows the calculation of the LDOS using the WIEN97 code [26]. In order to

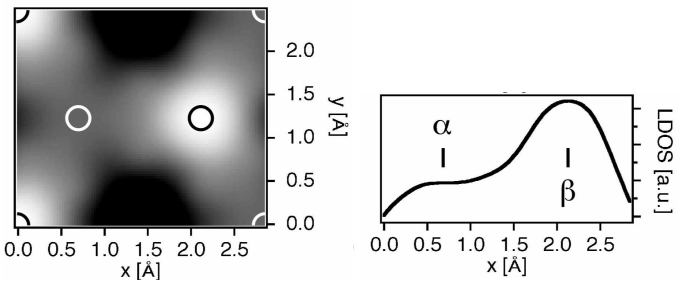

Fig. 1.9 LDOS calculated with WIEN.

simulate the surface of a supercell, they used two graphene layers of 3.35 Å separate and 12 Å of the empty space. This allows the calculation of the LDOS at a typical STM on the surface.

The results show that the interlayer interaction results in a very low DOS near E_F, which is positioned at the position of the α-atoms. For lower bias voltages, i.e., a further limitation of the energy difference to the E_F states probed in the scan, the asymmetry between α- and β-atoms becomes even clearer. The calculated density plot for states with a binding energy of $E_B \leq 150$ meV, yields a LDOS on the α atoms, which is even lower than the center of the hexagon, where no atom exists.

1.3 Defects in Graphite

Although a number of techniques probing graphite, a number of imperfections found in graphite. The most common defects found in a very perfect graphite flakes materials are dislocations, tilt, and twist boundaries [21]. A dislocation line extends along the core of the dislocation, wherein the distortion with respect to the perfect lattice is greatest. There are two basic types of dislocations about a dislocation line in a solid. One type is edge dislocation and the other type is a screw dislocation. The Burgers vector indicates the type of dislocation, since they quantify the amount and direction of the dislocation of the lattice distortion in a crystal lattice. An edge dislocation has its Burgers vector perpendicular to the dislocation line. Second, in a screw dislocation, the Burgers vector parallel to the dislocation line [28]. The four possible extended dislocations in graphite, are classified by [29]:

1. Screw dislocation line in the basal layer.
2. Edge dislocation line in the basal layer.
3. Edge dislocation line parallel to the hexagonal principal axis (c-axis).

4. Dislocation line and Burgers vector in non-basal directions.

The dislocation structures in graphite have been thoroughly investigated. Many dislocations are observed in the basal layers and appear in pairs, as shown in Figure (1.10 - from ref. [30]). each member of the pair is a partial dislocation and the total is $\frac{1}{3}a\langle 11\bar{2}0\rangle$.

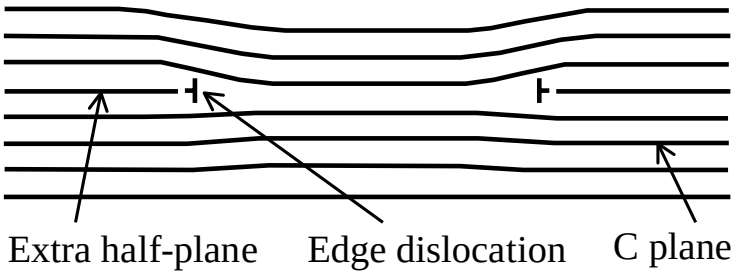

Fig. 1.10 Schematic of dislocations facing each other.

The separation between the partials varies from approximately 50-100 nm. The simple straight split dislocation can be found in edge or screw orientation. The partial dislocations repel each other, but the stacking fault between them amounts to an opposing force. The stacking fault partials is enclosed, in fact, in a region of the crystal stack of ABC structure, which can be best described by a rhombohedral unit cell. Features of the rhombohedral crystal structure, if apartment has a space group $R\bar{3}m$ [20], are sometimes seen in X-ray diffraction [21, 22].

Non-basal dislocations can lead to macroscopic structural features and can be examined by optical microscopy. The non-basal dislocations are present in graphite with a density in the range of 10^{-3} - 10^{-5} per cm^2. A number of studies have shown the existence of screw dislocations parallel to the c-axis of hexagonal with dislocation lines, as shown in Figure (1.11). A special feature of these dislocations is that they have large Burgers vectors 15-100 nm [21].

The last type of impurity to discuss is a local or point defect. Lattice vacancies and interstitial atoms in graphite were investigated. Another class of local defects are topological defects, pentagon and combinations include heptagon, although only the combinations that can not induce a significant curvature allowed failures in the basal layers in graphite crystals. The behavior of point defects completely described by its formation energy and entropy, and energy, and the entropy of movement of the defect in the grid. The energies of a single vacancy and interstitial are shown in Table (1.1 - from ref. [31]). The energy transfer in the formation of a di-vacancy of two individual points is about 5 eV [21], as shown in Figure (1.12 - from ref. [32]).

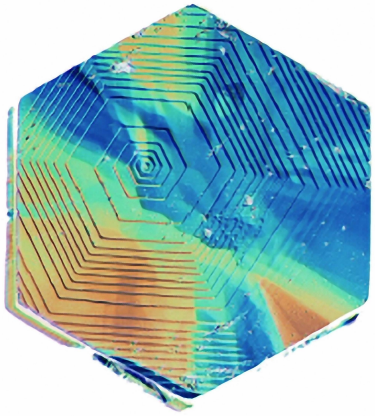

Fig. 1.11 A graphite crystal with a screw dislocation, from Dr. John Jaszczak of the Dept. of Physics at Michigan Technological University.

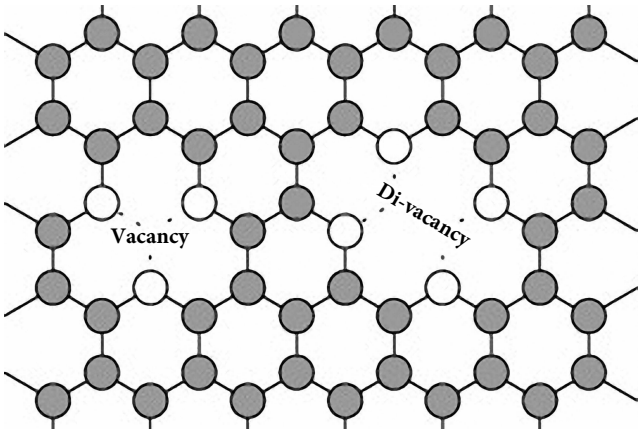

Fig. 1.12 The vacancy and di-vacancy in a graphite layer.

Table 1.1 Defect formation and migration energies in graphite.

Energy	Vacancy (eV)	Interstitial (eV)
formation	7.0 ± 0.5	7.0 ± 1.5
basal plane motion	3.1 ± 2.1	< 0.1
c-axis motion	> 5.5	> 5.0

Theoretical investigations of vacancies in graphite are an important and essential contribution to the understanding of the fundamental processes and complex defect in these materials. Embedded clusters with complete neglect of differential overlap (CNDO)-theory level [33], extended Huckel with a semi-empirical valence effective Hamiltonian [34], a tight-binding model interatomic potential [35], and first principles theory with local density functional theory [36, 37], and Hartree Fock method [38], have been applied only to the symmetric vacancy of graphite. Using tight binding molecular dynamics simulations at 2000 K Krasheninnikov et al [39]. Recently, using spin-polarized DFT (density functional theory), Ma et al [40]. they claimed that the vacancy is magnetic. Applying the same method, Lehtinen et al [41]. reported the magnetic properties of vacancies and the vacancy-hydrogen complex.

1.4 Methods of graphite exfoliation

Making artificial material from graphite (Graphene), how? The bonding forces between graphite layers are much weaker than the bonding between the carbon atoms within the layers. The carbon atoms within each sheet of graphene are bonded together via strong covalent bonds, while in graphite those sheets are held together by van der Waals (dipole- dipole) forces, which are much, much weaker. Because graphite is more weakly bound between the layers of carbon atoms, these layers can easily be broken and separate the different layers from a bulk sample. Experimentally, exfoliation of graphite has been investigated and realized by using various techniques, including chemical/solution, mechanical, and thermal methods [42–61]. In the exfoliation methods one should keep in mind important factors when considering the proficiency of any synthetic route graphene. First, the process must produce high quality in the 2D crystal lattice. Second, the method must provide that the layer be kept apart after separation.

1.4.1 Mechanical exfoliation

Mechanical exfoliation is the production process, which leads to product the first isolation of a graphene sample [62]. In addition to its historical importance, a mechanical exfoliation is still extremely valuable. Particularly in academic research there is applied a widely used technique because the resulting sample quality is still unmatched by any of the newer techniques. The conceptual simplicity of this technique, which is also referred to as the 'scotch-tape method', as shown in Figure (1.13).

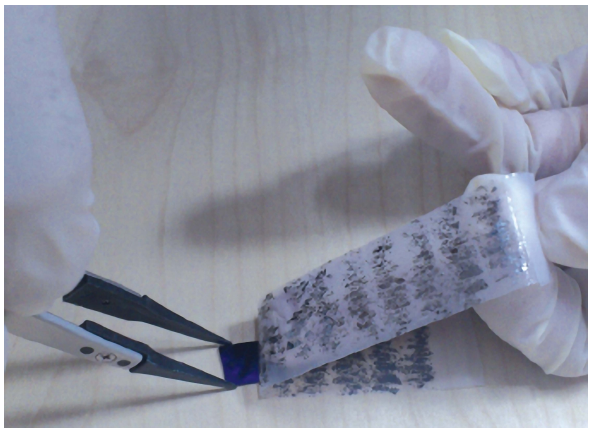

Fig. 1.13 Mechanically exfoliated using scotch tape to create 2D graphene samples.

Substantially all of the manufacturing process of the repeated removal graphitic material consists of a multilayer of a highly ordered pyrolytic graphite (HOPG) crystal with a celluphene tape, and then press the tape on a substrate (such as a Si/SiO_2 wafer) to deposit the graphene samples. The SiO_2 of the substrate has a carefully selected thickness ($\sim$ 300 nm) to improve the optical contrast of a single layer of graphene by an interference effect. With an optical microscope, it is possible to distinguish between mono-layer and the many graphs multilayer graphitic materials behind on the substrate after removal of the band to the left. The size of the samples prepared in this manner in the order of several μm^2 but set a polymer coating on the substrate, the adhesion of the graphene layers which make greater (mm^2) pieces to increase. The graphene samples produced by mechanical cleavage have very good electronic quality and are substantially free of defects [62], but there are some serious problems that are difficult to overcome. It seems impossible to use this method for mass production because there is no control on the number of layers. The monolayers of graphene are produced under a variety of FLG years and must be sought for with an optical microscope, it is difficult to see how this will ever become a high-throughput method for industrial applications. Therefore, other techniques are required for these applications.

1.4.2 Chemical exfoliation

A more recent technique for graphene production is to separate the individual layers in graphite with a solution process [63]. This method uses an intermediate step in which graphite is chemically modified to make it water dispersible. One possibility is Graphite oxide (GO), which can be incorporated with water, in order to separate the layers oxidize, as shown in Figure (1.14 - from ref. [64]). However we want to product pure graphene not GO, so it is necessary again to reduce GO again to graphene. This can be performed by annealing or chemical reduction in solution. The problem with chemical reduction in solution is that the various layers after the reduction unit, as they are not rapidly soluble. This is a problem that seems difficult to overcome. A further possibility is thermal reduction after the solution is applied by spray coating on a heated substrate such as SiO_2.

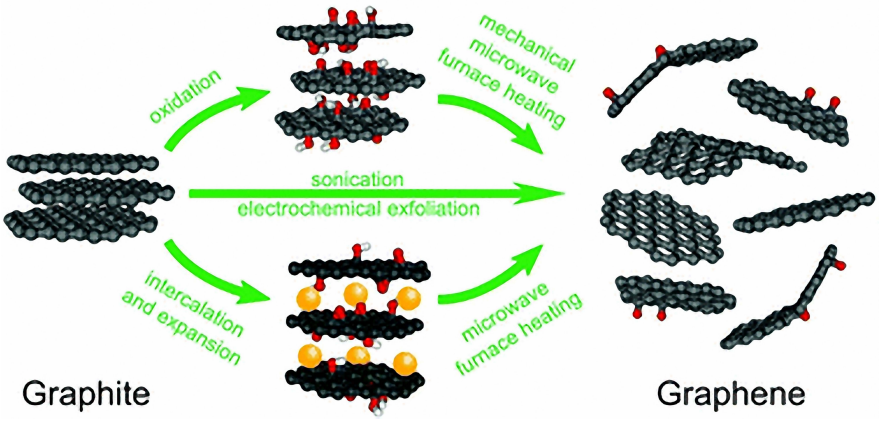

Fig. 1.14 Schematic illustration showing chemical exfoliation of graphene

The main advantage of chemical exfoliation is that it is inexpensive and massive scalability. But the quality of the sample is very low, since a lot of defects in the oxidation/reduction process will be introduced.

1.4.3 Thermal exfoliation

Thermal exfoliations are the preparation methods that lead to the achieving near-complete exfoliation into single-layer materials. Compared to mechanical exfoliation methods, thermal exfoliation has many advantages. First, the thermal exfoliation is usually faster. For example, with high-temperature processes peeling can occur within seconds [65, 66]. Furthermore, most thermal exfoliation methods produce graphs in a gaseous environment, avoiding the use of liquids. For some applications such as electrodes in lithium batteries dry graphene

is required. If graphite is used as the starting material, thermal peeling usually results in the same reduction and exfoliation of graphene. During the heating process, the functional groups attached to the graphite layers decompose and produce gases will accumulate pressure between adjacent layers of graphite. Exfoliation occurs when this pressure exceeds the van der Waals interlayer attractions [66], as shown in Figure (1.15 - from ref. [64]).

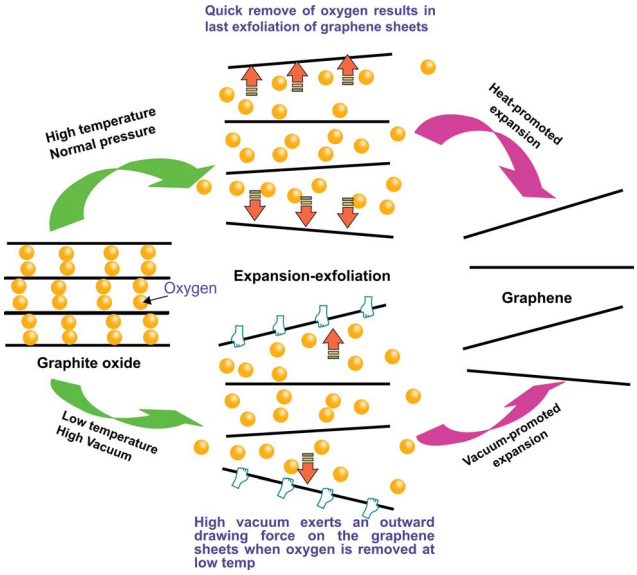

Fig. 1.15 Schematics showing exfoliation of graphite oxide in high temperature under atmospheric pressure (top) and in low-temperature (as low as 200 °C) under high vacuum (bottom).

For the successful construction of the pressure, the starting materials are required to have interlayer functional groups. For this reason, graphite oxide, expanded graphite and intercalated graphite compounds are generally used instead of pure graphite as raw materials for thermal exfoliation.

Successful thermal exfoliation of graphite oxide to produce sheets of graphene monolayer was reported by Schniepp *et al.* [65]. Dried graphite oxide was loaded into a quartz tube and purged with argon. The quartz tube is then rapidly introduced into a furnace preheated to 1050 °C, and less than 30 seconds, the exfoliation of the graphite oxide occurred. McAllister *et al.* [66] later provided a detailed analysis of the mechanism of exfoliation and proposed that the thermal exfoliation had occurred when the rate of decomposition of the functional groups of graphite oxide has exceeded the rate of diffusion evolved gases, thereby creating a pressure sufficiently high to overcome the van der Waals forces between the graphene layers. They also suggested that the critical temperature of 550 C must be exceeded for a rapid exfoliation to occur in seconds. Later, low thermal exfoliation temperature [67], was achieved by heating

the graphite oxide to 250 °C and 300 °C to 400 °C air for 5 minutes.

1.4.4 Photo exfoliation

Photo-exfoliation technique is also capable of achieving exfoliation of graphene sample. The ultrafast structural dynamics of graphite obtained by means of time-resolved electron crystallography reveal the nature of atomic motions under the influence of the quasi-2D lattice potential [68–70]. Following the impulsive laser excitation, the crystal undergoes a contraction followed by a strong expansion along the c axis, indicating the influence of electronic band anisotropy and structural instability by coherent phonon generation. The coherent motion is evident in the diffraction, and it is the collective carrier and phonon dynamics in the first picosecond which determine the extent of layers collisions and ultimately to graphene sheet ablationas, as shown in Figure (1.16 - from ref. [70]).

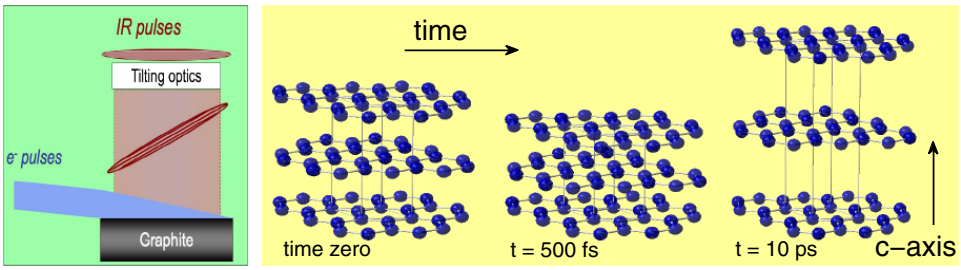

Fig. 1.16 The graphite crystal structure at different times. On the left, a schematic is shown for the optical tilting arrangement used to reach the fs resolution in reflection. On the right, The schematic displays the movements of planes, exaggerated for clarity.

The experimental observations are consistent with theoretical simulations of ablation [71]. Although the collision model is still valid, the time scales used in the theory require further investigations, as shown in Figure (1.17 - from ref. [71]).

The using of femtosecond laser pulses with specific shapes to detach graphene monolayers intact from a graphite surface, one at a time. This athermal process differs fundamentally from conventional laser ablation, which is a thermal process and destroys the desorbed structure. Unlike chemical exfoliation or chemical vapor deposition synthesis techniques, which generally produce defective or chemically contaminated graphene, photoexfoliation appears capable of producing highquality graphene monolayers in large quantities.

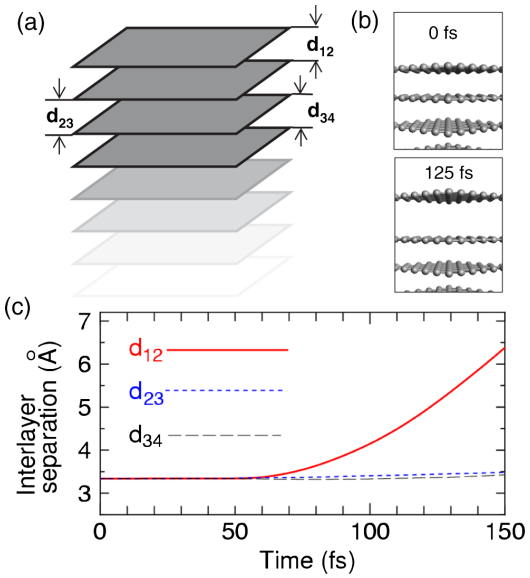

Fig. 1.17 (a) Schematic layer stacking structural, and (b) snapshots of the surface of AB-stacked graphite during exposure to a FWHM = 45 fs laser pulse. (c) Time evolution of the interlayer distances.

1.5 History of graphene

Graphene, has the reputation of being one of the most promising materials in the 21st century. This fact has been emphasized to a great extent by the Royal Swedish Academy of Sciences awarding the Nobel Prize in Physics to Andre Geim and Konstantin Novoselov "for ground breaking experiments regarding the two-dimensional material graphene" in 2010. Although the usage of graphite started 6000 years ago, when Marican in Europe used it to decorate pottery, the research about graphene, dates back to the 1859 to D. C. Brodie in the context of reduced graphite oxide, the fabrication of graphene as experimental and applied devices on a proper substrate was due to Geim and Novoselov in 2004 [62]. Essentially an isolated single-atom plane of graphite, started in the 1960s when surprisingly higher basal-plane conductivity of graphite intercalation compounds were discovered compared to that of the original graphite [72, 73]. The research of graphene grew slowly in the late 20th century, with the hope of observing superior electrical properties of thin layers of graphite or graphene, while obtaining graphene has been considered a daunting task in appearance to both theoretical and experimental. The AB initio calculations in 2002 showed that a graphene sheet was thermodynamically unstable with respect to other fullerene structures if its size was less than about 20 nm [74]. It was generally believed that, based on both theoretical calculation and experimental observation, 2D materials did not exist without a 3D base. It was until 2004 that Andre Geim and

Konstantin Novoselov used a method to isolate graphene, a process similar to what young Kaleb did, drawing with a piece of graphite or peeling graphite with adhesive tape till the graphene is found. Such a "kindergartner" approach can provide high quality graphene with size in hundreds of microns [62]. These high quality graphene crystals realize the investigation of their amazing properties. Since then, the research of graphene including the control of the graphene layers on substrates, functionalizing graphene and exploring the applications of graphene has grown exponentially. As shown in Figure (1.18), the number of publications on graphene (according to ISI Web of Knowledge^{SM}) increases dramatically after 2004.

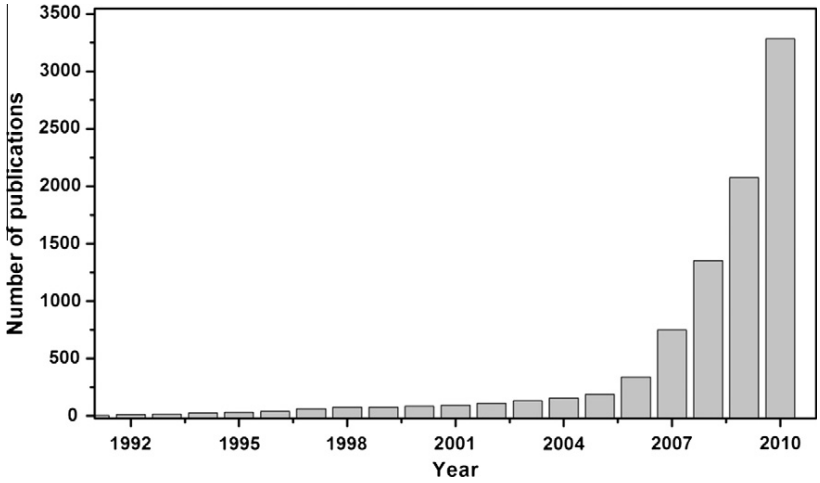

Fig. 1.18 Number of publications on graphene in past 20 years

Despite the short history of graphene, with exceptionally high crystal and electronic quality, it has already revealed a couple of new physical phenomena and potential applications. Therefore, graphene becomes a rapidly rising star on the horizon of materials science and condensed-matter physics [75].

1.6 Graphene

Graphene can be defined as a one atom thick sheet of carbon, tightly packed into a two-dimensional (2D) honeycomb lattice allotrope of carbon [75]. The atomic orbitals of carbon atoms in graphene are sp^2-hybridized, with the three planar sp^2 suborbitals for each carbon atom being used to make three very strong planar σ bonds with other carbon atoms. All the $2p_z$ orbitals are used to form π bonds, which create delocalized electrons, and these are capable of moving freely in the 2D honeycomb lattice of carbon atoms. At low energy the de-

localized electrons behave like 2D relativistic free particles, and is responsible for the electric conductivity. This is the reason behind graphene superior properties [25, 75–78].

The unit cell of this system of two triangular sublattices A and B of graphene is a rhombus, which contains two atoms per unit cell. The nearest neighbors of the A sites are always B sites and vice versa [25], as shown in Figure (1.19 - A).

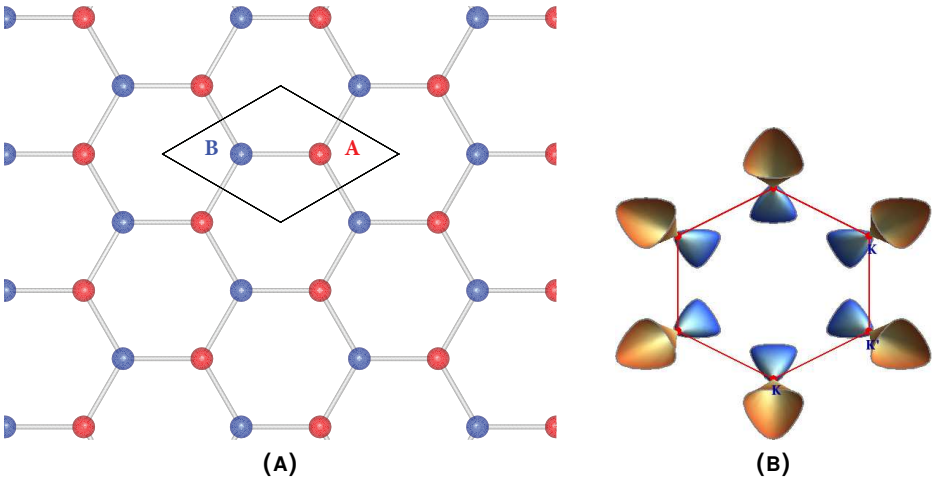

Fig. 1.19 (A) A section of the two dimensional hexagonal graphene lattice structure. The closed region shows the two crystallographically different carbon atoms known as A (red circle) and B (blue circle) sub-lattices, respectively. (B) Shows the Brillouin zone of the graphene lattice with two inequivalent K points around which the energy dispersion becomes linear.

The structure can be seen as a triangular lattice with a basis of two atoms per unit cell, as shown in Figure (1.19). The unit vectors are then given by [25]:

$$a_1 = \frac{a}{2}(3, \sqrt{3}), \qquad a_2 = \frac{a}{2}(3, -\sqrt{3}) \tag{1.1}$$

where a = 1.42 Å is the carbon-carbon distance [25]. The reciprocal lattice vector is defined with respect to the triangular lattice [79],

$$b_1 = \frac{2\pi}{3a}(1, \sqrt{3}), \qquad b_2 = \frac{2\pi}{3a}(1, -\sqrt{3}) \tag{1.2}$$

The first Brillouin zone (BZ) is a hexagon, as shown in Figure (1.20) contains two inequivalent points in reciprocal space which are particularly important for the low energy properties

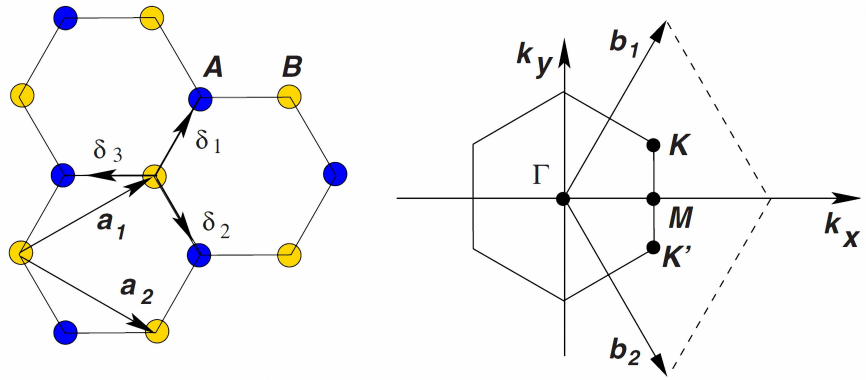

Fig. 1.20 Honeycomb lattice and its Brillouin zone. Left: lattice structure of graphene, made out of two interpenetrating triangular lattices (a_1 and a_2 are the lattice unit vectors, and δ_i, i=1, 2, 3 are the nearest-neighbor vectors). Right: corresponding Brillouin zone. The Dirac cones are located at the K and K′ points.

of graphene. These two points, denoted as K and K′, are named Dirac points, are given by:

$$K = (\frac{2\pi}{3a}, \frac{2\pi}{3\sqrt{3}a}), \qquad K' = (\frac{2\pi}{3a}, -\frac{2\pi}{3\sqrt{3}a}) \tag{1.3}$$

The three nearest-neighbor vectors (δ_1, δ_2, and δ_3) in real space are given by:

$$\delta_1 = \frac{a}{2}(1, \sqrt{3}), \qquad \delta_2 = \frac{a}{2}(1, -\sqrt{3}), \qquad \delta_3 = -a(1, 0) \tag{1.4}$$

The electronic properties of graphene are well described by the electronic structure of a perfect, and infinite graphene crystal in vacuum [62]. The low-energy electronic structure of graphene can be described by a single-orbital p_z nearest-neighbour hopping Hamiltonian [3, 24].

The density of states per unit cell, derived from the Dirac-Weyl equation, is given in Figure (1.21). In this model the point in the energy spectrum that coincides with the Fermi-level of the neutral system is called the Dirac point, but this name is also used for the corresponding point in reciprocal space (usually the K-point) of the hexagonal lattice. The DOS is zero at the Dirac point, but at the same time there is no gap in the band structure so that graphene is actually a zero gap semiconductor.

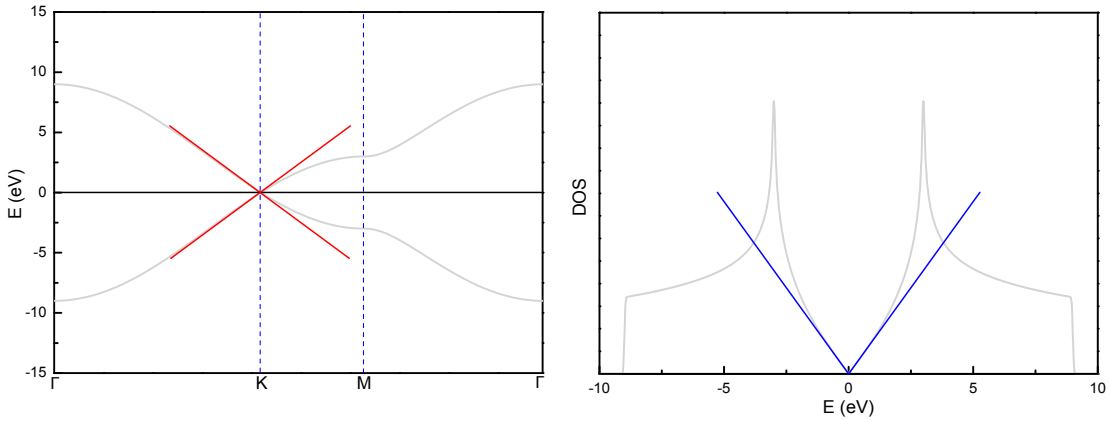

Fig. 1.21 The electronic band structure (left) and the density of states (right) for intrinsic graphene, calculated with Dirac theory (QED) for massless fermions.

1.7 Bilayer graphene

Bilayer graphene consists of two graphene layers lying one on the other, with four carbon atoms in the unit cell, labelled A1, B1 on the upper layer and A2, B2 on the lower layer. According to the usual Bernal AB-stacking the layers are arranged so that one of the atoms from the upper layer A1 is directly below an atom, B2, from the lower layer. We refer to these two atomic sites as 'dimer' sites because the electronic orbitals on them are coupled together by a relatively strong interlayer coupling. The other two atoms, B1 and A2, don't have a counter-part on the other layer that is directly above or below them, and are referred to as 'non-dimer' sites [80–82]. Figure (1.22) shows the crystal structure of bilayer graphene.

Also the bilayer graphene has a zero bandgap and thus behaves like a metal. But a bandgap can be introduced if the mirror-like symmetry of the two layers is disturbed; the material then behaves like a semiconductor [80–83]. Because the unit cell of a bilayer contains four atoms, its band structure acquires two additional bands, π and π^* states, in each valley split by interlayer (A-B) coupling, and two lower energy bands. Due to the strong coupling between A1 and B2, the two corresponding energy bands are split by $\gamma_1 = 0.39$ eV [84].

Figure (1.23 - b) shows the band energies of bilayer graphene for zero asymmetry ($\Delta = 0$). The linear dispersion of single layer graphene is replaced by a parabolic spectrum around **K** point. As a consequence of the parabolic spectrum, the density of states is independent of energy for bilayer graphene. In the limit of large momenta, the linear spectrum is recovered. Further, the energy dispersion is gapless at the **K** point. It is important to realize, however, that the electron and hole band in bilayer graphene effectively just touch each other in this point, whereas they are the natural prolongation of one another in single layer graphene [85].

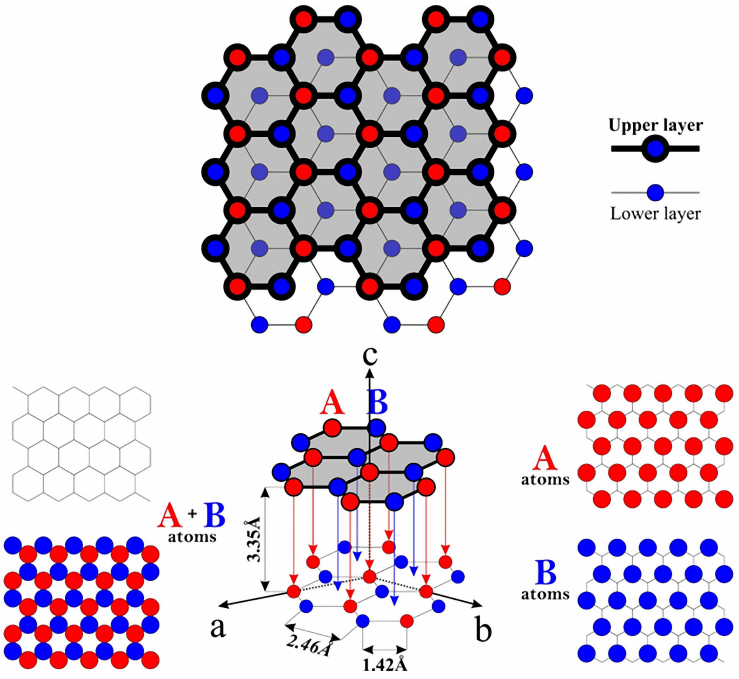

Fig. 1.22 Crystal structure of bilayer graphene.

One of the most remarkable properties of bilayer graphene is the ability to open a gap in the spectrum by electric field [86], and broken the symmetry [87, 88], as shown in Figure (1.23 - c). As a potential difference is introduced to the system, the bands are shifted to higher.

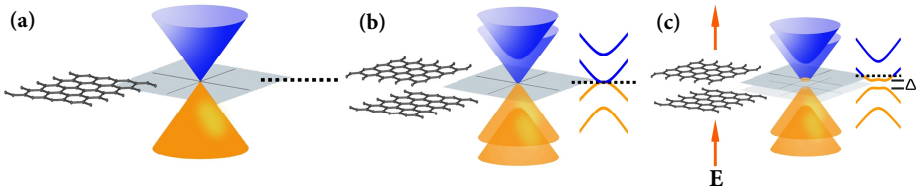

Fig. 1.23 (a) single-layer graphene is that its conical conduction and valence bands meet at a point – it has no bandgap. (b) Symmetrical bilayer graphene also lacks a bandgap. (c) Electrical fields introduce asymmetry into the bilayer structure, yielding a bandgap (Δ) that can be selectively tuned.

Previously, in 2006, researchers at Berkeley Lab's Advanced Light Source (ALS) observed a bandgap in bilayer graphene in which one of the layers was chemically doped by adsorbed metal atoms. But such chemical doping is uncontrolled and not compatible with device applications.

1.8 Hydrogenation of carbon materials

Atomic scale control in carbon nanostructures is essential to manipulate their mechanical, electronic, and magnetic properties. Hydrogenation has been recently attracting a lot of interest as a possible methodology that allows for this control. In contrast to directly manipulating the carbon atoms, e.g., creating vacancies [40, 89–91] or reshaping edges [89, 92], hydrogenation can effectively affect the electronic properties with the advantage that is a reversible process. Hydrogenation of graphene, for instance, was found both theoretically and experimentally to be an effective way to turn graphene from a gapless semiconductor to a gapful one with a tunable band gap [93–96]. It was also shown that partial hydrogenation may induce interesting magnetic properties in graphene which have potential applications in spintronics [97, 98].

The absorption and diffusion energetics of H atoms on graphene are of great importance to determine possible hydrogenation patterns and related electronic properties. Many calculations have been reported on the adsorption and diffusion processes of a H atom on graphene using first-principles electronic structure calculations. The results show that adsorptive carbon atoms on a graphene layer are puckered and, most importantly, that this adsorption leads to magnetic moments on neighboring carbon atoms totalling 1.0 μ_B [99]. Such spin polarization is mainly localized around the adsorptive H atom [91, 98, 100, 101]. The magnetic coupling of H pairs on graphene has also been studied and basically follows the rules expected from Lieb's theorem [102]. Graphene is a single layer of carbon atoms bonded together in a bipartite honeycomb structure. It is thus formed by two interpenetrating triangular sublattices, A and B, such that the nearest neighbors of an atom A belong to the sublattice B and vice versa [3]. Three different magnetic states can be triggered by the H pair, namely, nonmagnetic, ferromagnetic, and antiferromagnetic. The most energetically stable configuration corresponds to having both H atoms adsorbed on the nearest carbon pairs, leading to a nonmagnetic ground state. When the pair of H atoms is on the same sublattice they are coupled ferromagnetically with $S = 1$. When the pair of H atoms is adsorbed on different sublattices, but sufficiently far away from each other, they induce magnetic moments that couple antiferromagnetically ($S = 0$) [91, 98, 100, 101]. For similar distances between the H atoms the ferromagnetic coupling is always favored over the antiferromagnetic one. Previous calculations for vacancy-induced magnetism in graphene show similar results as long as the vacancies do not reconstruct [89, 90].

Many experimental studies, not free from controversy, have reported changes in the magnetic properties produced by irradiation of a graphite sample at room temperature. The re-

sults show that the graphite can have ferromagnetic states in originally non-magnetic graphite samples. These ferromagnetic states survive at low concentration of the impurities induced by irradiation and is independent of the irradiation ion type used [103–105]. Unlike graphene, not many theoretical studies have been reported on the properties of irradiated graphite or hydrogenated graphite. Graphite is a semimetal composed of stacked graphene layers. The Bernal (ABAB) stacking of these planes in a three-dimensional crystal effectively breaks sublattice symmetry: α site atoms that are located exactly above the atoms of the underlying plane, and β site atoms which are located above the center of the hexagonal rings of the underlying plane [106]. Yazyev [107] has studied the magnetic properties of hydrogenated graphite using a combination of mean-field Hubbard model and first-principles calculations. He obtained, as expected, that the sublattices are inequivalent (approx. 0.16 eV) for hydrogenation in bulk graphite and multilayer graphene due to the stacking order of graphene layers.

Due to the frequently found Bernal stacking for graphite, C atoms in one sublattice present C atoms underneath while the ones in the complementary sublattice do not. Thus, at first sight, the referred discovery is not too surprising since the two sublattices present different adsorption energies. However, the specifics of the desorption and diffusion processes of the adsorbed H atoms are essential to determine the final hydrogenation pattern and related electronic properties and, most importantly, the time scale for such pattern. H atoms are initially deposited at high temperatures reaching both sublattices with equal probability. The electronic state thus induced corresponds to that of an antiferromagnet. When the sample temperature is lowered to room temperature, both desorption and diffusion processes can still take place. If desorption rates are larger than diffusion ones, the sample will loose H, changing progressively into a paramagnet until all atoms are lost. If, on the other hand, diffusion rates are larger, H atoms will move across the surface before taking off. In the second scenario they will spend more time on one sublattice than on the other, eventually becoming one more populated. Here, we show that room temperature is, remarkably, just the right temperature to get a 100% sublattice selectivity where all H atoms occupy the same sublattice. Importantly, this occurs on a time scale of seconds which, in addition, is much shorter than typical time scales for H desorption. This spontaneous ordering opens a route for a novel and robust ferromagnetism.

Chapter 2

Basics of theoretical methods and approximations used

2.1 *Ab initio* electronic structure calculations

Ab initio or "first principles" electronic structure calculations are methods based upon fundamental quantum theories, and therefore provide the most accurate and a consistent prediction for the electronic structure (ES) of materials, which in the general sense determines all their physical properties. Here in these methods the atomic numbers of constituent atoms and, usually, some structural information are employed as the only input data. The role of *ab initio* (first-principles) calculations is not just to reproduce, or predict, the structure, but also to understand why that or other crystal structure takes over under certain conditions. In the studies of various materials and their properties, *ab initio* (first-principles) calculations practically imply the use of the density functional theory (DFT) [108–110].
Without going into fine details, I remind in the following some basic issues of the density functional theory (DFT) essential for understanding the organization of calculations done in the present work.

2.1.1 Density function theory

Density-functional theory (DFT) is one of the most popular and successful quantum mechanics methods to investigate the electronic structure of many-body systems in particular atoms, molecules, and the condensed phases. The problem of calculating the properties for a piece of material in many cases can be reduced to the problem of calculating the properties of the electrons in the material. To get accurate results one needs to consider that electrons live in the

world of quantum mechanics. In quantum mechanics we learn that all the possibly information we can have about a given system is contained in the system´s wave function, Ψ. Hence the problem adopt on solving Schrödinger equation for the system. Unfortunately the Schrödinger equation for a system consisting of several atoms solved very complex and requires a great effort. Naturally one tries to solve the equation numerically with help of computers. But, the full many-particle wave function depends on 3N variables (where N is the total number of particles in the system), and this is a very complicated thing. The complexity grows very badly with system size, and therefore solving the full many-particle wave function directly is too hard (even with numerical methods except for very simple model systems with very few electrons). It simply takes too much time and too much memory, thus for relevant materials problems it is impossible. But if we are satisfied with knowing the electronic structure (i.e. we do not care about other special properties of the wave function) then we do not really need the full many-electron wave function. In fact, the electronic structure can be described by a much simpler quantity which is the electron density in space. While the many-electron wave function depends on 3N variables, the electron density depends on three variables only, so it is computationally much simpler to represent and can be accessed for more complex systems. The main idea of the density functional theory is to reformulate the quantum many-electron wave function by the electron density as a base amount for the calculations.

The rudiments of density functional theory were developed by Thomas and Fermi in the 1920s. Calculated energy of an atom, representing its kinetic energy as a function of its electron density, and combining this with the expressions classical nucleus-electron and electron-electron interactions (which can also be represented in terms of electron density). The model was improved by Dirac, which added a exchange energy functional in 1928. However, the theory of Thomas-Fermi-Dirac was inaccurate for most of the applications, by misrepresentation of the kinetic energy as a function of density. The theoretical basis for the DFT was given in 1964 by Hohenberg and Kohn [108], who showed that energy is a functional of the density and the density also minimizes this functional system. However, the most important development was given the following year, when Kohn and Sham showed that from the theory of density functional is possible to write an equation for a particle orbitals, of which the density is obtained. Loosely speaking these theorems state that it is possible to express the energy of an interacting many-body system as a functional of the density, and that all properties of the system are completely determined from only the ground state density. The DFT was very popular for calculations in solid state physics since the 1970s. However, it considered that it was not accurate enough for quantum chemistry until the 1990s, when greatly refined approximations used in the theory. Later, Levy and Lieb came up with a more general formulation

of DFT which amongst other things makes the theory valid also for degenerate ground states. For a detailed discussion of differences between the Hohenberg-Kohn and Levy-Lieb formulations see for example [111]. Now the DFT is a fundamental method for electronic structure calculations in both fields physics and chemistry.

The universal energy functional

To fully describe the quantum mechanical system is sufficient to know the Schrödinger equation for the system. The complete many-particle Schrödinger equation for a non-relativistic system, by using Dirac's bracket notation are written in a compact form as

$$\hat{H}\,|\psi\rangle = \varepsilon\,|\psi\rangle \tag{2.1}$$

where the Hamiltonian operator $\hat{H}$ representing the total energy is defined as

$$\hat{H} = \hat{T} + \hat{V}_{\text{int}} + V_{\text{ext}}(\mathbf{r}) \tag{2.2}$$

The three terms in $\hat{H}$ represent kinetic energy, potential energy due to internal forces, and potential energy due to external forces. The probability interpretation from the wave function leads directly to the electron density n($\mathbf{r}$). From quantum mechanics we know that the density is defined in terms of the wave functions as

$$n(\mathbf{r}) = |\psi(\mathbf{r})|^2 \tag{2.3}$$

As a typical example we illustrate in Figure (2.1) the electron density of the water molecule in two different representations. The total energy for a system in the state ψ can be written

$$E = \langle\psi|\hat{H}|\psi\rangle = \langle\psi|\hat{T}|\psi\rangle + \langle\psi|\hat{V}_{\text{int}}|\psi\rangle + \int d^3r V_{\text{ext}}(\mathbf{r})n(\mathbf{r}) \tag{2.4}$$

The energy of the ground state can, in principle, be found by minimising the expression for the total energy with respect to all possible states $|\psi\rangle$. But suppose that one first minimises the energy only for the set of states $|\psi\rangle$ having the same density n(r). In this case we can write the lowest energy for that density as a functional (i.e. a function of a function, in this case a function of the density)

$$E[n] = \min_{|\psi\rangle\to n(\mathbf{r})}\left[\langle\psi|\hat{T}|\psi\rangle + \langle\psi|\hat{V}_{\text{int}}|\psi\rangle\right] + \int d^3r V_{\text{ext}}(\mathbf{r})n(\mathbf{r}) \equiv F[n] + \int d^3r V_{\text{ext}}(\mathbf{r})n(\mathbf{r}). \tag{2.5}$$

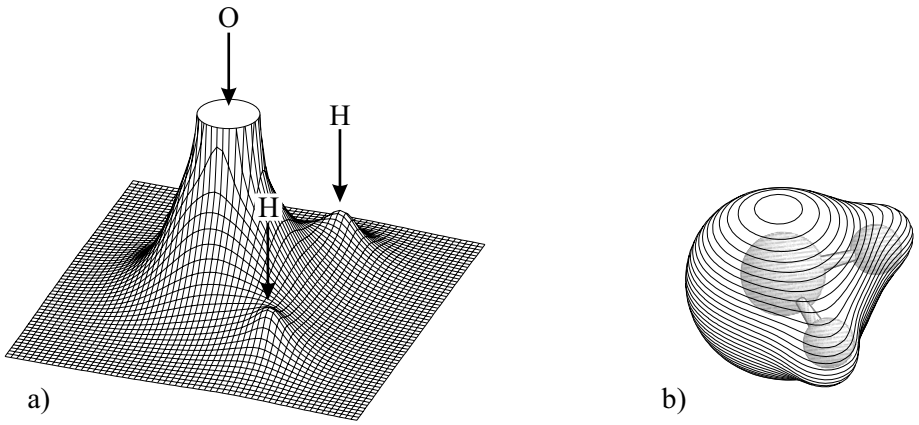

Fig. 2.1 Representations of the electron density of the water molecule: (a) relief map showing values of n(**r**) projected onto the plane, which contains the nuclei (large values near the oxygen atom are cut out); (b) three dimensional molecular shape represented by an envelope of constant electron density (0.001 a.u.).

If we know the external potential V_{ext} and the universal functional $F[n]$, then 2.5 gives us the minimum energy for a specific density $n(\text{r})$. To obtain the ground state energy of the system we must also minimise 2.5 with respect to all possible densities $n(\text{r})$. The functional $F[n]$ is independent of the external potential V_{ext}. The central question is now: what is the universal functional $F[n]$? There is no easy answer to this question, because finding an explicit expression for $F[n]$ corresponds to solving the full many-particle Schrödinger equation. Because of this, density functional theory might have remained a mere curiosity were it not for the approach taken by Kohn and Sham.

The Kohn-Sham approach

In 1965 Kohn and Sham [109] proposed a way to attack the problem of finding an expression for the unknown universal functional F[n]. It is obvious that each electron have kinetic energy, and also energy due to classical Coulomb repulsion between all electrons, but it is not possible to state exact expressions for these quantities because of complicated many-body effects. However, the kinetic energy and Coulomb energy must contribute to the internal energy of the system, and F[n] should incorporate these quantities in some way. It is not easy to see how the quantum mechanical many-body effects (exchange and correlation) affect the energy. Kohn and Sham thought that the complicated many-body effects of the interacting system (contained in F[n]) can be seen as a small correction to the total energy of a similar auxiliary system without difficult many-body effects. Therefore in the Kohn-Sham approach one

replaces the original interacting system with a similar system that can be solved more easily. This simpler auxiliary system is chosen to have the same number of electrons as the original system, and it also has the same external potential. Each single electron has a single-particle kinetic energy (free from manybody effects), and it also feels the Coulomb repulsion from all other electrons. So the Hamiltonian of this auxiliary system must consist of the kinetic energy, the classical Hartree energy and the external potential. Using the DFT formalism we can rewrite the expression for the ground state energy of the auxiliary system as functional of the density

$$E_{aux}[n] = T_s[n] + E_{Hartree}[n] + \int d^3 r V_{\text{ext}}(\mathbf{r}) n(\mathbf{r}) \tag{2.6}$$

The first two terms here can be calculated provided that one knows the one-electron wave functions ϕ_i of the auxiliary system as

$$T_s = -\frac{1}{2}\sum_{i=1} \langle \phi_i | \nabla^2 | \phi_i \rangle$$

$$E_{Hartree}[n] = \frac{1}{2}\int d^3 r d^3 r' \frac{n(\mathbf{r}) n'(\mathbf{r})}{|\mathbf{r}-\mathbf{r}'|}$$

$$n(\mathbf{r}) = \sum_{i=1} |\phi_i|^2$$

Now, in the Kohn-Sham approach to DFT one assumes that the auxiliary system can be chosen to have the same ground state density as the original interacting system. To make this possible one must change the auxiliary system in some way to represent many-body effects that exist in the actual physical system. A new term must express the difference between the original and the auxiliary systems, and it must in the DFT formalism be defined as a functional of the density. Kohn and Sham called this extra term the exchange-correlation functional. All difficult many-body effects are incorporated in this exchange-correlation functional $E_{xc}[n]$. Formally this can be written in terms of an expression for the universal functional F as

$$F[n] = T_s[n] + E_{Hartree}[n] + E_{xc}[n]. \tag{2.7}$$

The beauty of this procedure is that $E_{xc}[n]$ is also universal and can be evaluated - or realistically approximated (for example by many-body theories or from quantum Monte Carlo methods) - once and for all. If we can find an exact expression for the last term $E_{xc}[n]$ then we can actually calculate the exact energy of the original interacting system. The expression for

the total energy becomes

$$E[n] = T_s[n] + E_{Hartree}[n] + \int d^3 r V_{\text{ext}}(\mathbf{r}) n(\mathbf{r}) + E_{xc}[n] \tag{2.8}$$

Here T_s is the kinetic energy of the independent particles, $E_{Hartree}$ is the self interaction energy of the (classical) electronic density and E_{xc} is the exchange-correlation energy. Two problems must be solved before one may actually calculate physical properties of materials and systems. One is to obtain the single-particle wave functions ϕ_i needed to construct the kinetic energy and the density of the auxiliary system. For any given nonzero exchange-correlation the original auxiliary Hamiltonian is no longer valid. Before one can obtain the single-particle wave functions the auxiliary Hamiltonian must be modified to incorporate the effect of the exchange-correlation term. To find this modification one may use the powerful tool of variational calculus. This is discussed further in (subsection 2.1.1). The other is to find an actual approximate expression for E_{xc}. It is not possible to find an exact expression, but there are many good approximate expressions available. This is discussed further in (section 2.1.2).

The Kohn-Sham equation

The tool of variational calculus can be used to find an equation which solutions minimise the energy functional (equation 2.8). If one minimises with respect to the density one gets the so called Kohn-Sham equation. For the actual derivation I refer to standard textbooks, e.g. [111]. The resulting equation turns out to be a Schrödinger-like equation for the auxiliary system where the potential has an extra term due to exchange-correlation effects

$$H_{\text{eff}} |\phi_i\rangle = \left[-\frac{\nabla^2}{2} + H_{\text{Hartree}}(\mathbf{r}) + V_{\text{ext}}(\mathbf{r}) + V_{\text{xc}}(\mathbf{r}) \right] |\phi_i\rangle = \varepsilon_i |\phi_i\rangle \tag{2.9}$$

The solutions to this equation are the so called Kohn-Sham orbitals ϕ_i for the auxiliary system with the approximated many-body corrections present in the form of the exchange-correlation term.

2.1.2 Solving the Kohn-Sham equation

The Kohn-Sham equation is in practise solved numerically by an iterative procedure called the self-consistency loop. The procedure is as follows:

1. Make an initial guess for the electron density n(r).

2. Construct the Kohn-Sham Hamiltonian based on this density.

3. Solve the Kohn-Sham equation to get the Kohn-Sham orbitals.

4. Construct a new density from the Kohn-Sham orbitals.

5. Calculate the total energy of the input and output densities using 2.8. If the difference between these two energies is smaller than some threshold then the final energy is taken as the ground state energy for the system. If the energy difference larger than the threshold go to step 6.

6. Add a little of this new density to the old one to get a new input density and go back to step 2.

Finding the best way to mix the new and old densities in step 6 is not trivial.

Numerical problems with the Kohn-Sham equation

The basic result of density functional theory is that one may rewrite the problem of the many-particle Schrödinger equation in terms of a functional of the electronic density. Kohn and Sham then found a way to practically divide the functional into an exact (but incorrect) part describing an auxiliary system, and a correction part to account for the missing many-body effects. The equation governing the auxiliary system is called the Kohn-Sham equation and it describes independent electrons in an effective potential. The effective potential includes the (approximated) many-body effects of the system. This simplification is a great achievement, but the resulting Kohn-Sham equation is still difficult to solve numerically close to the atomic nuclei. The reason is that in the region of space close to the atomic core the wave functions of the valence electrons oscillate very rapidly. This rapid oscillation happens because the valence states are required to be orthogonal to the core states. To represent these rapid oscillations with sufficient numerical accuracy a very fine grid is required. To use a fine enough grid in the whole space region is not computationally feasible, but since we want to do calculations anyway we need to find a way around this.

2.1.3 The exchange correlation functional

One practical way to interpret this term is as the difference in energy between the simple auxiliary system and the full interacting system. It includes exchange effects of the Pauli-exclusion principle as well as other correlated corrections. It is not feasible to find an exact

expression for the term E_{xc} because it would again correspond to solving the full many-particle problem. But, it is reasonable to assume that this term is small and therefore a good enough approximation could work. This is indeed the case and numerous such approximations have been developed. Much of the theoretical work within DFT has been about finding better and better approximations for the term E_{xc} under the condition that the expressions must be computationally efficient.

The Local Density Approximation (LDA)

The first approximation for the exchange-correlation energy was proposed by Kohn and Sham in the same paper [109] as the so called Kohn-Sham approach described above. In this approximation, called the local density approximation (LDA), one assumes that the exchange-correlation effects are the same as in a system of a homogeneous electron gas. In LDA the effects of exchange and correlation are local in character and the exchange correlation term is

$$E_{xc}^{LDA} = \int d\mathrm{r} n(\mathrm{r}) \varepsilon_{xc}^{LDA}(n(\mathrm{r}))$$

where E_{xc}^{LDA} is the exchange-correlation energy per electron of a homogeneous electron gas at density n. This simple approximation works astonishingly well and gives good results for a lot of atomic systems. Further discussion of the LDA (and the spin-dependent version LSDA) is beyond the scope of this thesis and I refer the interested reader to standard textbooks, for example [111].

The Generalised-Gradient Approximation (GGA)

Following the success of the LDA many generalised-gradient approximations (GGAs) has been developed. Such an approximation is a functional not only of the density, but also of the magnitude of the gradient of the density $\mid \bigtriangledown n \mid$. GGA functionals are chosen to be on the general form

$$E_{xc}^{GGA} = \int d\mathrm{r} \varepsilon_{xc}^{LDA} F(n, |\nabla_n|, ...).$$

F is called the enhancement factor and numerous forms have been proposed. In this thesis a GGA functional called revised PBE (or revPBE for short) [112] has been used for all self-consistent calculations. Further discussion of GGA functionals is beyond the scope of this thesis and I refer the interested reader to standard textbooks, for example [111].

The van der Waals density functional method

In 2004 a new functional called vdW-DF or vdW-DF1 was proposed [113]. It is actually two things. It is a specific new non-local approximation for the exchange-correlation energy E_{xc}. It is also a new framework (today called the vdW-DF method) for extending the reach of DFT by account of dispersive or vdW interactions. The advantage of the vdW-DF method is that it is physics or constraint based and that it treats vdW forces at the same electronic level as DFT treats other types of interactions (e.g. covalent, ionic, metallic and hydrogen bonds) This functional has proven to give promising results for a wide variety of systems, see for example the review article [114]. The total energy functional within the vdW-DF method is defined in terms of the Kohn-Sham scheme outlined in (section 2.1.1):

$$E^{vdW-DF}[n] = T_{\mathrm{S}}[n] + E_{\mathrm{H}}[n] + \int_r V_{\mathrm{ext}}(\mathbf{r})n(\mathbf{r}) + E_{xc}^{vdW-DF} \tag{2.10}$$

This expression includes the standard Kohn-Sham expressions for the the kinetic energy of the auxiliary system T_S, the electrostatic energy of the system E_H and the interaction with an external potential V_{ext} (the atomic cores). What is different in vdW-DF (compared to traditional functionals such as LDA and GGA) is that the correlation part of the energy has a non-local dependence on the density. The full expression for the exchange-correlation energy uses the exchange part of a GGA functional and the correlation part of LDA but adds also a non-local correlation term.

$$E_{xc}^{vdW-DF} = E_c^{LDA} + E_x^{GGA} + E_c^{nl} \tag{2.11}$$

The functional vdW-DF uses the GGA functional revPBE [112] for exchange. One should keep in mind that the standard Kohn-Sham expression for the kinetic and electrostatic energy is also non-local. What is special about vdW-DF is that there is a non-local part also in the expression for the correlation. The expression for the non-local correlation in vdW-DF takes the form of a six-dimensional integral

$$E_c^{nl}[n] = \frac{1}{2}\int_r \int_{r'} n(\mathbf{r})\phi(\mathbf{r},\mathbf{r}')n(\mathbf{r}') \tag{2.12}$$

with an interaction kernel $\phi(\mathbf{r},\mathbf{r}')$. In the asymptotic limit this kernel has the well known $1/r^6$ behaviour characteristic for van der Waals interaction. Now, what is the expression for this kernel function ϕ? The kernel function can be expressed in the following way:

$$\phi(\mathbf{r},\mathbf{r}') = \frac{2me^4}{\pi^2}\int_0^\infty a^2 da \int_0^\infty b^2 dbW(a,b) \times T(v(a),v(b),v'(a),v'(b))$$

where

$$T(w,x,y,z) = \frac{1}{2}\left[\frac{1}{w+x} + \frac{1}{y+z}\right]\left[\frac{1}{(w+y)(x+z)} + \frac{1}{(w+z)(y+x)}\right]$$

and

$$W(a,b) = 2[(3-a^2)b\cos b\sin a + (3-b^2)a\cos a\sin b + (a^2+b^2-3)\sin a\sin b - 3ab\cos a\cos b]/a^3b^3$$

The quantities υ and υ' are defined as

$$\upsilon(y) = y^2/2h(y/d) and \upsilon'(y) = y^2/2h(y/d')$$

where

$$d = |\mathrm{r}-\mathrm{r}'|\, q_0(\mathrm{r}) and d' = |\mathrm{r}-\mathrm{r}'|\, q_0(\mathrm{r}')$$

where the parameter $q_0(\mathrm{r})$ is defined as

$$q_o(\mathrm{r}') = \frac{\varepsilon_{xv}^0(\mathrm{r})}{\varepsilon_x^{LDA}} K_F(\mathrm{r}) \tag{2.13}$$

This quantity $\varepsilon_{xv}^0(\mathrm{r})$ is defined as the LDA expression for exchange and correlation, but with a gradient correction term as

$$\varepsilon_{xv}^0(\mathrm{r}) \approx \varepsilon_{xc}^{LDA} - [\frac{Z_{ab}}{9}(\frac{\nabla n}{2k_F n})^2] \tag{2.14}$$

The LDA exchange used in equation 2.13 is defined as

$$\varepsilon_{xc}^{LDA} = -3e^2 k_F/4\pi$$

where, finally, k_F is defined as

$$k_F^3 = 3\pi^2 n.$$

The parameter Z_{ab} introduced in equation 2.14 determines the contribution of the gradient correction term. This quantity is obtained from first principles and for the functional vdW-DF the value is $Z_{ab} = -0.8491$. In principle, Z_{ab} is not a constant but rather a function of electronic density. For further details about this gradient contribution in vdW-DF see [115] appendix B (and references therein). A derivation of kernel expressions is beyond the scope

of this thesis. For the interested reader a summarised derivation can be seen in [113] and for a detailed derivation I recommend reading the licentiate thesis of Berland [116], chapter 3 and appendix A.

Non-self consistent calculations

It is possible to do what is usually called non self-consistent calculations with DFT. Here one converges the density self-consistently with respect to one functional, and then uses this density to calculate the energy with another functional. This is used for example in situations where one wants to do a full DFT calculation with a certain choice of exchange-correlation functional, but the calculations with this functional are hard to converge in a self-consistent way, or are too time consuming.

2.1.4 Spin density functional theory

The ground state electron density for a physical system might be spin polarised, i.e. $n(\mathrm{r};\sigma=\uparrow) \neq n(\mathrm{r};\sigma=\downarrow)$. This must happen in a system with a finite and odd number of electrons [111], for example the hydrogen - graphene system used in this thesis. It may also happen in an extended system like hydrogen on graphite. For many systems (such as atoms with an even number of electrons) one does not need to keep track of the spin-polarisation and such spin-paired calculations is generally a bit faster. However, it is possible to rigorously generalise the arguments of DFT to include two types of densities, the particle density $n(\mathrm{r}=n(\mathrm{r};\uparrow)+\neq n(\mathrm{r};\downarrow)$ and the spin density $s_\sigma(\mathrm{r}=n(\mathrm{r};\uparrow)-\neq n(\mathrm{r};\downarrow)$. The expression for the total energy is modified to depend not only on the particle density but also on the spin density, see for example [21]. A more detailed discussion of the derivation is beyond the scope of this thesis.

Spin polarised van der Waals calculations

Calculations with the vdW-DF method on systems which are guaranteed to be spin polarised (e.g. hydrogen - graphene) must be seen as a first step in a more systematic theory programme. No derivation of a spin-dependent form for the non-local correlation in the vdW-DF method exist at present [29]. In vdW-DF is implemented in the form $E_{xc} = E_c^{LDA} + E_x^{GGA} + E_c^{nl}$. When one asks for a spin-polarised calculation the spin polarised parts are really Ex and Ec. There are certainly spin-polarised expressions for these first two terms of exchange and correlation. The last term, E_c^{nl}, is the principal term separating vdW-DF from other functionals. One could assume that the plasmon energy which enters in the non-local correlation part is spin-independent. One important question arises: if one did a proper spin-polarised derivation

of the vdW-DF kernel function, would the resulting expression still be invariant under spin-polarisation? The only correct way to answer this question is of course to do the derivation. Unfortunately this is a project far beyond the scope of this thesis. Doing spin-paired calculations is no alternative, because it cannot be done for systems with an odd number of electrons like the hydrogen-graphene system.

In this thesis I have opted instead to illustrate the importance of spin (in treatment of physisorption). In this illustration I have to make an assumption of how the spin would affect the non-local correlation effects.

2.2 Monte Carlo method

Monte Carlo method is a Mathematical method which solves a problem by generating suitable random numbers and observing that fraction of the numbers obeying some property or properties. The method is useful for obtaining numerical solutions to problems which are too complicated to solve analytically. It was named by S. Ulam, who in 1946 became the first mathematician to dignify this approach with a name, in honor of a relative having a propensity to gamble (Hoffman 1998, p. 239). Nicolas Metropolis also made important contributions to the development of such methods.

The kinetic Monte Carlo calculations have been performed to understand the time evolution of the pattern created by the H atoms for different temperatures and concentrations. Kinetic Monte Carlo algorithms are powerful techniques to study the dynamics of a system of particles when the different events that those particles can perform are known as well as their probabilities (for a recent review see [117]). There are many different algorithms with the name of kinetic Monte Carlo [**?**]. In this case we use what is often known as an object kinetic Monte Carlo (OKMC) algorithm, based on the residence time algorithm or Bortz-Kalos-Liebowitz (BKL) algorithm [118] Briefly, in an object kinetic Monte Carlo algorithm a list of possible events is defined with a given probability for each event, Γ_i. The total rate for all events, R, is then calculated as:

$$R = \sum_{i=1}^{n} \Gamma_i N_i, \tag{2.15}$$

where n is the total number of events and N_i is the number of particles that can perform event i. An event is then selected by picking a random number between $[0, R]$. In this way one event is selected every Monte Carlo step from all possible, with the appropriate weight. Once the event has been selected, a random particle is chosen from all those that can undergo that event. The particle is then moved and the total rate has to be computed again for the next simulation

step. At every Monte Carlo step the time increases by:

$$t = \frac{-log\xi}{R}, \tag{2.16}$$

where ξ is a random number between $[0,1]$ that is used to give a Poisson distribution of the time.

The probability of the event usually follows an Arrhenius dependence with temperature:

$$\Gamma_i = \Gamma_i^0 exp\left(\frac{-E_i}{k_B T}\right), \tag{2.17}$$

where k_B is the Boltzmann constant, E_i is the activation energy of the given event and Γ_i^0 is the attempt frequency. In this case the activation energies are related to migration energies, desorption, and dissociation energies.

Chapter 3

Graphene electro-exfoliation with a STM tip

3.1 Introduction

The mechanical exfoliation of graphite has been widely used for decades to prepare clean surfaces suitable for scanning tunneling microscope (STM) studies even at ambient conditions. This has allowed the extensive study of the structure and electronic properties of the last layer of a graphite surface [119]. This process was taken to its ultimate limit when isolated single graphene layers where obtained, showing new and extraordinary properties [44, 62]. Some of these are also present on defective surfaces of graphite when the last graphene layer is slightly decoupled from its graphite substrate [120]. The study of such decoupled layers normally requires a previous chemical or physical treatment of the graphite surface [**?**] or simply finding these on the surface by chance. Here we report the controlled exfoliation process of the last layer of a graphite surface when an electrostatic force is applied with a STM tip. The exfoliated layer is subsequently studied with the aid of the tip. This process and its different ingredients are characterized and can be understood through ab-initio electrostatic calculations and molecular dynamic simulations. Our results demonstrate a new route towards surface modifications fo graphite that can be extended to other layered materials and will permit to gain control in the study of novel electronic and topological properties.

Its low reactivity and almost perfect flatness makes of HOPG graphite surface ideal to be used as substrate for STM studies even at ambient conditions, showing easily atomic resolution. However in such studies it is observed that the tip of the STM can be easily contaminated by the substrate, specially when using high Bias Voltages applied between them. On an other side, previous STM studies have shown the possibility different surface modifications on

graphite using a scanning tunneling microscope [121–123]. Albrecht et al. demonstrated the possibility of creating holes [121] on a graphite surface by simply applying voltage positive voltage pulses to the STM tip. Kondo et al. [122] showed that in the case of negative pulses metallic deposits were formed and explained the hole formation as result of sublimation of carbon atoms induced by the tunneling electrons when this process was done in UHV conditions and to chemical reactions on the surface for ambient conditions. Later, Hiura [123] demonstrated that also the scanning speed affected the results showing a dependence of the threshold voltage to produce a hole and the scanning speed. They attributed this dependence to the kinetics of the oxidation process. In all the cases above, the procedure in which the graphite surface was modified involved either, the mechanical interaction of the STM with the surface,or an induced chemical reaction. It was D. Eigler in his pioneer works [124] who showed that an electrical field can also be used to attract and displace atoms over a surface and this effect have been used by other authors to displace even larger objects [**?**] including graphite flakes [125].

Experimental investigation of this effect and gain control over the modification of layered surfaces as the graphite with a STM trip has been done, by Carlos Untiedt et. al., they using the electrostatic force appearing when there is a voltage difference applied.

For this studies they place the STM tip at the edge of a graphite terrace as the one shown in Fig1a. The mechanism they use is conceptually very simple and consistent in gradually increasing the applied voltage in between the STM tip and a graphite surface thus increasing their electrostatic attractive force. When they do this while keeping a low Tunneling current (about 0.1A in this case) constant to avoid any contact between tip and sample, they can observe that at a certain applied voltage the STM-tip shows a sudden retraction meaning that the graphite surface is being lifted. This lifting process occurs by tearing the graphite surface resulting in a triangular flake being folded on top of the original graphite terrace as shown in Fig 1b.

The whole process can be characterized by recording the movements of the STM tip as depicted in the graph of Fig1c. The green curve starts at about 0.1V which was the applied Voltage used for imaging the graphite surface with them STM. As Voltage is increased, and in order to keep the current constant, a slight retraction of about 0.03 nm/V of the STM-tip is observed. At about 3V the tip has been retracted about 0.1nm, less than one graphite terrace height, and at this point the retraction of the tip accelerates to about 0.06 nm/V meaning that the last graphite layer is being puffed out until the tip is retracted an other 0.25nm at about 6V . This is the point when a sudden abrupt retraction of about 0.5nm, in this case, is observed meaning that the graphite layer has been teared and lifted up. If now the applied voltage is

decreased, we observe almost no further displacement of the tip, meaning that the electrostatic force is still strong enough to keep the graphene layer lifted until about 1V that it is dropped back to the surface. The exact details of this process depend on the tip as a consequence of its exact shape since it will determine the one of the electrical field but keep constant for each tip.

3.2 Graphene layers, and graphite

We begin our study by optimizing the geometric structures of the monolayer, bilayer, five layers graphene, and graphite unit cell in their natural nonmagnetic state. The C-C bond lengths and cell parameters (a and c) and the interlayer distances (d) between the layers are listed in Table (3.1). The accuracy of our procedure is very satisfactory when these magnitudes are contrasted against experimental values. For completeness, we present the atomic structures of single-layer and bilayer graphene in Figure (3.1). Different colors are used to stress different sublattices.

Table 3.1 Atomic structures of single-layer, bilayer, five layers graphene, and graphite.

	c-c (Å)	a (Å)	c (Å)	d (Å)
Graphene	1.419069568	2.457897	25	-
Bilayer	1.419906937	2.459279	25	3.35277104
Five layers	1.419906937	2.459279	35	3.35277104
Graphite	1.417353876	2.454867	6.709482	3.35372034
Experimental		2.456 [126]	6.696 [126]	

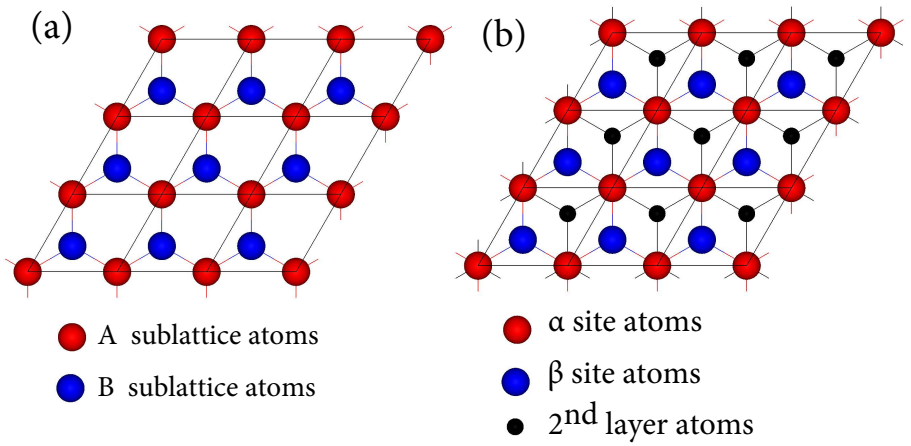

Fig. 3.1 atomic structure of (a) single-layer and (b) bilayer graphene for a $3 \times 3 \times 1$ supercell.

We show in Figure (3.2) the electronic band structure for monolayer, bilayer, five-layer graphene, and graphite along MΓKM. The well-known case of graphene is shown in Figure (3.2-a), being the result similar to that found by many others (see, for instance Ref. [24, 127, 128]). Since there are two basis atoms in graphene there is one pair of $\pi\pi^*$ bands of p_z character, which are degenerate at the K-point or Dirac Point, coinciding with the Fermi level.

We have considered bilayer graphene in Bernal stacking, as for a typical graphite arrangement. Since the basis consists now of four atoms, there are two pairs of $\pi\pi^*$ bands and there are four sets of p_z-derived bands close to the K-point as shown in Figure (3.2-b). Due to the interaction between the graphene layers these bands split apart. Consistent with previous theoretical works [129, 130], we find that, similar to monolayer graphene, the bilayer graphene is also a zero-gap semiconductor with a pair of the $\pi\pi^*$ bands being degenerate at the K-point. On the other hand, there is an energy gap of 0.8 eV between the other pair of $\pi\pi^*$ bands. The band structure for five-layer graphene is shown in Figure (3.2-c) which already anticipates the characteristic band structure of graphite. For instance, at the Γ point five bands, closely packed in energy, manifest the emerging dispersion in the perpendicular direction. Finally, the bands of graphite are shown in Figure (3.2-d). Within about 1 eV around the Fermi level we have four electronic bands, two derived from π orbitals and two from the π^* orbitals of the basis atoms. These results are also in agreement with previous first-principles works (see, e.g., Ref. [131]). Our calculated energy gap between the π and π^* bands is 0.07 eV at the H point and 1.41 eV at the K-point [132].

The number of the pair of $\pi\pi^*$ bands is directly related to the number of basis atoms in the unit cell: e.g. one for graphene, two for bilayer graphene and for bulk graphite, and five for the five layers graphene, as obtain in figure (3.2-c). For a multilayer graphene there is noticeable splitting in the π and π^* bands, except for the innermost pair at the K-point.

The corresponding total density of states for single-layer, Bilayer, and five-layer graphene and graphite are shown in Figures (3.3- a, b, c and d).

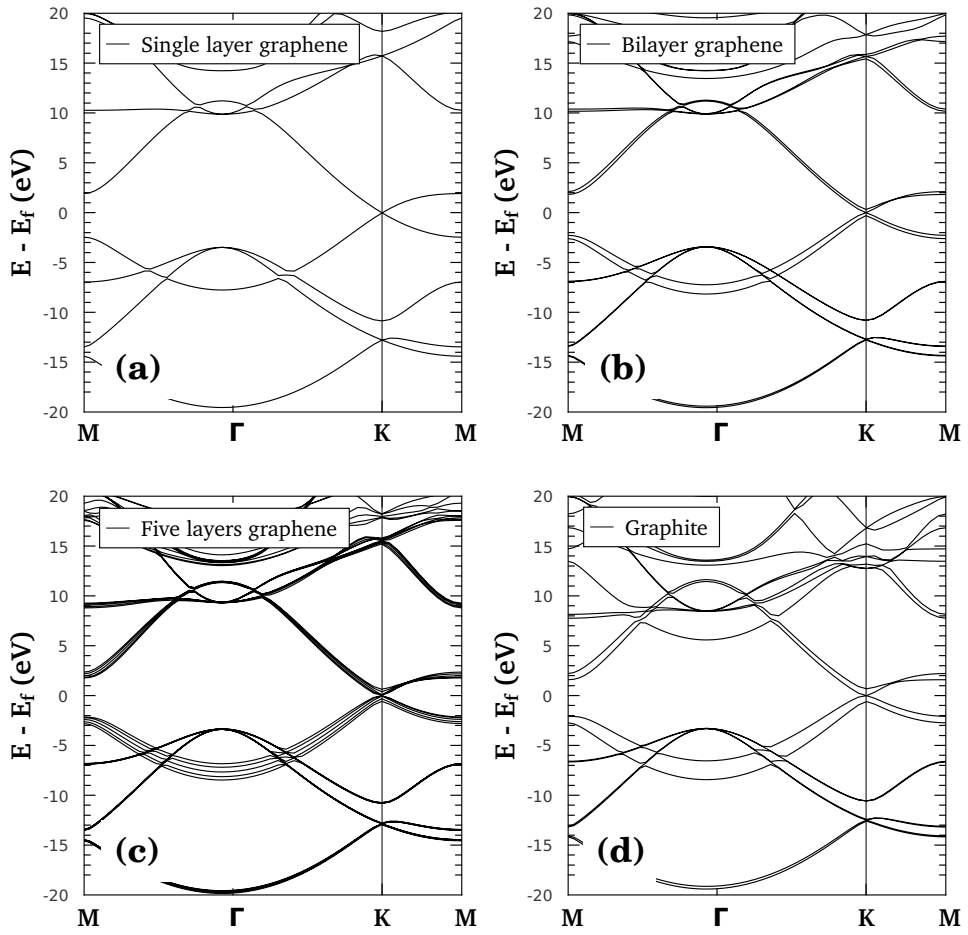

Fig. 3.2 Electronic band structure of single-layer graphene calculated with a $100 \times 100 \times 2$ MP-grid for a $1 \times 1 \times 1$ supercell.

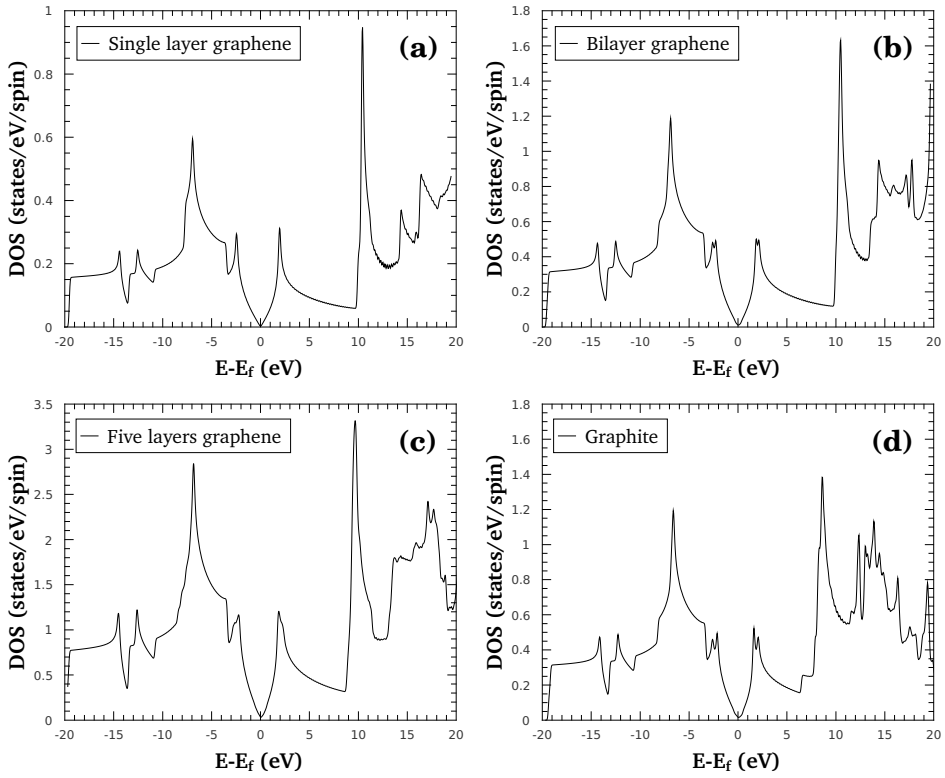

Fig. 3.3 Total density of states calculated with a $100 \times 100 \times 2$ MP-grid for a $1 \times 1 \times 1$ supercell.

3.3 Static charging of graphite layers

Graphite, generally accepted as being ideally flat, is the archetype of layered structures. Static charging on a graphitic sheet break up π bonds by creating electrostatic repulsion forces between graphene sheets induced by charging on a graphitic sheet make graphene well dispersed.

The effect of charging on a graphite slab consisting of 3 layers (3×3 supercell size) of graphene is better seen in Figure (3.4). The distribution of charge in Figures (3.4 - b, and c) shows that positive charge, occurs mainly on both surfaces (i.e. first and third graphene layers), whereas the middle graphene has relatively small positive charge. This is an expected result for a metallic system.

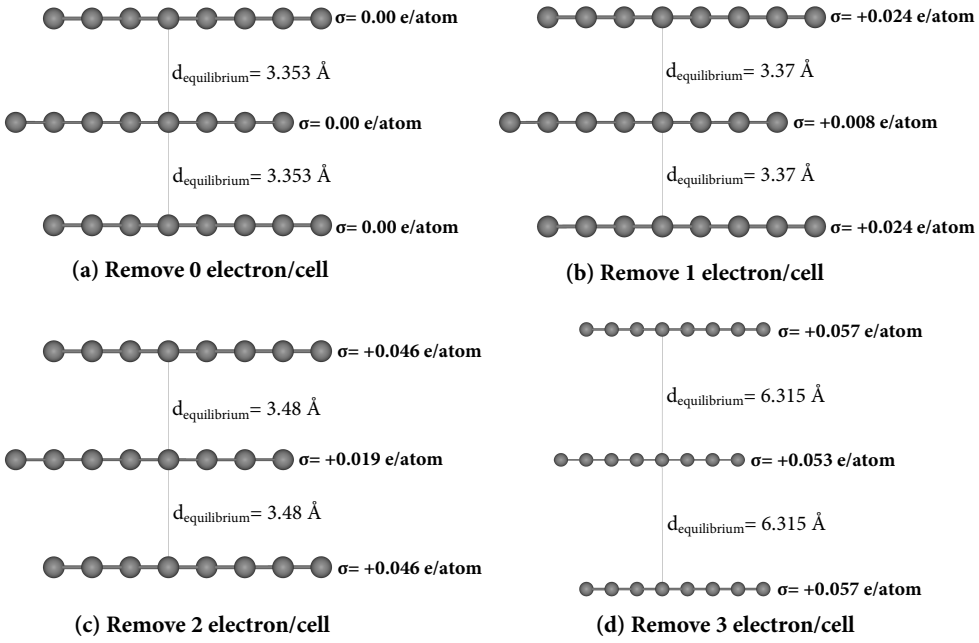

Fig. 3.4 The-charges-on-the-trilayer-graphene-and-distances.

By increasing the charge on the trilayer graphene the separation distance between the graphene layers increases due to increasing the electrostatic repulsion forces between the charged surfaces. In figure (3.4 - d), we show the exfoliated of 3 layers graphene, and distribution of charge occurs on all the graphene surfaces (i.e. three graphene layers).

In figure (3.5) we show the equilibrium distance between layers of a trilayer system as a function of the charge per surface atom. The vdW calculations predict that a threshold charge, Q=0.042 e/atom gives rise to exfoliation of two outermost layers.

Eventually, charged outermost layers of graphite are exfoliated.

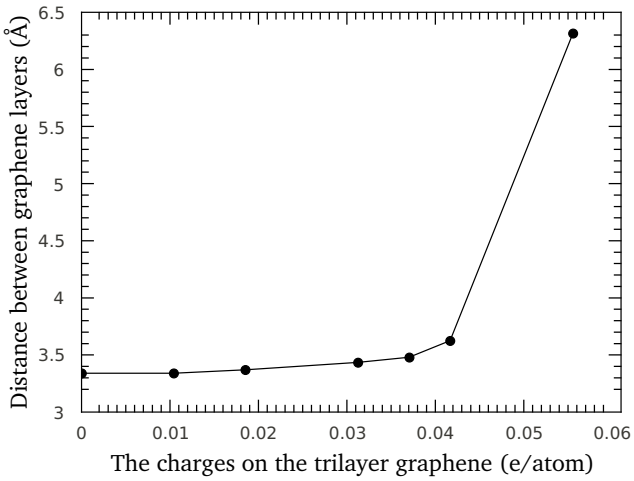

Fig. 3.5 The effect of charges on the trilayer graphene.

3.4 Modeling electrostatic graphite exfoliation

We propose a theoretical model to use electrostatic interaction between a tip and graphite surface as a gentle method to detach an entire graphene monolayer from graphite as shown in figure (3.6-d). In this model, we consider there is a two forces affect on the graphite surface sheet, when we applied the voltage (V) between the tip and the graphite sample. The first, the binding force between the charged graphite surface sheet within the rest of the graphite bulk crystal, and the second, the electrostatic force due to the potential difference between tip and graphite surface sheet. The graphitic sample model consists of five graphene layers with AB stacking, in which each layer is composed of 4×4 supercells thus containing 32 carbon atoms in each layer.

3.4.1 The first force

Due to the fact that in this simple model there is charging induced by the applied voltage (V) on the graphite surface sheet. We can calculate the force between the charged graphite surface sheet within the rest of the graphite crystal obtained from the electrostatic charged system by charging the graphitic sample model as shown in figure (3.6-a).

In figure (3.7), we calculated the charged binding energy curves per atom as a function of the distance between the graphite surface sheet and the rest of the graphite crystal sheets for different charges (Q) on the outer-layers graphite sheets, which contained repulsion energy (from the recently observed detachment of graphene layers in section 3.3, during charging there is a repulsive forces between the graphite surfaces).

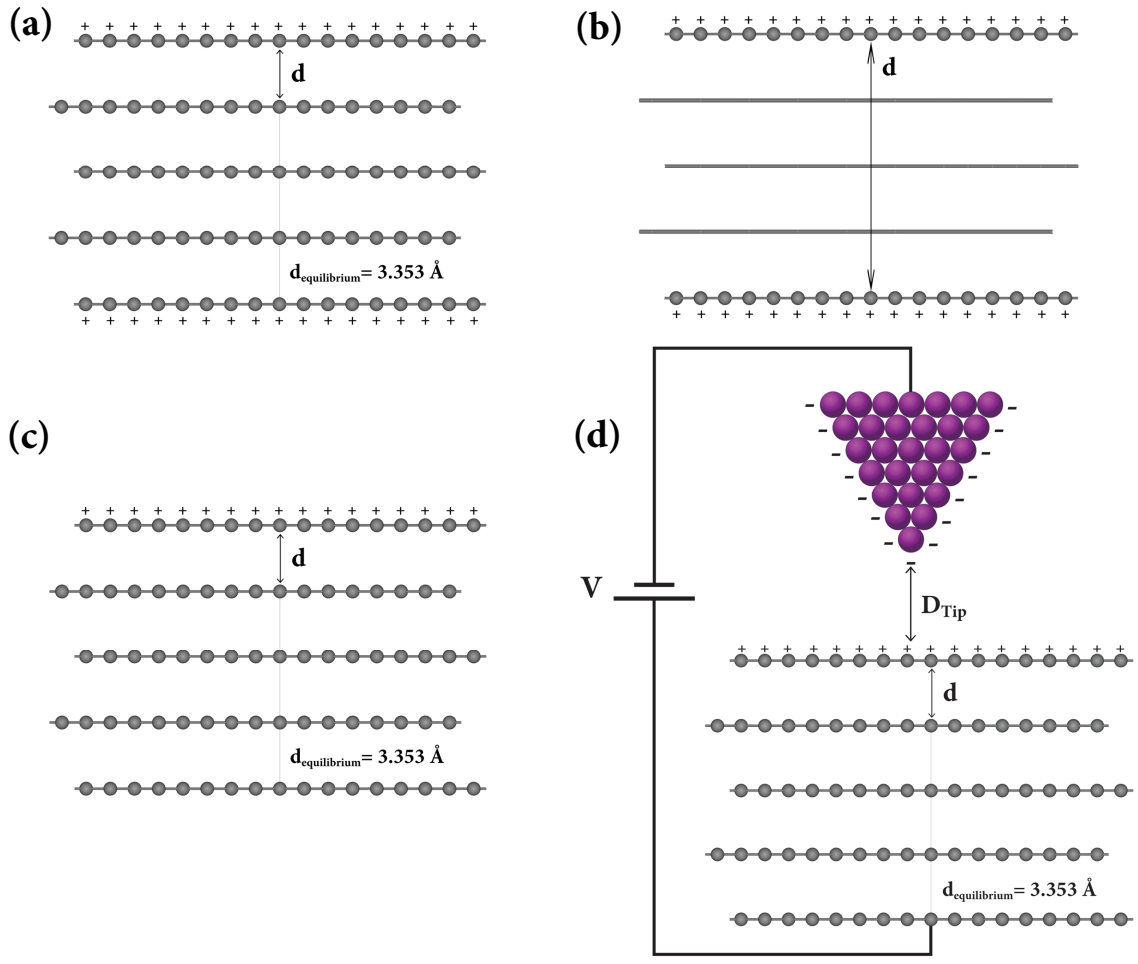

Fig. 3.6 Modeling the electrostatic charging of graphite.

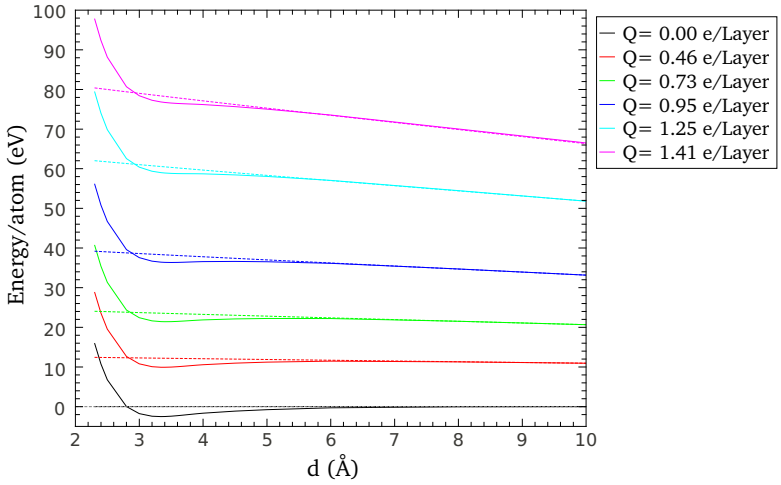

Fig. 3.7 (Solid line) The charged binding energy curves per atom, (Dots line) The electrostatic repulsion energy.

In figure (3.8), we calculated the charged binding energy curves per atom as a function of the distance between the graphite surface sheet within the rest of the graphite bulk crystal for different charges Q with removal the electrostatic repulsion energy forces between the charged outer-layers graphite sheets which depend on the internal distance between the graphite surfaces ($d_{repulsion}$), as shown in figure (3.6-b).

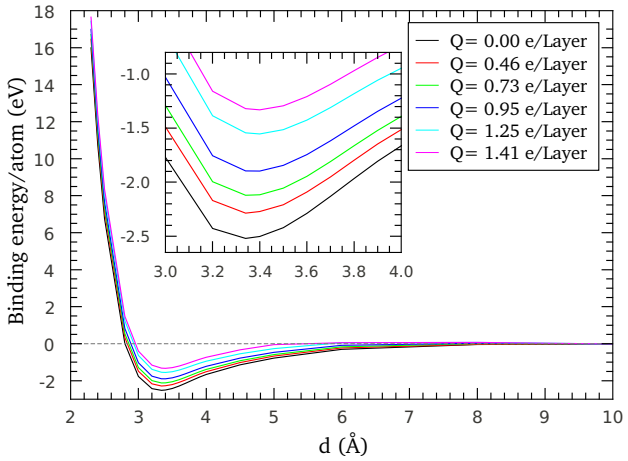

Fig. 3.8 The charged binding energy curves per atom without the electrostatic repulsion energy forces between the charged surface.

From these charged binding energy curves we can obtained the charged binding forces per carbon atom for different charges, F_B, which given from the relation $F_B = -\nabla E_B$, as shown in

figure (3.9).

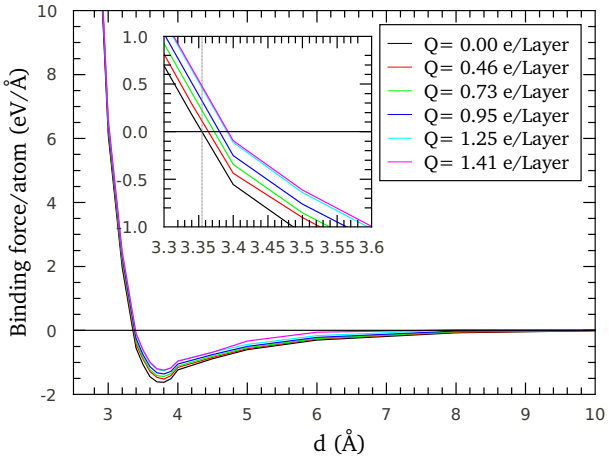

Fig. 3.9 The charged binding force curves per atom without the electrostatic repulsion forces between the charged surface.

At V=0 volt, which corresponding to Q=0 on the graphite surface sheet, the equilibrium distance nicely matches the bulk experimental one at 3.353 Å, this shows at a minimum binding energy -2.53 eV, and at a binding force equal to zero. Increasing the voltage the charges induced on the graphite surface sheet increased concomitant weakening of the binding energy, and increased the equilibrium distance between the charged graphite surface sheet within the rest of the graphite bulk crystal.

In easy way (two charged parallel plate capacitor model), we can calculate the voltage applied (V), to induced these amount of charges (Q) on the graphite surface sheet which depend on the distance between the tip and the graphite surface sheet.

3.4.2 The second force

The second force, the electrostatic force due to the potential difference between the tip and the graphite surface sheet, this force is given by:

$$F_{el} = \frac{-1}{2}\frac{\partial C}{\partial D_{tip}}(V^2 - \frac{\Delta\phi}{e})$$

wherein this force (F_{el}) depend on the geometry of the tip. For this calculation we consider that the work functions difference ($\Delta\phi$) between the tip and the graphite sample is equal to zero. And we consider that there is two types of the geometry a flat tip with an area A, and a spherical tip of radius R. These geometries flat, and spherical tip will be discussed in

subsections 3.4.3 and 3.4.4 respectively. With these models we can calculate the exfoliation voltage (V), which we determine it, when the minimum force curve has a value greater than zero represents a repulsive force with respect to the graphite crystal.

3.4.3 Electrostatic model with using a flat tip

As a first approximation, we consider the tip geometry in the flat form in this system. In this approximation $\frac{\partial C}{\partial D_{tip}} = \frac{\varepsilon_\circ A}{D_{tip}^2}$, where A is the area of the flat tip which we can take it the same as the area of the graphite surface sheet sample (the area of 4×4 graphene supercell size), which have an area equal to (A= 83.84 Å^2), and D_{tip} is the distance between the flat tip and the graphite surface sample. We can rewrite the electrostatic attractive force due to the potential difference between the flat tip and the graphite surface sheet, in the form:

$$F_{el} = \frac{-1}{2}\frac{\varepsilon_\circ A}{D_{tip}^2}(V^2)$$

In this case, we can model the flat tip and the graphite surface as a parallel plate capacitor in which both the energies and the forces scaled linearly with respect to the number of carbon atoms in the graphite surface sheet. We can calculate the electrostatic attractive force F_{el} by using same voltages (V) as which have been applied to induced different charges Q on the graphite surface sheet (to obtained the charged binding force curves F_B).

This allows us to calculate the total force exerted by the two effects, $F_{total} = F_B + F_{el}$. In figure (3.10), we calculated the total force F_{total} effect on the graphite surface sheet as a function of the distance (d) for different applied voltages (V) between the flat tip and the graphite sample. By increasing the applied voltage the total force curves shift the equilibrium position of the graphite surface sheet until the exfoliation voltage (V_{ex}), where the total force greater than zero ($F_{total} > 0$), this represents repulsion force between the graphite surface sheet and the rest of the graphite crystal sheets.

As shown in figure (3.10), the exfoliation voltage (V_{ex}) for a flat tip at distance $D_{tip} = 7$Å is equal to 6.15 volt, while for a flat tip at distance $D_{tip} = 11$Å is equal to 13.6 volt. The exfoliation voltage (V_{ex}) increases linearly with the tip distance (D_{tip}), As shown in figure (3.11).

Subsequently, we can express the relationship between the exfoliation voltage V_{ex} and the distance of the flat tip D_{tip}, In the following equation:

$$V_{ex} = (1.88 \pm 2.69 \times 10^{-3})D_{tip} - (7.06 \pm 3.14 \times 10^{-2})$$

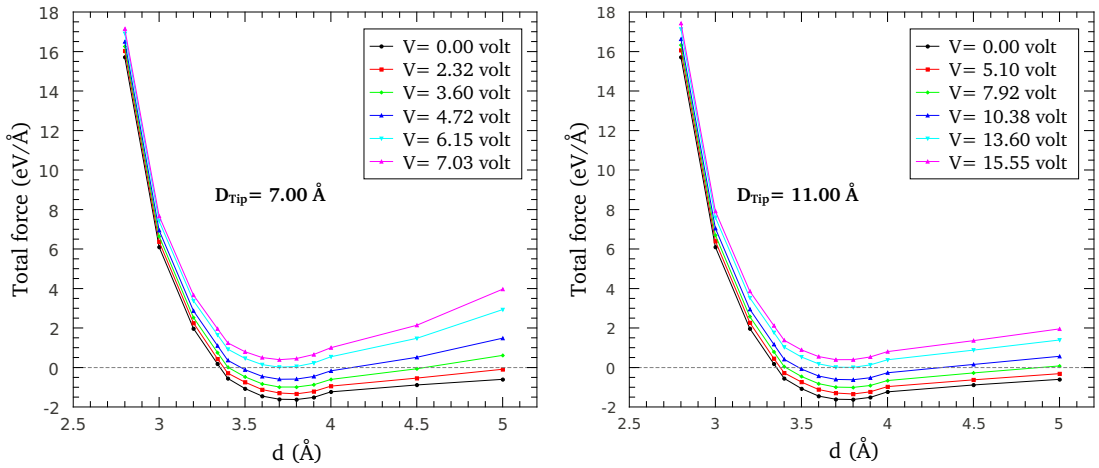

Fig. 3.10 Total force effect on the graphite surface sheet due to a flat tip at distance 7, and11 Å.

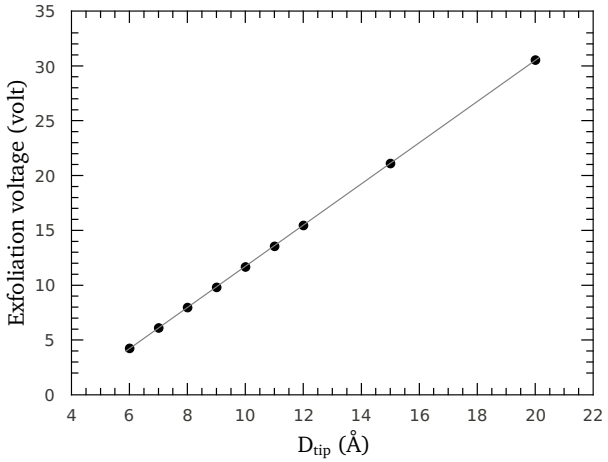

Fig. 3.11 Relationship between the exfoliation voltage V_{ex} and the distance of the flat tip D_{tip}

3.4.4 Electrostatic model with using a spherical tip

Now, if we consider the tip have a spherical geometry form, in this case the term $\frac{\partial C}{\partial D_{tip}} = 2\pi\varepsilon_{\circ}\frac{R^2}{D_{tip}(D_{tip}+R)}$, where R is the radius of the spherical tip which we can take it equal to 5.17 Å which have an area ($A = \pi R^2$ = 83.84 Å^2) same as the area of the graphite surface sheet sample (the area of 4×4 graphene supercell size). We can rewrite the electrostatic attractive force due to the potential difference between the spherical tip and the graphite surface sheet, in the form:

$$F_{el} = -\pi\varepsilon_{\circ}\frac{R^2}{D_{tip}(D_{tip}+R)}(V^2)$$

Due to the spherical shape of the tip over the graphite sample both the energies and the forces no scaled linearly with the number of carbon atoms in the graphite surface sheet. We can calculate the electrostatic attractive force F_{el} by using same voltages (V) as which have been applied to induced different charges Q on the graphite surface sheet (to obtained the charged binding force curves F_B).

This allows us to calculate the total force exerted by the two effects, $F_{total} = F_B + F_{el}$. In figure (3.12), we calculated the total force F_{total} effect on the graphite surface sheet as a function of the distance (d) for different applied voltages (V) between the spherical tip and the graphite sample. By increasing the applied voltage the total force curves shift the equilibrium position of the graphite surface sheet until the exfoliation voltage (V_{ex}), where the total force greater than zero ($F_{total} > 0$), this represents repulsion force between the graphite surface sheet and the rest of the graphite crystal sheets.

As shown in figure (3.10), the exfoliation voltage (V_{ex}) for a spherical tip at distance $D_{tip} =$ 7Å is equal to 6.9 volt, while for a spherical tip at distance $D_{tip} = 11$Å is equal to 12.55 volt. The exfoliation voltage (V_{ex}) increases linearly with the tip distance (D_{tip}), As shown in figure (3.13).

Eventually, we can express the relationship between the exfoliation voltage V_{ex} and the distance of the spherical tip D_{tip}, In the following equation:

$$V_{ex} = (1.38 \pm 7.71 \times 10^{-3})D_{tip} - (2.72 \pm 8.98 \times 10^{-2})$$

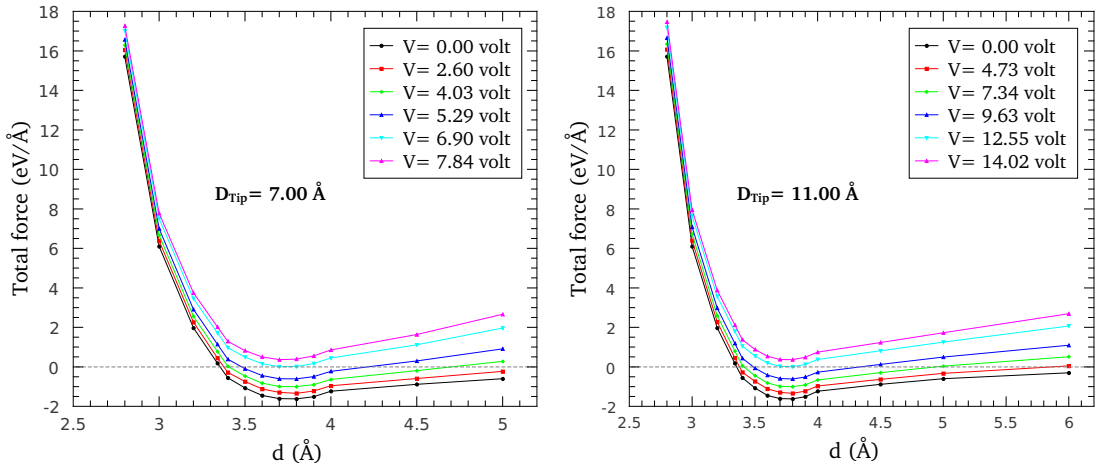

Fig. 3.12 Total force effect on the graphite surface sheet due to a spherical tip at distance 7, and11 Å.

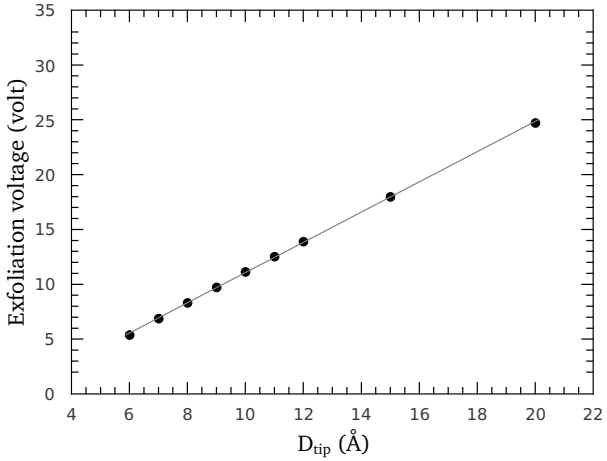

Fig. 3.13 Relationship between the exfoliation voltage V_{ex} and the distance of the spherical tip D_{tip}.

Chapter 4

Hydrogenation-induced ferromagnetism on graphite surfaces

In this chapter, we report a DFT study of hydrogenation on the surface of graphite. First we revisit the energetics of a H pair on graphene and obtain exchange coupling constants as a function of the relative distance and adsorption sublattice. Next we present results for the different adsorption energies on different sublattice for bilayer graphene. Both sets of results are then combined to estimate the relative critical distance that separates ferromagnetic coupling from antiferromagnetic one. Finally, we present a study of the Curie temperature in this system based on a Ising model constructed with the DFT coupling constants. Our results support the existence of ferromagnetic hydrogenated graphite surfaces, as recently reported.

4.1 Introduction

Experimental investigation of the hydrogen deposition has been done using scanning tunneling microscope (STM), by Ivan Brihuega et. al., they deposited atomic hydrogen from a hot hydrogen atom beam source on a pristine graphite surface. Figure (4.1), shows several STM images of graphite surface samples measured at 6K (4.1 - A) before, and (4.1 - B-D) after H deposition. All of them are represented with the same color code for comparison. The previous perfect and pristine graphite surface (4.1 - B), now presents several bright defects of nearly identical height and shape. They performed several preparations with low final coverages between 0.10-0.03 H atoms/nm^2 (or equivalently, 0.0026-0.0001ML; 1ML= 38 atoms/nm^2 = 3.8*10^{15} atoms/cm^2, referred to carbon atoms in graphene layers). After the H deposition the graphite surface presents several nearly identical point defects surrounded by threefold ($\sqrt{3} \times \sqrt{3}$) patterns.

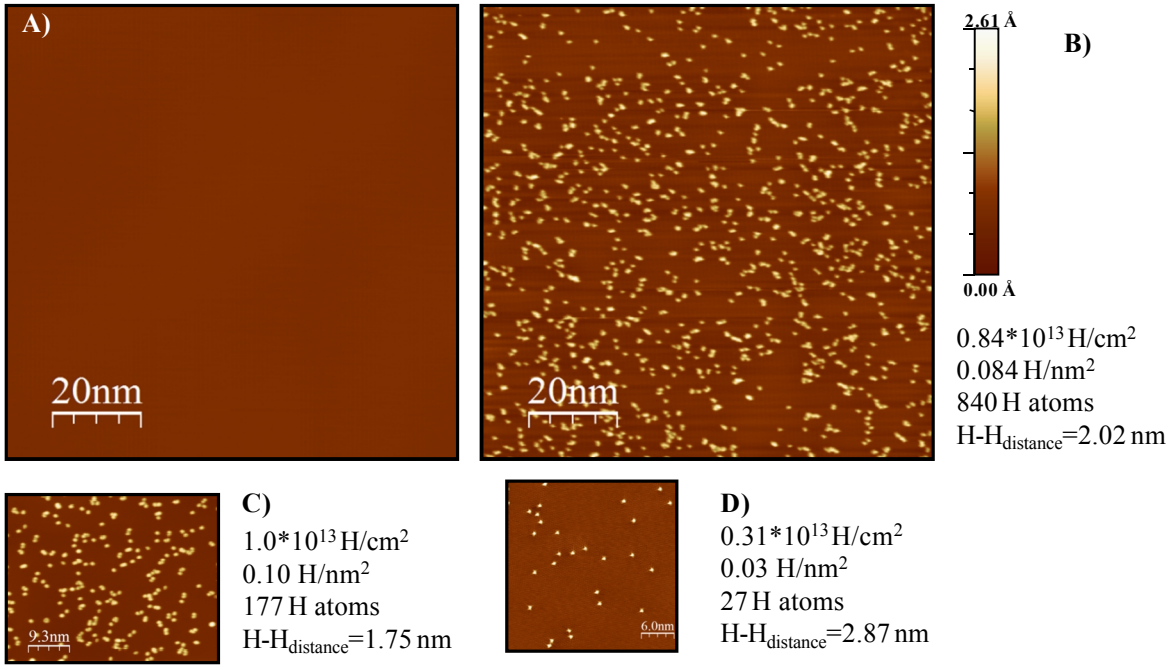

Fig. 4.1 Large scale STM images showing the general morphology of the graphite surface, (A) before, and (B-D) after H deposition for several H coverages.

The resolved STM images of these defects, shows that these defects correspond to a single H atoms placed on the graphite honeycomb lattice sites. In order to identify the H chemisorption sublattice, high resolution STM images resolving both α and β sites in the vicinity of the defects are required, since the actual orientation of the honeycomb graphite surface can only be inferred from them, as shown in Figure (4.2). As outlined in panel B, triangular bright features point in the direction of the six first neighboring atoms belonging to the sublattice opposite to the one where H is chemisorbed. Once such orientation is known, the H chemisorption sublattice is trivially identified from the triangular symmetry of the defects, even when the resolution is not as exceptional.

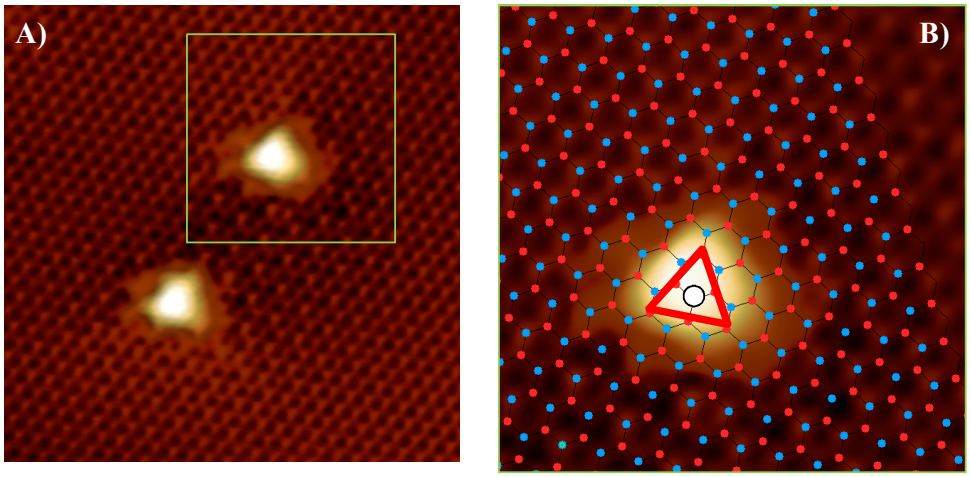

Fig. 4.2 Identification of the atomic H chemisorption site from the triangular symmetry of the defects. Image sizes: A) 7x7nm^2, and B) 3.2x3.2nm^2

4.2 Hydrogen atoms on monolayer graphene

4.2.1 One hydrogen atom

We revisit now, for the sake of completeness, the atomic, electronic, and magnetic structure changes induced on monolayer graphene by the adsorption of a single H atom. In Figure (4.3) we present a view of the atomic structure resulting after the adsorption. This can only occur when the substrate is allowed to relax. In the stable configuration the H atom is covalently bonded to one carbon atom and is located right above this atom, as shown in Figure (4.3)a. The carbon atom in the adsorption site extrudes out of the graphene plane, displaying the typical sp^3 hybridization to form the σ C-H bond [see Fig.4.3(b)] . For all supercell sizes we found that the bond lengths between the adsorbent carbon atom and its nearest neighbors increase up to 1.50Å (which is to be compared to the bond length in graphene of 1.42Å). The other bond lengths are practically unaffected and the C-H distance is always found to be 1.13Å, regardless of the supercell size. Table 4.1 contains a detailed account of our results compared to those found in the literature for this system.

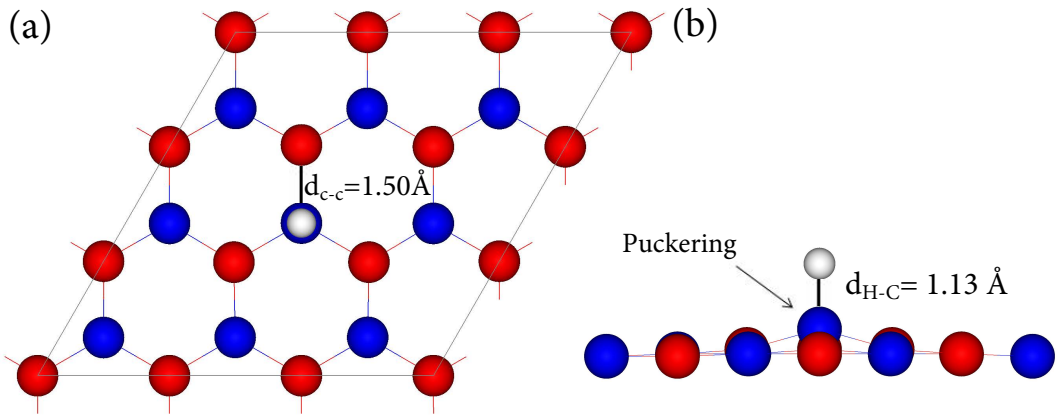

Fig. 4.3 Atomic structure of H on graphene. (a) Top and (b) side view for a $3 \times 3 \times 1$ supercell.

The adsorption energy E_a for a H atom on graphene is calculated as

$$E_a = E_{graphene+H} - (E_{graphene} + E_H) \tag{4.1}$$

where $E_{graphene+H}$ denotes the total energy of the complete system and $E_{graphene}$ and E_H denote the energies of the isolated graphene and H atom, respectively. As shown in Figure

Table 4.1 Equilibrium height of the adsorbent carbon atom above the surface $(d_{puck},)$ and formation energies (E_{form}, eV) for different supercell sizes and corresponding H coverage (Θ). All the carbon atoms are allowed to relax along with the H atom.

Unit cell	Θ	d_{puck} (Å) this work	d_{puck} (Å) other work	E (eV) this work	E (eV) other work
2×2	0.125	0.359	0.36 [133], 0.36 [101], 0.36 [134]	-0.909	-0.67 [133], -0.75 [101], -0.83 [135], -0.85 [134]
3×3	0.056	0.476	0.41 [136], 0.42 [101], 0.51 [134]	-0.915	-0.76 [136], -0.77 [101], -0.84 [134]
4×4	0.031	0.485	0.48 [101], 0.49 [137], 0.58 [134]	-0.946	-0.76 [138], -0.85 [139], -0.79 [101], -0.89 [137], -0.89 [134]
5×5	0.020	0.500	0.59 [101], 0.63 [134]	-0.950	-0.82 [140], -0.84 [101], -0.94 [134]
6×6	0.014	0.531	0.66 [134]	-0.956	-0.96 [134]

(4.4), the binding energy between the H atom and a graphene monolayer increases with increasing supercell size. A linear fit as a function of the inverse supercell size can be done for the calculated points which shows that the adsorption energy is about -0.98 eV in the limit of zero concentration of H atoms. Obviously, for a given supercell size, the binding energy of the H atom sublattice A is equal to the binding energy of the H atom on sublattice B $[E_a(A) = E_a(B)]$.

In agreement with previous studies we also find that the adsorption of H leads to the appearance of a staggered magnetization on neighboring carbon atoms amounting to exactly $1\mu_B$/cell. Such spin density is mainly localized around the adsorptive H atom as shown in Figure (4.5). In Figure (4.6) we show the total DOS for the 6×6 H-graphene equilibrium structure. The H adsorption causes the appearance of peak in the DOS at the Fermi level which spin-splits due to electron-electron interactions. Remarkably, this result is compatible with Lieb's theorem for the Hubbard model on bipartite lattices [102]. According to such

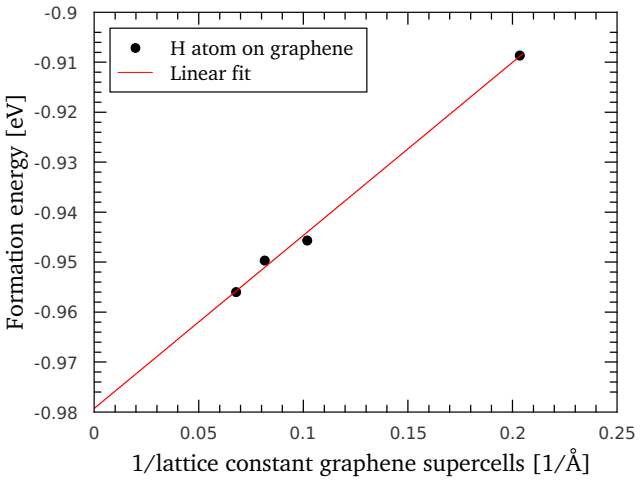

Fig. 4.4 Adsorption energy of a H atom on graphene against different cell sizes.

theorem, the removal of a single site in the bipartite lattice should give rise to a ground state with $S = 1/2$. The covalent bond between the H atom and the C atom underneath effectively suppresses the "site" (the p_z orbital), creating a vacancy in the underlying low-energy Hamiltonian. It is worth noticing how this result contrasts with that obtained for a vacancy. As discussed in Ref. [141], vacancies could in principle give rise to similar magnetic states. The difference with the respect to the case of H adsorption is that vacancies tend to reconstruct and the magnetic moment generated actually vanishes for low concentrations.

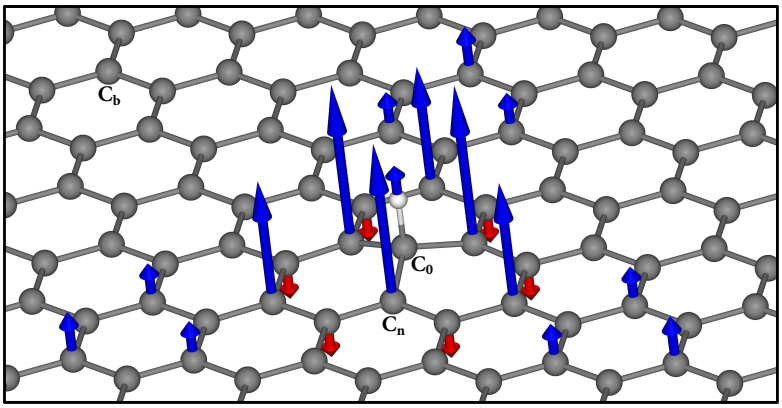

Fig. 4.5 Relaxed atomic structure and spin polarization around an adsorbed H atom over graphene. Magnetic moments with opposite orientations are depicted by blue and red arrows for clarity.

In Figure (4.7) we show the projected densities of states (PDOS) on the relevant atoms.

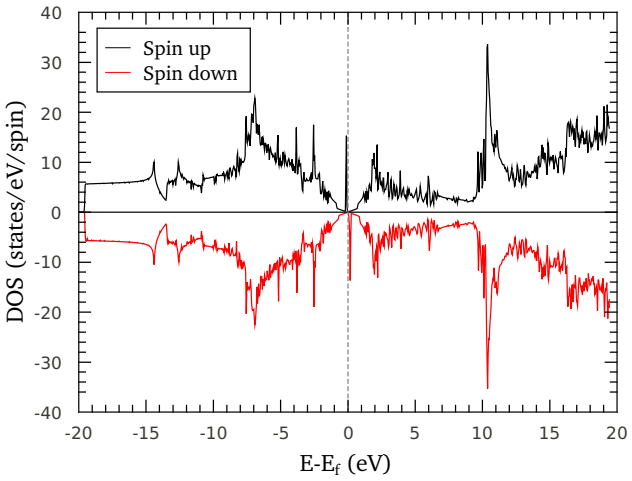

Fig. 4.6 Total density of states for hydrogen atom on single-layer graphene calculated with a $40 \times 40 \times 2$ MP-grid for a $6 \times 6 \times 1$ supercell.

For the H atom a spin splitting close to the Fermi level is visible (4.7-a). There is a negligible spin polarization on the adsorptive C atom (C_0), as shown in Figure (4.7-b). The covalent bond of the adsorptive C atom (C_0) with the H induces a spin polarization in the surrounding C atoms and we find that the magnetic moment is larger at the first-nearest-neighbor C atoms (C_n) as can be appreciated from the strong spin polarization as shown in Figure (4.7-c). The spin polarization induced by the H adatom on the graphene layer tends to quickly decrease at large distances from the absorption point and far from the H atom the PDOS corresponding to the background C atoms (C_b) as seen Figure in (4.7-d)] shows a DOS similar to that of the C atoms in pristine graphene.

4.2.2 Two hydrogen atoms

To investigate the electronic and magnetic structure induced on graphene by two adsorbed H atoms we use a $12 \times 12 \times 1$ supercell. Figure (4.8) shows an example and illustrates the required size of the supercell. The use of such a large supercell is essential in order to minimize the influence of neighboring supercells on the pair-wise properties due to the relative long range interaction between the magnetic clouds induced by the H atoms. The relative extension of the magnetic clouds with respect to the supercell size is illustrated in Figs. 4.9(a) and

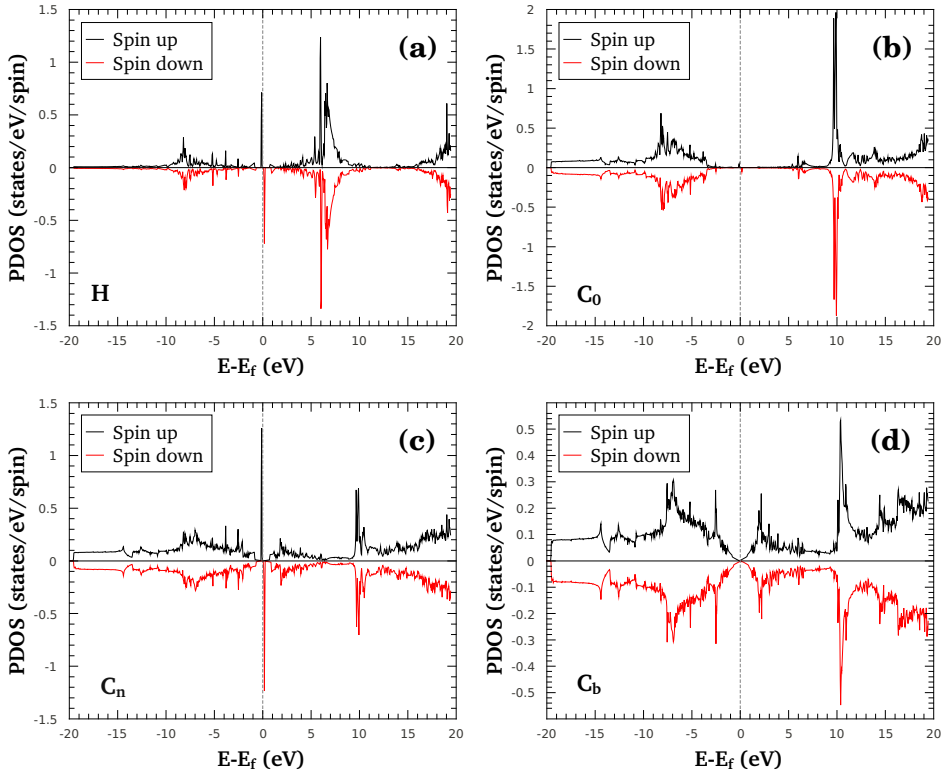

Fig. 4.7 Partial densities of states for (a) the H atom, (b) the pz orbital of the adsorptive carbon atom (C0), (c) one of the first-nearest-neighbor carbon atoms (Cn), and (d) a C atom located far from the atom in the background.

(b). Test calculations show that using larger supercells essentially gives similar results. We calculate the energetics for the two fundamentally different adsorption configurations. One in which the two H atoms are sitting on the same sublattice (AA) and the other where they are sitting on different sublattices (AB). The formation or adsorption energies for pairs of H atoms at various relative adsorption distances for both AA and AB configurations are shown in Figure (4.10). In order to see the influence of the H atoms on the each other, we have subtracted twice the adsorption energy of single H atom.

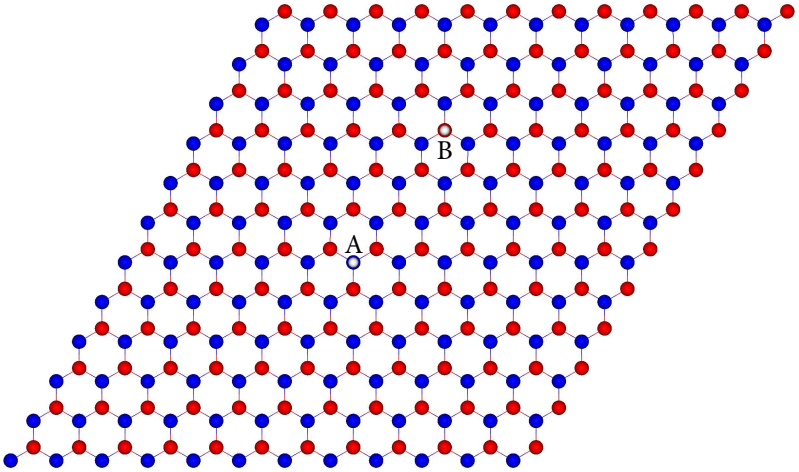

Fig. 4.8 Atomic view of a pair of H atoms on a graphene monolayer for a $12 \times 12 \times 1$ supercell.

First, we can see that the "interaction" energy between atoms is always negative, i.e., the H atoms "attract" each other regardless of the relative adsorption sublattices. (This attraction is obviously counteracted by the diffusion barriers at low temperatures.) It can be appreciated that there is always an energy gain by placing the atoms on different sublattices for any relative distance. This gain quickly grows at short distances (below 1 nm) for the AB case. This can be understood in simple terms by noticing that the H adsorption creates a localized state at the Fermi energy occupied by a single electron. When two states are created on different sublattices, these hybridize creating a bonding state that is now occupied by the two electrons forming a singlet state[89]. This is essentially the reason why magnetic solutions only appear at long distances in the AB cases. As Fig. 4.8 shows, only for the longest possible calculated distance the H atoms retain the magnetic cloud. There the coupling is antiferromagnetic ($S = 0$), as expected from Lieb's theorem. Figures 4.9(b) and (d) show the spin-density and the spin-resolved DOS, respectively, in this case. The latter does not exhibit any spin splitting. On the contrary, when both atoms are on the same sublattice (AA cases) the solution is always ferromagnetic ($S = 1$) regardless of distance [see Figs. 4.9(a) and (c)], but the energy gain with

decreasing distance is very small since the localized states induced by the H atoms belong to the same sublattice and cannot hybridize.

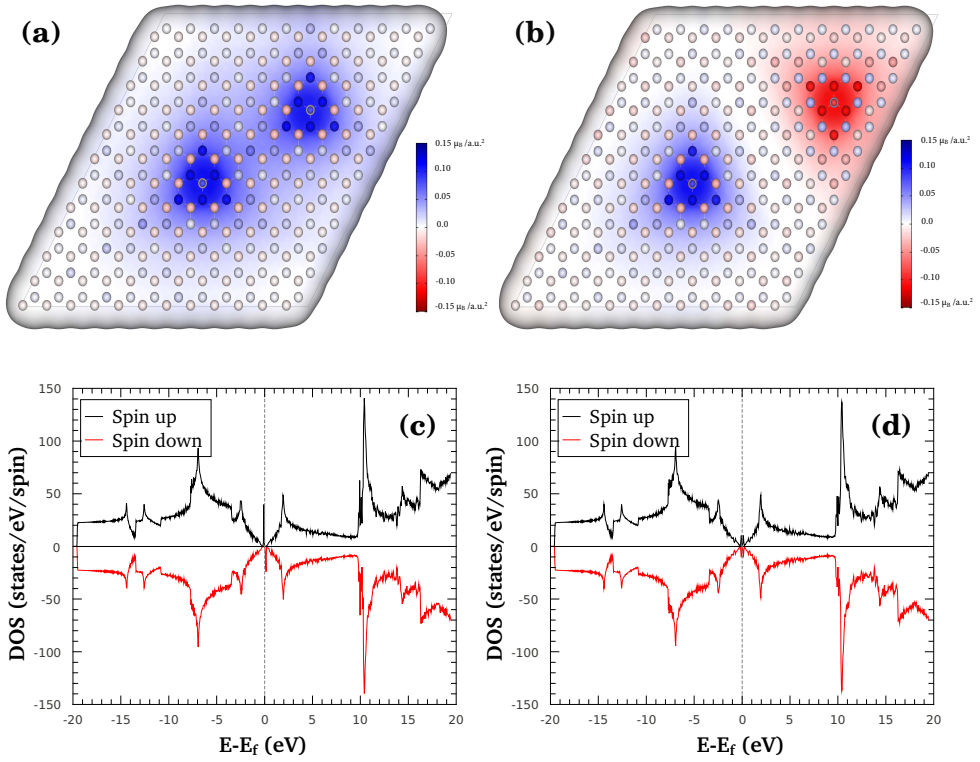

Fig. 4.9 Spin density (blue indicates up and red down) and spin-resolved total DOS for graphene monolayer with 2 H atoms sitting on AA [(a) and (c), respectively] and AB [(b) and (d), respectively] sublattices at far distances calculated with a $4 \times 4 \times 2$ MP-grid for a $12 \times 12 \times 1$ supercell.

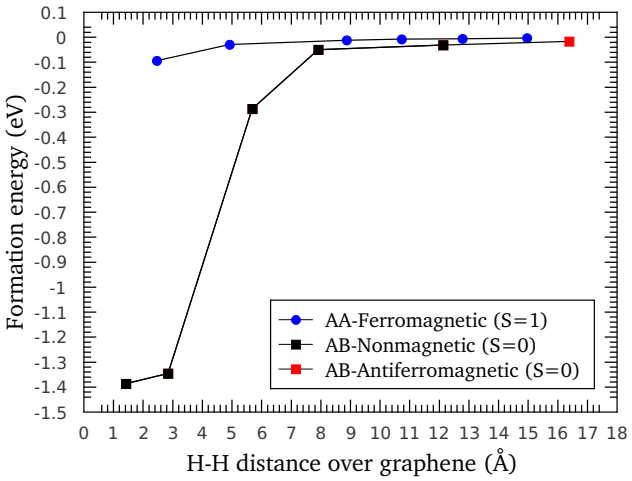

Fig. 4.10 Adsorption energy for a pair of H atoms on a graphene monolayer for a $12 \times 12 \times 1$ supercell relative to the twice a single atom energy. Both AA and AB cases are shown.

4.3 Hydrogen atoms on bilayer graphene

4.3.1 One hydrogen atom

The main focus of this work is actually to elucidate how the interactions of the graphene layers underlying the surface monolayer that hosts the adsorbed H atoms changes the well-established results presented in previous section. As we know, the most stable structure for bilayer graphene, multilayer graphene, and bulk graphite consists of stacked graphene monolayers following what is called Bernal stacking. In Figure (4.11) we present a top view of the obtained atomic structure for the adsorption of a single H atom on a graphene bilayer. Here the upper layer is allowed to relax while the carbon atoms in the lower layer were fixed at their equilibrium position. The adsorption geometry of a H atom on a bilayer graphene surface is very similar to that for graphene monolayer. Due to the interaction between layers, however, in the bilayer graphene case (and surface graphite as shown below) the sublattices are not equivalent $[E_f(\alpha) > E_f(\beta)]$. (In order to make clear that the surface sublattices are not equivalent anymore, we change the labels A and B to α and β from now on.) In Figure (4.12) we show the H adsorption energy difference between α and β sites ($\Delta E = E_f(\alpha) - E_f(\beta)$) for different supercell sizes of the graphene bilayer. ΔE increases linearly with the supercell size, extrapolating to ≈ 85 meV for infinitely large supercells. Importantly, the induced magnetic moment is not affected by the presence of the second graphene layer.

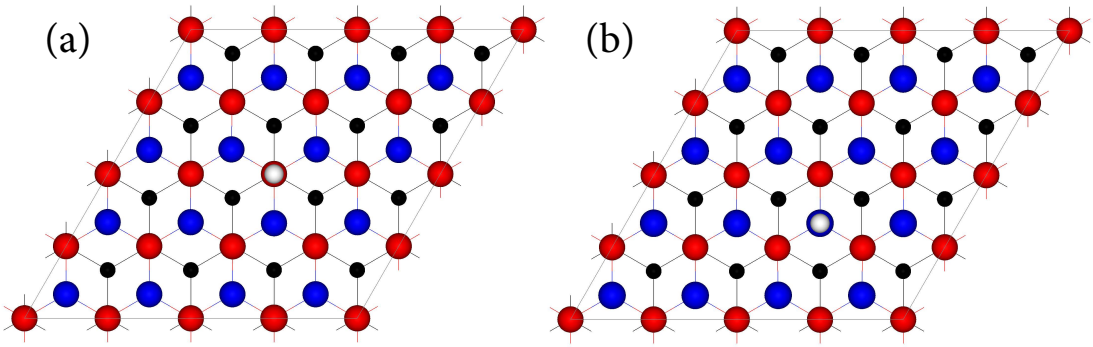

Fig. 4.11 Top view of the atomic structure of H on bilayer graphene (a) α and (b) β sites for a $4 \times 4 \times 1$ supercell.

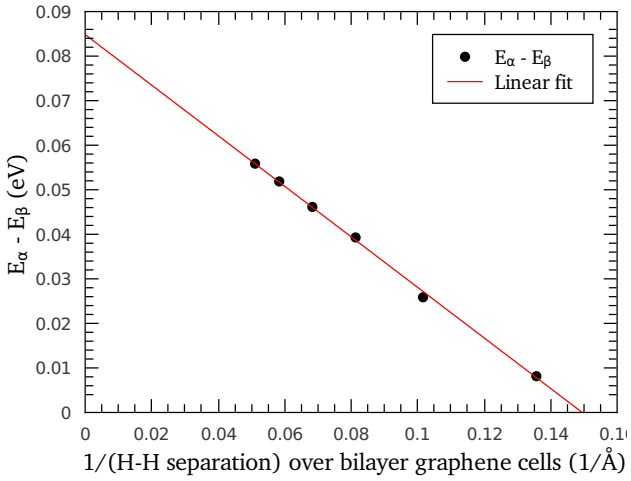

Fig. 4.12 Energy difference for the adsorption of a H atom on the two different sites α and β of a bilayer graphene against different cell sizes.

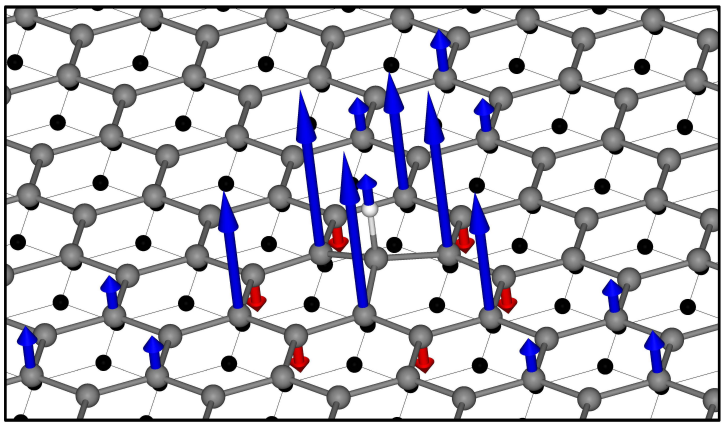

Fig. 4.13 Relaxed atomic structure and spin polarization around an adsorbed H atom over bilayer surface. Magnetic moments with opposite orientations are depicted by blue and red arrows for clarity.

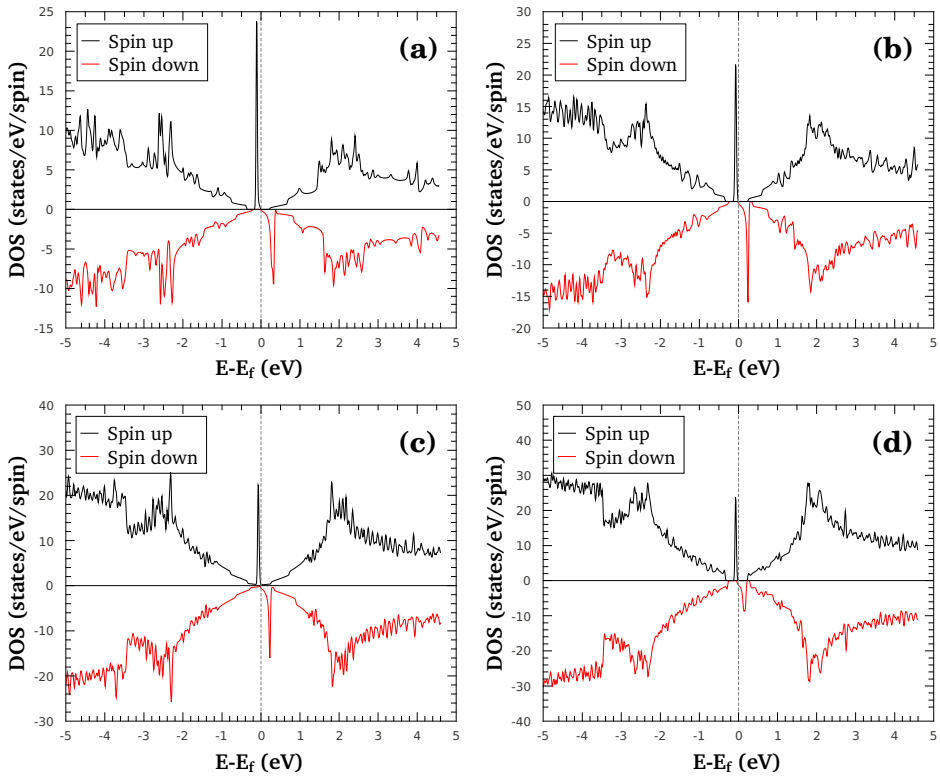

Fig. 4.14 Total density of states calculated for a) 4x4x1 supercell b)5x5x1 supercell c) 6x6x1 supercell d) 7x7x1 supercell.

4.3.2 Two hydrogen atoms

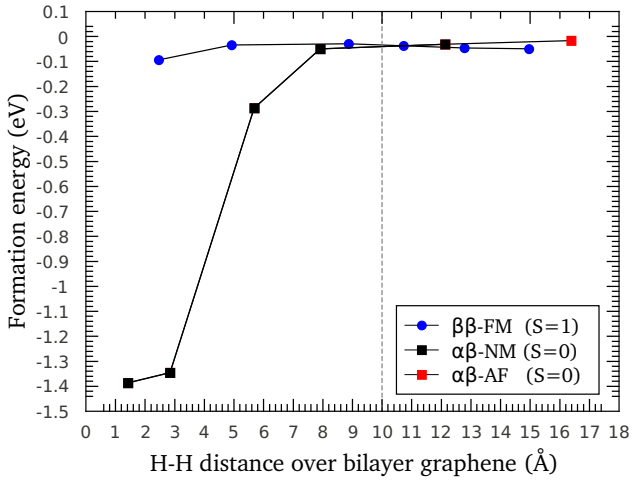

Fig. 4.15 Difference energy $(\Delta E, eV)$ of hydrogen atom on two α and β sites bilayer graphene against different cell sizes.

As shown in previous sections, to properly investigate the interaction between two adsorbed H atoms, one requires very large supercells. A similar study in the bilayer case is computationally prohibited. Here we adopt a different approach. We assume that the attractive forces between H atoms are not affected by the underlying graphene layer. This is not a strong assumption since the interaction between layers is mainly of van der Waals type while the origin of the magnetic structure changes induced on graphene by adsorbed H are of Coulomb type. We now simply correct the pair adsorption energy as a function of distance shown in Fig. 4.10 by the energy difference between different α and β adsorption sites ΔE. There are two possibilities here. One is to use the value of ΔE obtained in the limit of infinitely large supercells. The other is to use a value of ΔE changing with the distance between H atoms. This can be estimated from the calculation for a given supercell size that approximately corresponds to such distance. Either choice obviously favors adsorption on the same sublattice (β in this case) when the H atoms are sufficiently far apart and the intra-layer interactions are weakened. There are not significant differences between both choices. The result for the second choice is shown in Figure (4.15). The pairs of H atoms prefer to sit on the same sublattice for distances longer that ≈ 1 nm, thus inducing a ferromagnetic state on the surface layer.

4.4 Hydrogen atoms on the surface of graphite

We have mentioned in passing that the magnetic moment induced in a single graphene monolayer by the H adsorption survives when a second layer is added to form a bilayer. This is result is not necessarily obvious. Neither is the fact that H adsorbed on a graphite surface may induce a magnetic moment as well. As discussed in Ref. [141], vacancies tend to loose the magnetic moment because the electron-hole symmetry is severely broken and the localized state hosting the unpaired electron is not exactly placed at the Fermi energy. A similar effect could happen here. To make sure we have evaluated the atomic and magnetic structures of a H atom adsorbed on graphite (represented by a four-layer graphene structure). In Figure (4.16) we present the atomic structure determined after the adsorption of a H atom on the surface. Here, also, the upper layer is allowed to relax while the carbon atoms in the lower three-layers were fixed at their equilibrium position. The adsorption of the H atom leads to the formation of a spin density on neighboring carbon atoms, again amounting to exactly 1μB/cell. Such spin density is mainly localized around the adsorptive layer only, as shown in Figure (4.16). Due to the stacking order in the multi-layer graphene structure, the sublattices are, again, inequivalent $[E_f(\alpha) > E_f(\beta)]$ for adsorption. In Table (4.2) we show the difference energy ΔE for a 5×5 supercell size against different numbers of graphene layers. This energy difference converges very quickly with the number of layers so that the results obtained in previous section remain valid here: H atoms adsorbed on a graphite surface locate themselves on the same sublattice in thermodynamic equilibrium and induce a ferromagnetic surface. The Curie temperature of this novel ferromagnet is analyzed in the following section.

Table 4.2 Difference energy $(\Delta E, eV)$ of sitting hydrogen atom on two α and β sites over 5×5 supercell size against different numbers of graphene layers.

No. of layers	$\Delta E = E_\alpha - E_\beta (eV)$
1	0.00000
2	0.03930
3	0.03798
4	0.03866
5	0.03857
6	0.03871

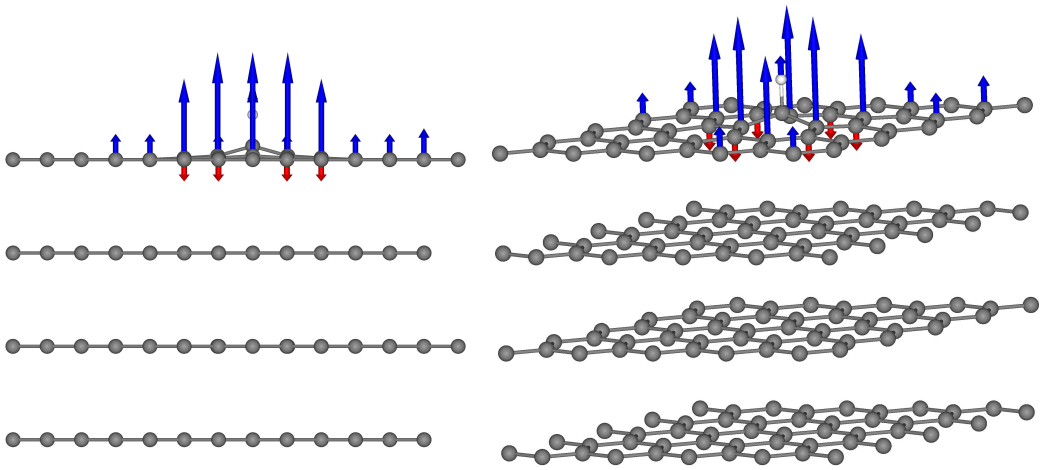

Fig. 4.16 Relaxed atomic structure and spin polarization around an adsorbed H atom at β site over 4-layers graphene surface. Magnetic moments are depicted by blue(red) arrows for spin-up(spin-down) for clarity.

In Figure (4.17), we show the total density of state (DOS) of the 4×4 supercell graphene 5-layers equilibrium structure. It is obtain from the figure that the hydrogen adsorption causes the appearance of a double peak in the DOS, symmetrically placed around the Fermi level.

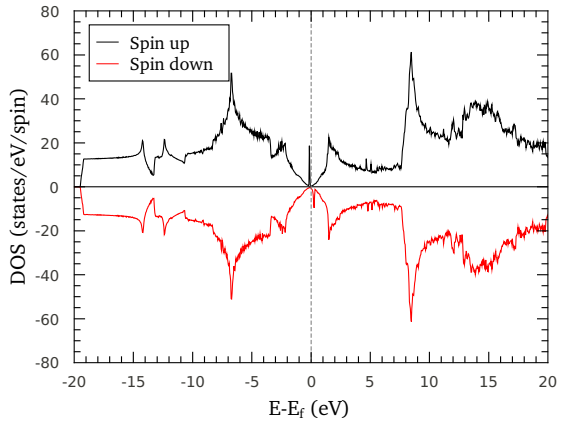

Fig. 4.17 Total density of states for hydrogen atom on five-layers graphene calculated with a $60 \times 60 \times 2$ MP-grid for a $4 \times 4 \times 1$ supercell.

4.5 Curie Temperature Calculation:

Our results show that the adsorption of hydrogen atoms on a graphite surface induce, at low concentrations, a polarized spin density distributed arround the adsorbed H atom. In the diluted regime, the extension of the polarization cloud is small compared to the mean distance between H atoms, therefore to study the collective magnetic properties of the system we will use a model Hamiltonian of the form:

$$H_F = -\sum_{ij,\alpha} J_{ij} p_i S_i p_j S_j \tag{4.2}$$

where S_i and S_j are two spin variables at sites i and j of a given sublattice of the graphite surface. The random variables p_i and p_j represent the occupation of one those carbon with an hydrogen atom. They can take the values 1 (occupied) or 0 (unoccupied). These discrete random variables are drawn from a probability density function:

$$p = (1-C)\delta(p) + C\delta(p-1) \tag{4.3}$$

where C is the concentration of hydrogen and defines a mean distance between hydrogen atoms ℓ. J_{ij} is the magnetic coupling constant between two magnetic moments at sites i and j. The coupling constant is defined as the total energy difference between the antiparallel (AFM) and parallel (FM) alignment of the local moments.

$$J_{ij} = (\Delta E)_{ij} = (E^{AFM})_{ij} - (EFM)_{ij} \tag{4.4}$$

In Figure (4.18), the magnetic coupling J_{ij} have been obtained using ab initio (vdW-DF) calculations methods [108, 109, 142], the exchange energy decreases linearly with the inverse of the H-H pair separation distance. In a very good approximation, it extrapolates to 0 eV in the infinite separation limit.

To study the magnetic ordering in this system we have simulated Hamiltonian (4.2) using the Monte Carlo (**MC**) method over a graphite surface lattice using the Metropolis algorithm [143].

The thermal averaging took 50000 MC measurements, after allowing 1000 steps for thermalization. After that the average over 50 random realizations of the hydrogen distribution was taken. The magnetization curves calculated in cells of the size L= 24.6, 49.2, 73.8, 98.4, and 123 nm is shown in Figure (4.19). Simulations have been performed at the very low concentrations C=0.0005, 0.0006, 0.0007 , 0.0008 , 0.0009 and 0.0010 (considering that 1 means full coverage of the graphite surface with hydrogen atoms).

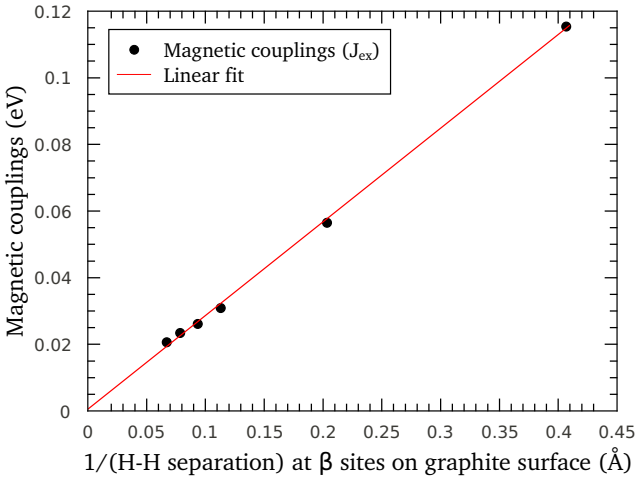

Fig. 4.18 Exchange energy of paire H atoms on β sites over graphite surface.

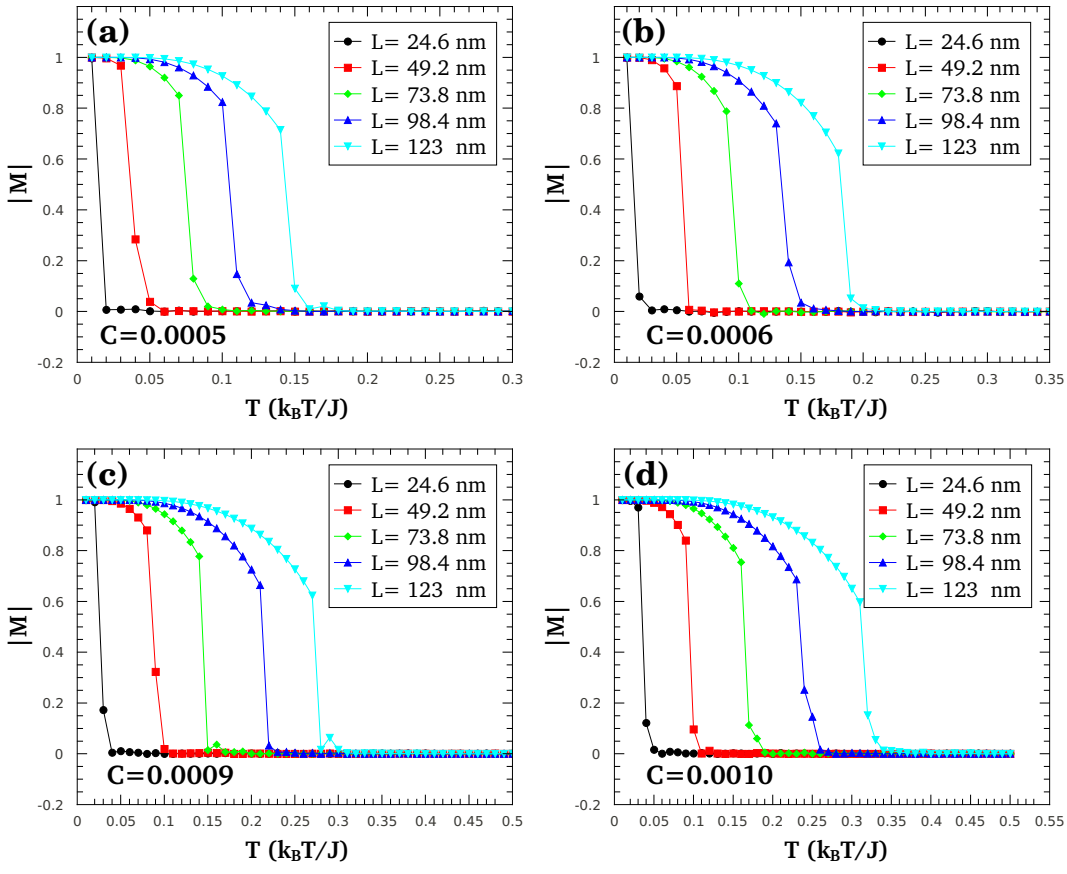

Fig. 4.19 Absolute magnetization per spin for supercells sizes L= 24.6, 49.2, 73.8, 98.4, and 123 nm using concentrations a) C= 0.0005, b) C= 0.0006, c) C= 0.0009, and d) 0.0010

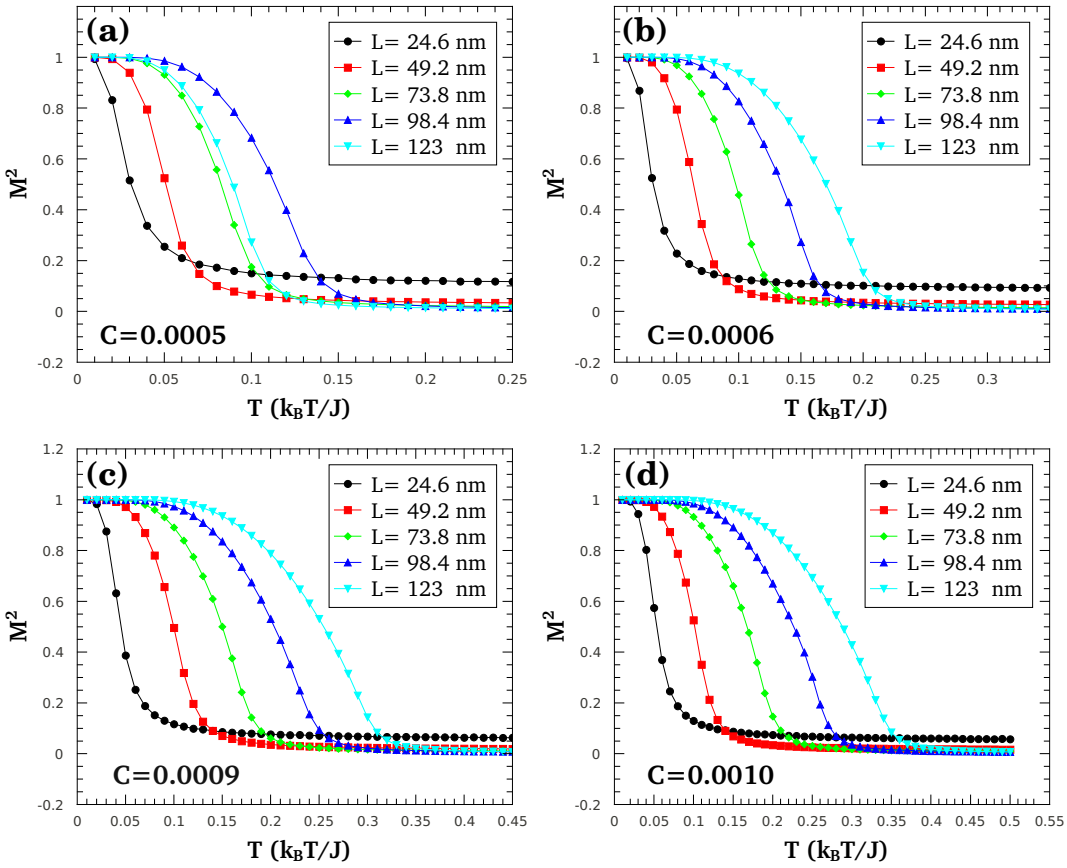

Fig. 4.20 Magnetization square per spin for supercells sizes L= 24.6, 49.2, 73.8, 98.4, and 123 nm using concentrations a) C= 0.0005, b) C= 0.0006, c) C= 0.0009, and d) 0.0010

In Figure (4.19), we show the thermal average of the magnetization absolute value for concentrations(C= 0.0005, C= 0.0006, C= 0.0009, and 0.0010) and a range of sample sizes. The abrupt supression of $|M|$ signals the approximate value of the ordering temperature T_O, however, this ordering temperature increases with the system size. In the thermodynamic limit this behavior extrapolates to a infinite Curie temperature (i.e. a finite magnetization at any finite temperature). Also in Figure (4.20), we calculated the magnetization square value for concentrations(C= 0.0005, C= 0.0006, C= 0.0009, and 0.0010).

We discuss now whether this phenomenon is a finite-size artifact or an intrisec property of the system, consequence of the long-range coupling between the magnetic moments. To study that, we compute the Binder cumulant, used conventionally for an accurate determination of the critical temperature in MC simulations of statistical systems. The Binder cumulant is the fourth order cumulant of the order parameter distribution [144, 145], which is defined as:

$$U_L(T) = \frac{1}{2}\left[3 - \frac{\langle M^4 \rangle}{\langle M^2 \rangle^2}\right] \tag{4.5}$$

where $\langle M^2 \rangle$ and $\langle M^4 \rangle$ are the second and fourth moments of the magnetization distribution, with the brackets $\langle ... \rangle$ and the bar denoting thermal and sample averaging.

The finite-size scaling argument states that, close to a critical point, a thermal average scales as:

$$\langle O \rangle = L^{\mu} g_O(L/\xi) \tag{4.6}$$

where L is the system size μ a critical exponent and ξ is the temperature dependent correlation length, which close to the critical point scales as $\xi(T) \sim (T - T_c)^{-\nu}$. It is well known that several physical properties have important finite size corrections which make difficult the T_c determination. However, if we consider specifically the scaling of the moments of the order parameter:

$$\langle M^{2n} \rangle = L^{2n\beta\nu} g_{M^{2n}}(L/\xi) \tag{4.7}$$

and substitute in the Binder parameter we get $U_L(T) = U(L/\xi(T))$ which is size independent at the critical point. At large temperatures the histogram of the magnetization is expected to be a Gaussian distribution and therefore $U_L(T \to \infty) = 0$. On the other hand, in the zero temperature limit the magnetization distribution function reduces to two delta peaks at opposite values of the saturation magnetization and hence $U_L(T \to 0) = 1$. If a system has a well defined second order phase transition at a finite temperature, the finite-size analysis of the

Binder parameter $U_L(T)$ will show a family of decreasing functions of the temperature, all of them crossing, in a very good approximation, at T_C. In Figure... we show such an analysis for our model. While the qualitative behavior of $U_L(T)$ shows ordering for each independent supercell size, the ordering temperature $T_O(L)$ is clearly size dependent. This behavior is related with the long-ranged nature of the couplings. To illustrate this point, we computed the effective coupling between a single magnetic moment and the rest of the system in the mean field approximation. We rewrite the Hamiltonian in the form

$$H = \sum_i S_i p_i \sum_j J_{ij} p_j S_j \tag{4.8}$$

in the mean-field approximation S_j is substituted by its site-independent mean field value $\langle S \rangle$:

$$H = \sum_i S_i p_i \langle S \rangle \sum_j J_{ij} p_j = \sum_i \bar{J}_i S_i p_i \langle S \rangle \tag{4.9}$$

the expression above defines a local mean-field coupling J_i as :

$$\bar{J}_i = \sum_j J_{ij} p_j \tag{4.10}$$

and averaging over all lattice sites we define a total effective coupling

$$\bar{J}_i = \frac{1}{L} \sum_{i \neq j} J_{ij} p_j p_j \tag{4.11}$$

In the limit of large supercell size $L/\ell \ll 1$ $\bar{J}_i$ takes depends on the size and concentration as $\bar{J} = 0.358CL$. Rescaling all our data, we obtained the same stender Binder cumulant curves with the cross point curves, as shown in figure (**??**).

Now, we can obtained the relation between the Curie temperature T_c for each supercell sizes with the concentrations, as shown in figure (4.23).

The Curie temperature (T_c) of hydrogen atoms on graphite surface were calculated from Figure (4.23) as:

$$T_c = (0.352)CL \tag{4.12}$$

where the subscript C denotes the spin concentration on graphite surface, and L denote the supercell graphite size.

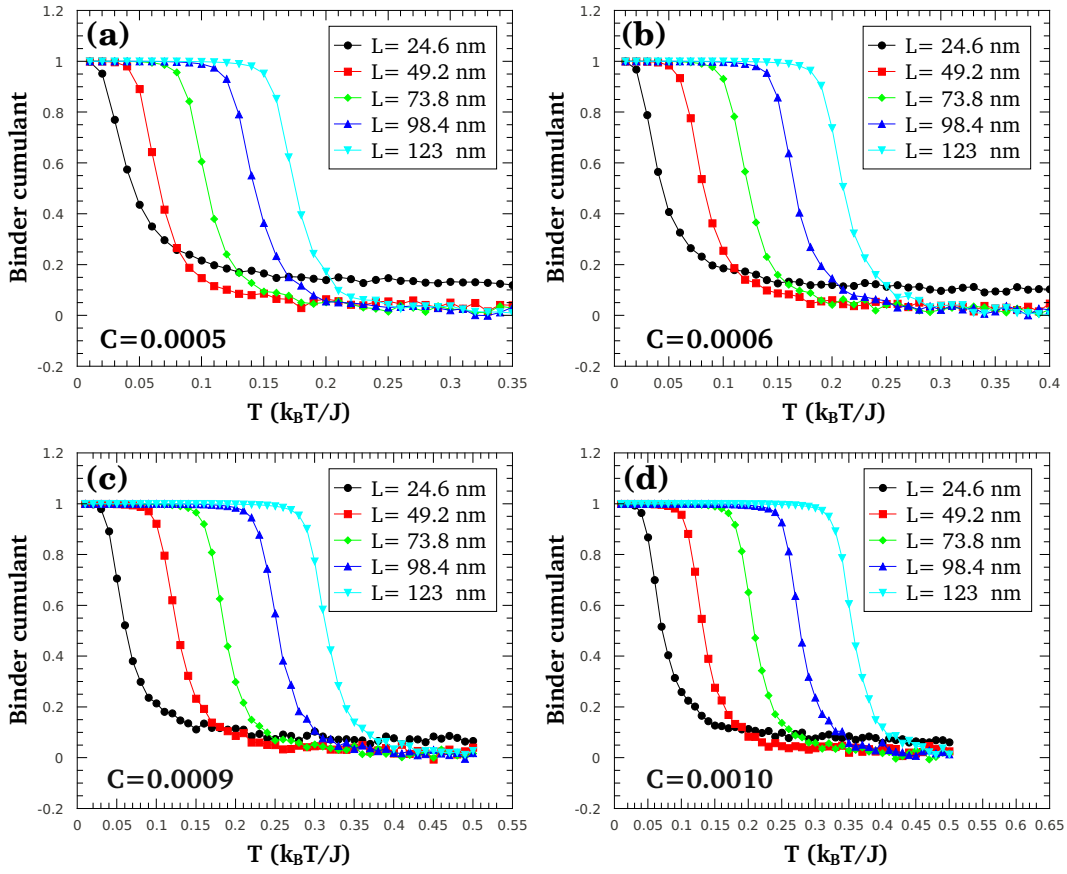

Fig. 4.21 Fourth-order cumulant for supercells sizes L= 24.6, 49.2, 73.8, 98.4, and 123 nm using concentrations a) C= 0.0005, b) C= 0.0006, c) C= 0.0009, and d) 0.0010

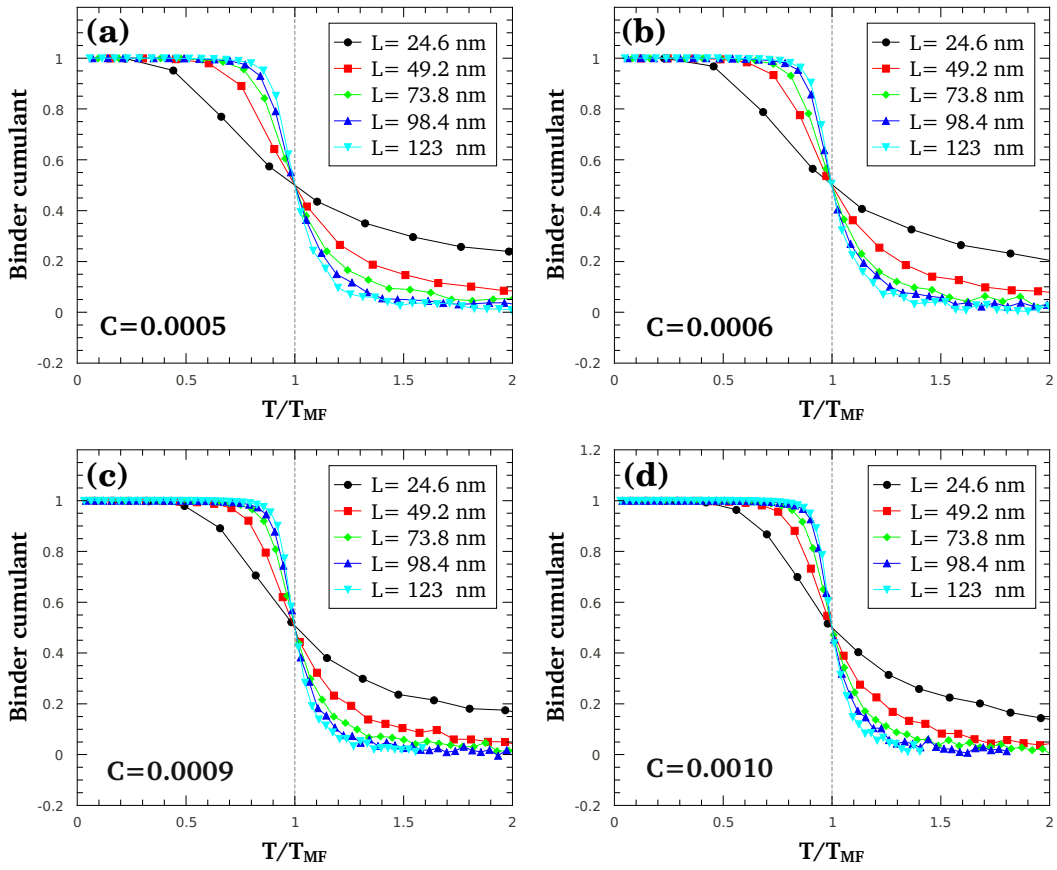

Fig. 4.22 Fourth-order cumulant for supercells sizes L= 24.6, 49.2, 73.8, 98.4, and 123 nm using concentrations a) C= 0.0005, b) C= 0.0006, c) C= 0.0009, and d) 0.0010

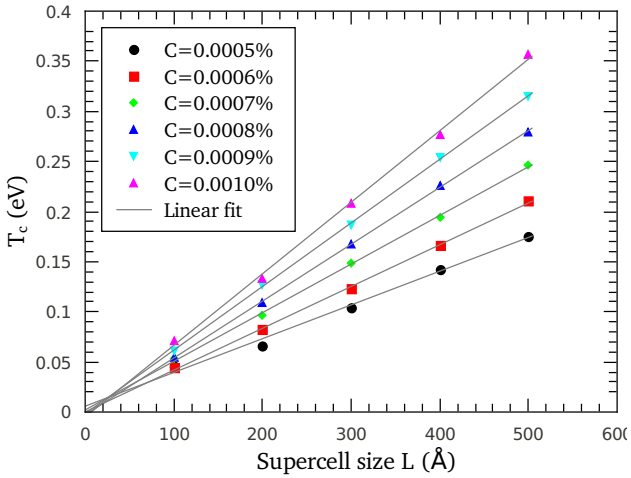

Fig. 4.23 Critical temperature against supercells graphite size.

Chapter 5

Dynamics of atomic hydrogen on graphite surface

5.1 Introduction

When atomic H is adsorbed on graphene the H atom bonds directly on top a C atom. Since the sublattices are completely equivalent, the adsorption process is blind to the sublattice index.

A recent experiment of the hydrogen deposition has been done using scanning tunneling microscope (STM), by Ivan Brihuega et. al., they deposited atomic hydrogen from a hot hydrogen atom beam source on a pristine graphite surface. Figure (5.1), showing the general morphology of the samples for different H coverages. For H-H distances $>$ 1nm all triangular bright features are equally oriented, with all H atoms chemisorbed on β sublattice. For shorter distances some of the triangular features are rotated 60°, as correspond to H atoms chemisorbed in the opposite α sublattice (see red triangles outlined in the zoom-in panels). For such short H-H distances the energy gain for H chemisorption on β sites may not be enough to compensate the favorable AB configurations.

As can be appreciated in Figure (5.2), for H-H separations $\geq$1nm, all triangular bright features point in the same direction, which implies that all H atoms are chemisorbed on the same atomic sublattice. In particular, this happens on sublattice β, where carbon atoms have no carbon underneath.

Ivan Brihuega et. al., have revealed that, when atomic H is deposited on a graphite surface at low concentrations (typically below 10%) and at room temperature, a single sublattice of the surface graphene layer hosts all the H atoms. Only when the concentration is increased the complementary sublattice becomes, logically, progressively populated. This remarkable result has important implications since it is known that a H atom induces a net magnetic moment of

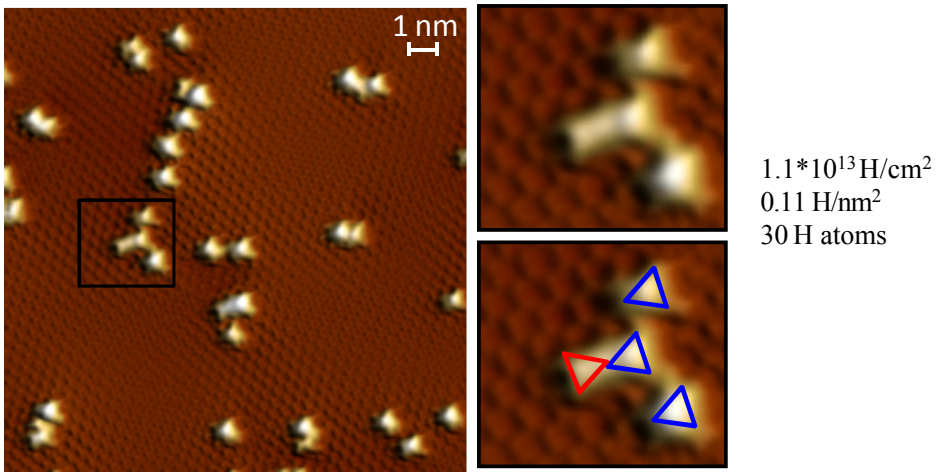

Fig. 5.1 Atomically resolved STM images showing the general morphology of the samples for different H coverages.

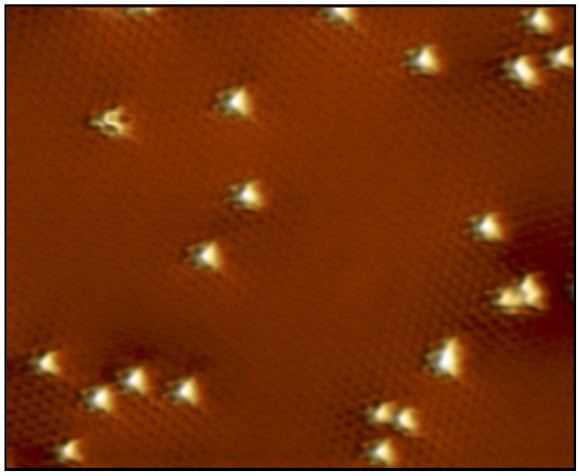

Fig. 5.2 STM topography, showing the general morphology of the graphite surface after H deposition all triangular bright features are equally oriented, corresponding to H atoms chemisorbed on the same β sublattice.

1 μ_B on the host graphene layer. When all the atoms sit on the same sublattice the resulting electronic ground state is a ferromagnetic state with a typically very high Curie temperature for a wide range of concentrations.

5.2 Hydrogen atom on a graphene bilayer

5.2.1 Desorption

On graphene, H atoms are known to preferentially adsorb on top of C atoms. Adsorption of H on a graphene bilayer is not different in this regard. In Figure 5.3 we present the atomic structure for the adsorption on a graphene bilayer as obtained from our DFT calculations. Here the upper layer is allowed to relax while the carbon atoms in the lower layer were fixed at their equilibrium position, simulating the presence of underlying layers of graphite. The characteristic sp^3 re-hybridization induced by the H atom is patent for both A and B adsorption sites. However, due to the Bernal stacking, the sublattices are not equivalent any more and the atomic structures are not identical. We will denote the two different adsorption sites as α and β when referring to the bilayer from now on.

The DFT binding energy curves for both adsorption sites are shown in Figure 5.4. Both curves exhibit two different minima or adsorption states: a strongly bound chemisorption state and a weakly bound physisorption state. The physisorption state can be appreciated in both curves as a shallow mimimum around 2.5 Å. In between both minima the magnetic moment induced on the substrate by the H atom transfers between substrate and H. The abruptness of this transition is likely to be an artefact of the mean-field theory which could be smoothed by more sophisticated (but impractical) methods which do not break spin symmetry[**?**]. Notice that the activation barrier separating the chemisorption from the physisorption minima is slightly smaller than the binding energy. We will take this barrier as the desorption activation barrier, ΔE_d^α, and ΔE_d^β. The physisorption minimum is so shallow that, to any practical purpose, it can be safely ignored from now on.

In order to illustrate the sensitivity to the supercell size, we present the results for the 4x4 and 5x5 cases. Although fairly similar, significant differences can be appreciated. The calculated chemisorption energies $[E_\alpha > E_\beta]$ differ by an increasing number which approaches ≈ 85 meV in the limit of isolated atoms or infinite cells. The desorption activation barriers, although slightly smaller than the chemisorption energies, behave similarly with the size of the supercell. Since these quantities appear in the exponential factor of the probabilities in Eq. **??**, an accurate estimate of these is mandatory. The values extrapolated to the infinite

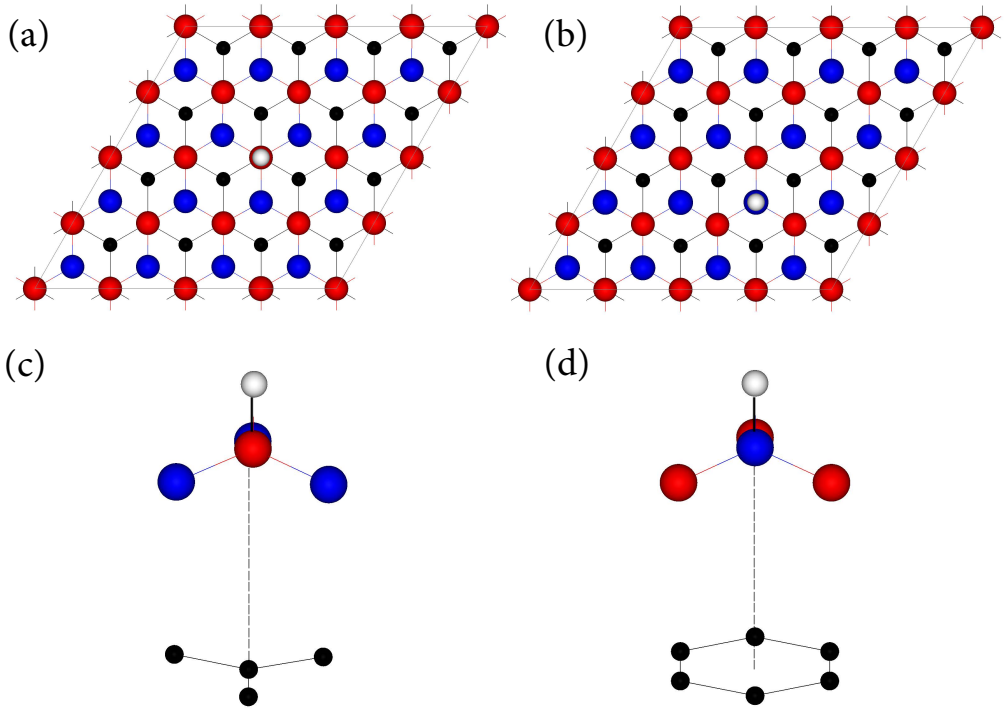

Fig. 5.3 Atomic structure of H on bilayer graphene (a) α and (b) β sites top view for a $4 \times 4 \times 1$ supercell, and (c) α and (d)β sites side view.

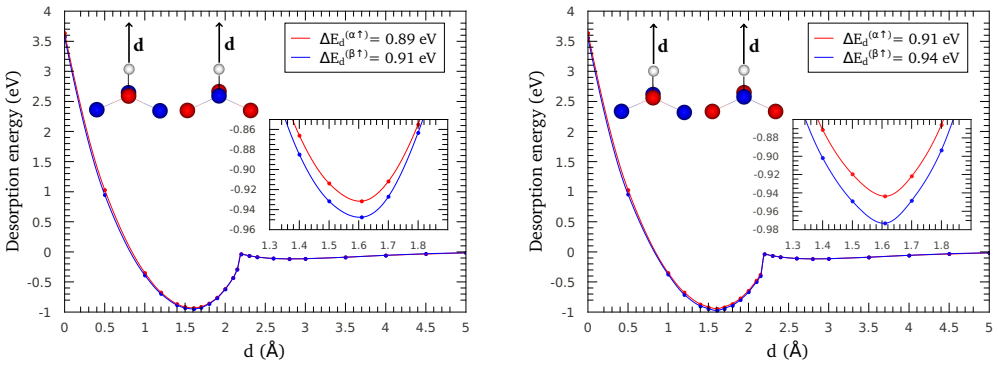

(a) 4x4 supercell bilayer graphene (b) 5x5 supercell bilayer graphene

Fig. 5.4 Desorption energy (E, eV) of hydrogen atom on α and β sites over bilayer graphene surface.

supercell limit, which will be used in the OKMC, are shown in Table 5.2.

5.2.2 Migration

The energy landscape of the H atom moving across the surface of the bilayer is shown in Figure 5.7. This has been obtained by fixing the xy (plane) coordinates of the H atom, letting relax the z (height) and all the other coordinates of the C atoms of the top graphene layer. Several conclusions can be drawn from this graph. First, there is a shallow adsorption local minimum in the center of the hexagons of the order of 200 meV. The depth is much smaller that of the minima at C sites. While this minimum might host atoms for short periods of time, we will ignore them in what follows. Second, and most importantly, the path that a H atom follows from α to β sites is "protected" in the sense that all along the C-C bond there are lateral energy barriers preventing the H atom from leaving the path and falling into the hollow site minimum (see Fig. 5.6 for details). Also, the H atom does not desorb half-way through between C atoms since the binding energy there is negative. Figure 5.5 shows the energy curve through this path. Again, noticeable differences in the activation barrier height, $\Delta E_m^{\alpha\to\beta}$, for different cell sizes can be seen. The value of this barrier extrapolated to an infinite cell size is given in Table 5.2.

5.2.3 Other activated processes

The activation energies discussed above dramatically change when the H atom is close to other H atoms. A thorough study for many cluster possibilities on monolayer graphene can be found in Ref. [146] and serves of guidance for the following considerations. Here we will make use

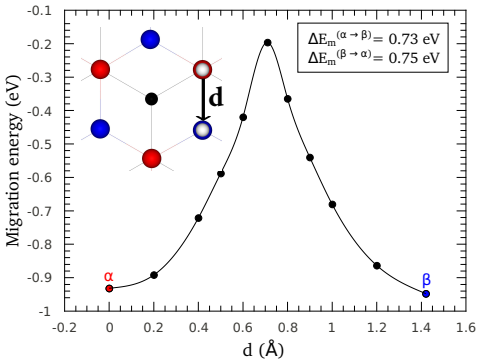

(a) 4x4 supercell bilayer graphene

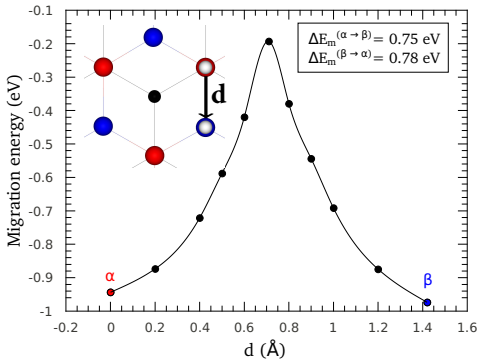

(b) 5x5 supercell bilayer graphene

Fig. 5.5 Diffusion energy (E, eV) of moving hydrogen atom from α to β sites over bilayer graphene surface.

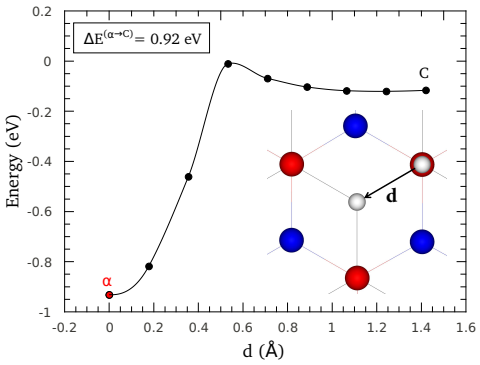

(a) Moving H atom from α site to the center

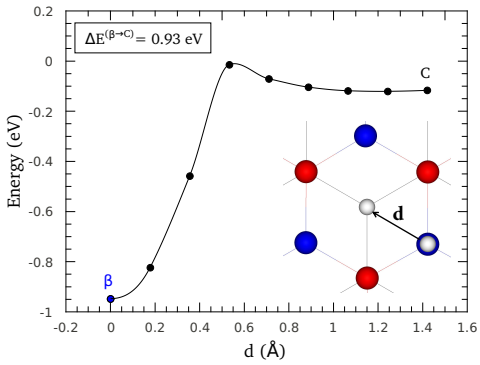

(b) Moving H atom from β site to the center

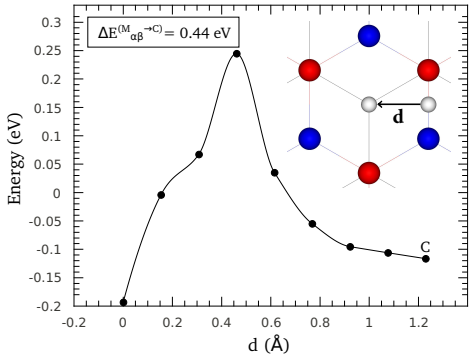

(c) Moving H atom from the halfway α β sites to the center

Fig. 5.6 Energy (E, eV) of moving hydrogen atom from α, β, and the halfway sites to the center of hexagonal ring over bilayer graphene surface.

of the detailed energetics of two H atoms on graphene [**?**]) to make reasonable estimates of how the vicinity of other atoms modify these barriers. Our basic assumption is that when a H atom attempts to break an A-B bond (two H atoms sitting on nearest-neighbour C atoms) a pair binding energy $E_b \approx 1.4$ eV has to be paid. This is the energy required to change an A-B H pair into an A–A or B–B configuration as shown in Fig.**??**. The migration activation barrier will now be given by:

$$\Delta_{m'}^{\alpha(\beta)} = \Delta_m^{\alpha(\beta)} + E_b \tag{5.1}$$

and the desorption barrier by

$$\Delta_{d'}^{\alpha(\beta)} = \Delta_d^{\alpha(\beta)} + E_b. \tag{5.2}$$

We will assume that these values hold regardless of the number of atoms and form of the cluster from where the H atom attempts to detach itself. Also we will ignore the binding energy or attraction exerted at distances longer than a single C-C bond, in particular the strong binding between H atoms in the A—B configuration (see Fig. **??**. Finally, we will assume that the attempt rates are not modified by the presence of other H atoms. When interpreting the results one should thus keep in mind that these simplifications might reduce the likelihood for formation of clusters.

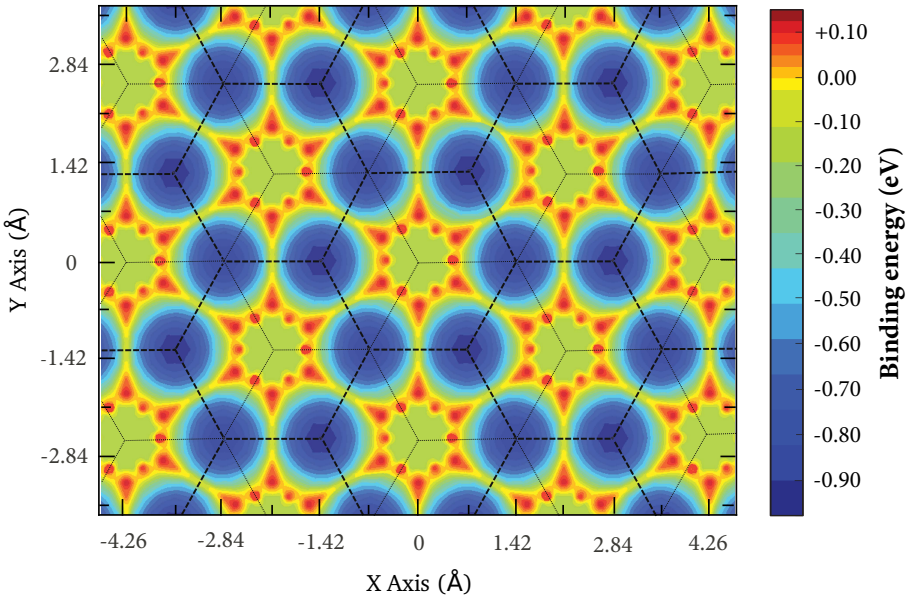

Fig. 5.7 Energy map (E, eV) of moving hydrogen atom on bilayer graphene surface.

5.2.4 Vibrational frequencies

Important characteristics of impurities in materials are their vibrational frequencies, which are known to be dependent on the particular site occupied by a given impurity in the crystal and on its interactions with the nearby host atoms. In our calculations, the question arises whether the oscillator frequencies associated to an impurity located at a given site can be extracted by assuming the host carbon atoms fixed in the relaxed geometry. This is in fact a method frequently employed to calculate vibrational frequencies of impurities in materials.

To calculate these vibrational frequencies, at the outset, we have discussed the lowest-energy configuration for the hydrogenic impurities on a bilayer graphene sheet, as derived from our DFT calculations on the two α, and β sites. The hydrogen binds to an carbon atom, which relaxes out of the sheet plane by 0.48 Å, with a bond distance between carbon and hydrogen of 1.13 Å, as shown in Figure (5.3). These results are in line with those reported in the literature, and in particular with the breaking of a π bond and producing an additional σ bond, changing the hybridization of the involved C atom from sp^2 to sp^3. Assuming the host C atoms fixed in the relaxed geometry, one can calculate vibrational frequencies for the impurity in a harmonic approximation. Thus, we find for hydrogen a frequencies on the two α, and β bilayer graphene sites:

Table 5.1 Hydrogen frequency $\omega_{\perp}$ for stretching of the C-H bond (perpendicular to the bilayer graphene surface) and $\omega_{\parallel}$ for vibrations parallel to the bilayer graphene surface (twofold degenerate).

	$\omega_{\perp}(cm^{-1})$	$\omega_{\parallel}(cm^{-1})$
H on α site	2368.1969	1161.3874
H on β site	2371.4863	1164.3152

5.2.5 Desorption and migration rate

The jump frequencies for the the hydrogenic impurities can be deduced from the corresponding υ by the equation:

$$\upsilon = \upsilon_{\circ} * exp(\frac{-\Delta E_b}{k_B T}) \tag{5.3}$$

where $\upsilon_{\circ}$ is the vibration frequency , and ΔE_b is the energy barrier.

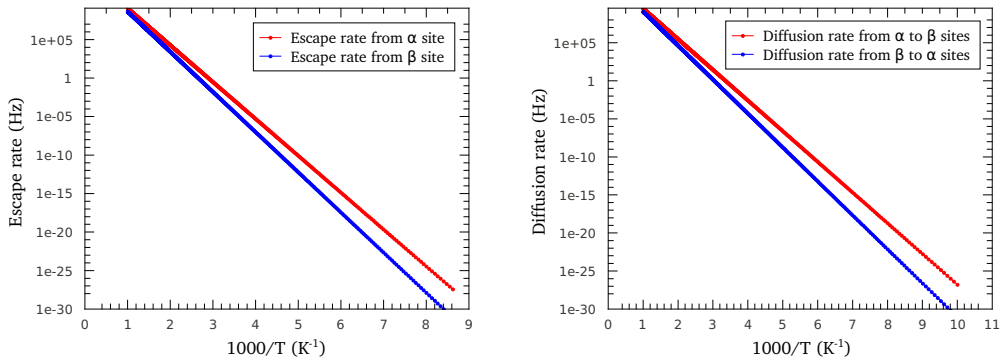

(a) Escape rate (b) Diffusion rate

Fig. 5.8 Escape, and diffusion rate of hydrogen atom on bilayer graphene surface.

Shown in Figure (5.8), is the rate for the hydrogenic impurities for desorption and migration over bilayer surface as a function of the inverse temperature. Data were derived from the desorption and migration energy barriers displayed in Figure (5.4, and 5.5), using the Hydrogen vibrational frequencies $\omega_{\perp}$ and $\omega_{\parallel}$ in Table (5.1).

At T= 500 K, the jump rate for hydrogen results to be larger than that for deuterium, which in turn is higher than that found in the classical limit, as expected from the change in effective free-energy barrier discussed above. At 300 K, the jump rate for hydrogen is found to be 11.6 s^{-1}, about 20 times larger than the value found in the classical calculation. The influence of quantum effects on hydrogen diffusivity increases as temperature is lowered, as could be expected; but the jump rate itself becomes very small. In fact, at 200 K, the calculated rate for hydrogen kH is less than 10^{-4} s^{-1}. On the contrary, at high temperatures kH converges to the classical result, and the difference between both becomes unobservable at T larger than 1000 K. At this temperature, we find kH= 2.0×109 s^{-1}.

5.2.6 Pair-wise interaction between H atoms

Another necessary ingredient in the OKMC calculations is the interaction energy between pairs of H atoms. This has been calculated before [**?**]. Here, for completeness, we present the result of our calculation for a graphene mono-layer. As can be seen, the interaction energy strongly depends on whether the pair of atoms is placed on the same or different sublattices. When situated on the same sublattice the binding energy is negligible. However, when placed on different sublattices the binding energy can be as high as 1.4 eV at near-neighbour distance.

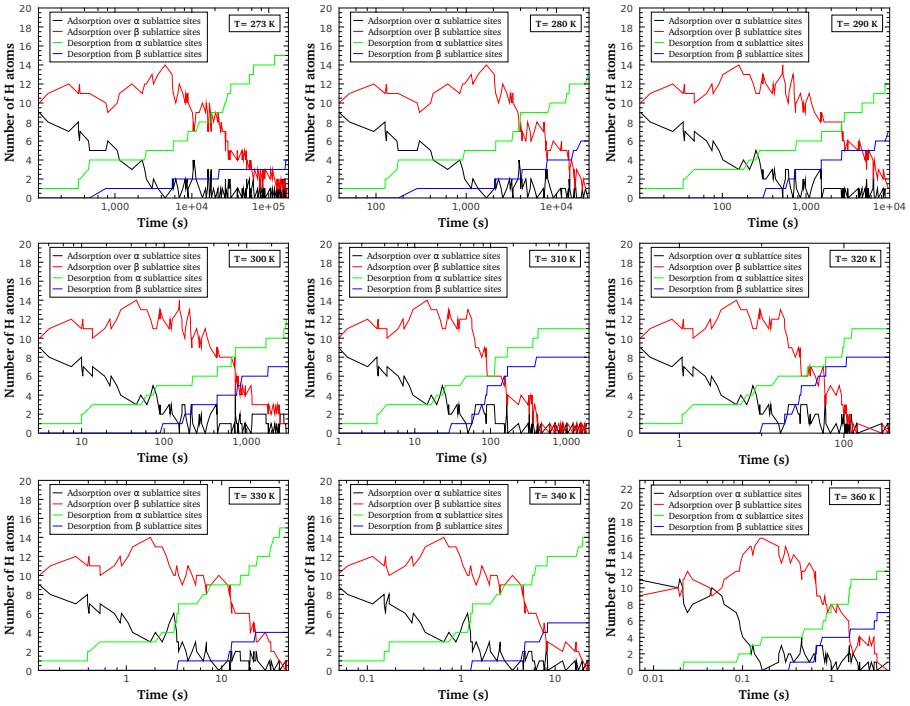

Fig. 5.9 Distribution of hydrogen lifetime over graphite surface at 273, 280, 290, 300, 310, 320, 330, 340, and 360 K with C=0.005 (H_α/C_α site), and C=0.005 (H_β/C_β site).

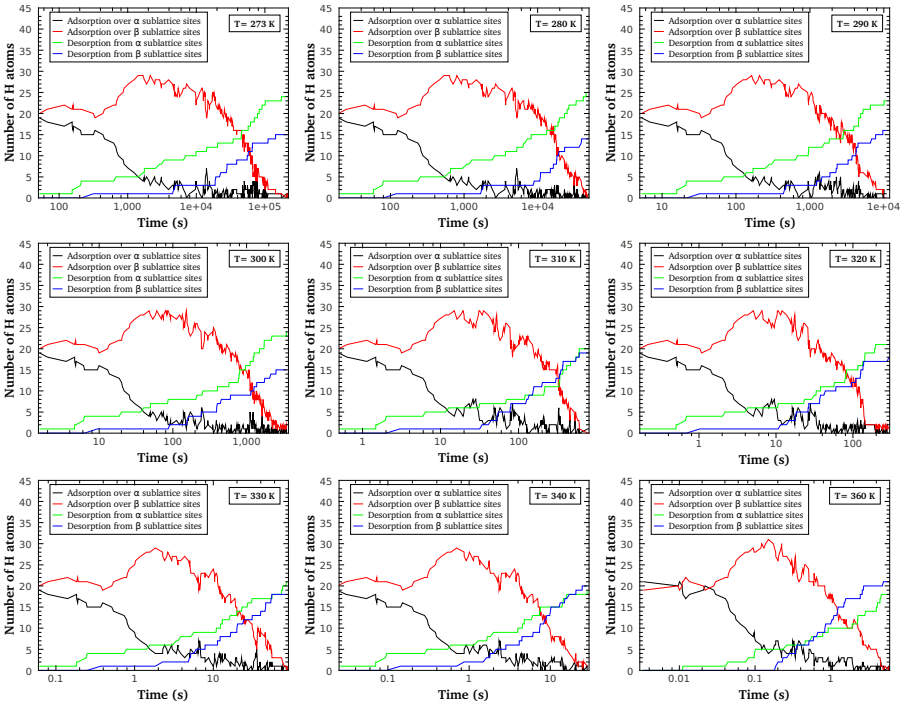

Fig. 5.10 Distribution of hydrogen lifetime over graphite surface at 273, 280, 290, 300, 310, 320, 330, 340, and 360 K with C=0.01 (H_α/C_α site), and C=0.01 (H_β/C_β site).

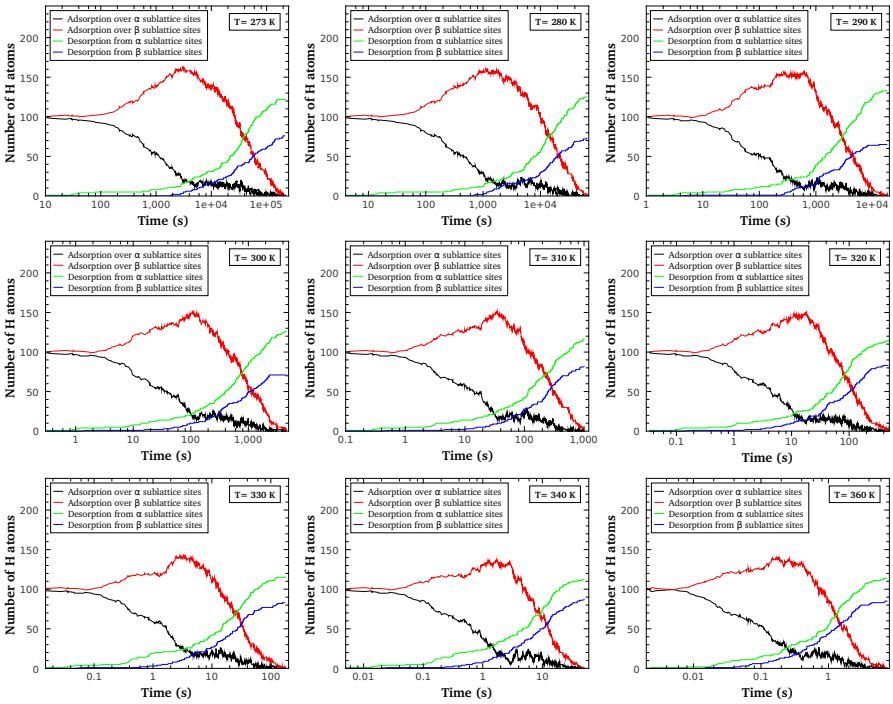

Fig. 5.11 Distribution of hydrogen lifetime over graphite surface at 273, 280, 290, 300, 310, 320, 330, 340, and 360 K with C=0.05 (H_α/C_α site), and C=0.05 (H_β/C_β site).

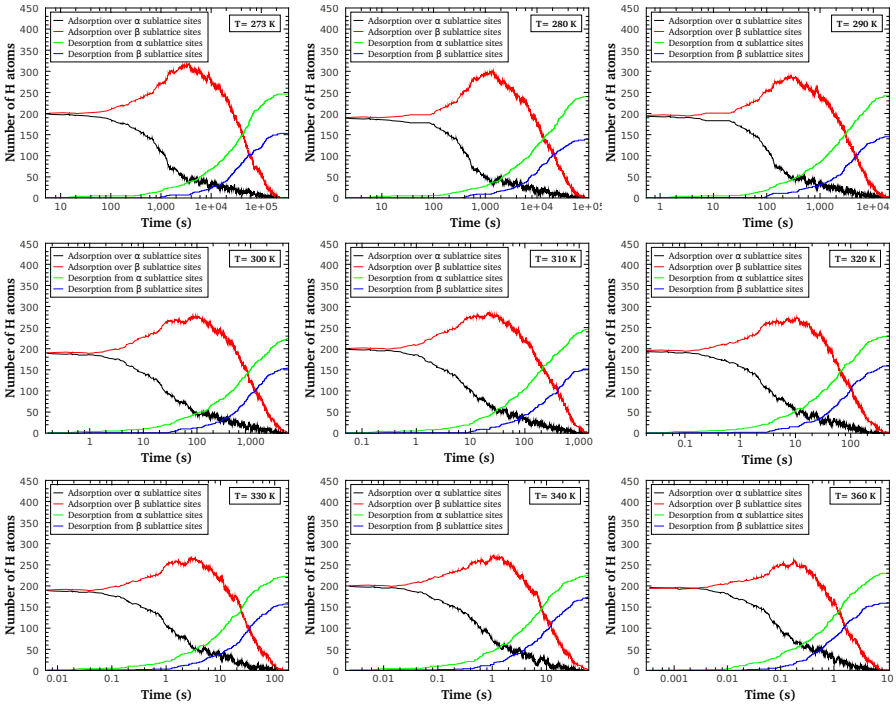

Fig. 5.12 Distribution of hydrogen lifetime over graphite surface at 273, 280, 290, 300, 310, 320, 330, 340, and 360 K with C=0.1 (H_α/C_α site), and C=0.1 (H_β/C_β site).

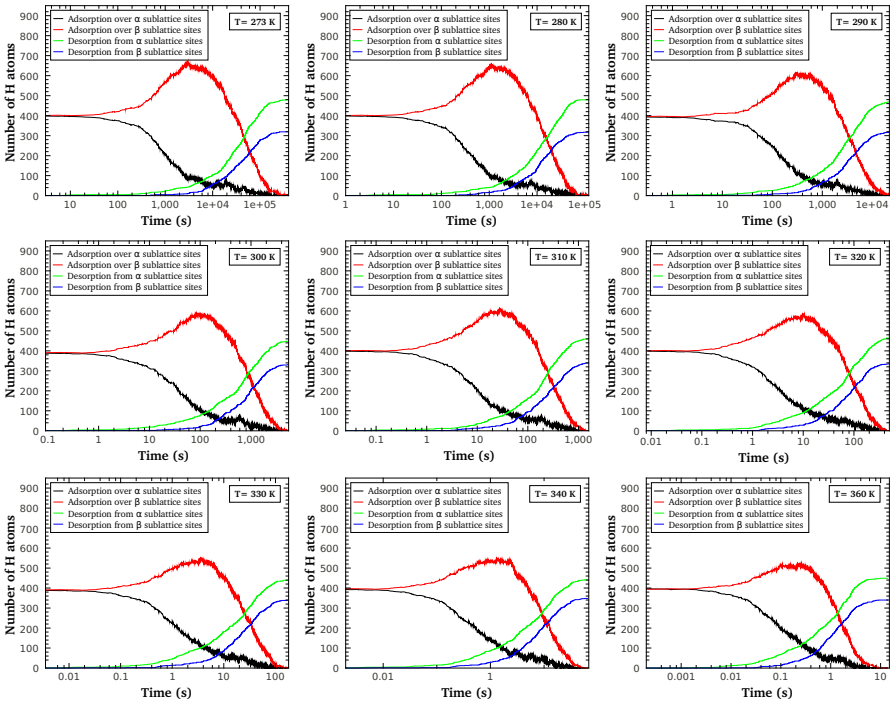

Fig. 5.13 Distribution of hydrogen lifetime over graphite surface at 273, 280, 290, 300, 310, 320, 330, 340, and 360 K with C=0.2 (H_α/C_α site), and C=0.2 (H_β/C_β site).

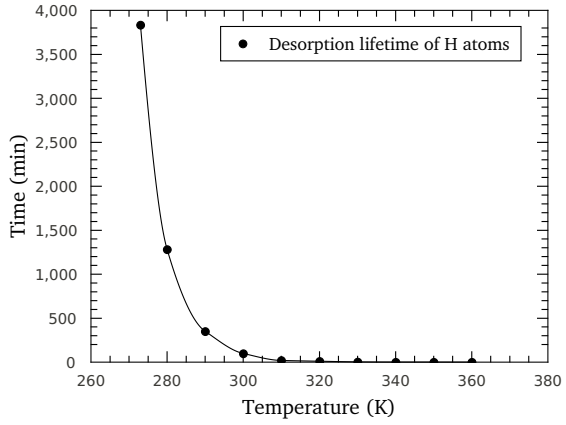

Fig. 5.14 Desorption lifetime of hydrogen atoms over graphite surface at 273, 280, 290, 300, 310, 320, 330, 340, 350, and 360 K with C=0.05 (H_α/C_α site), and C=0.05 (H_β/C_β site).

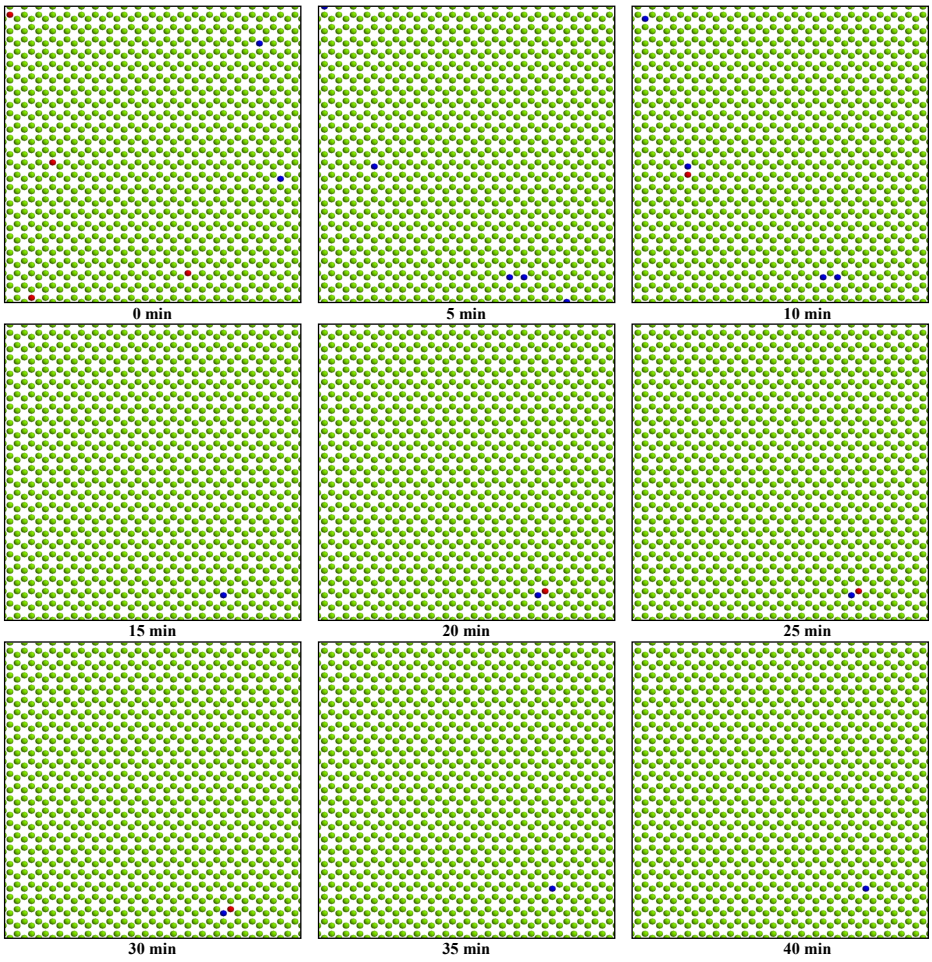

Fig. 5.15 Screenshot of hydrogen lifetime distribution over graphite surface at 300 K with C=0.005 (H_α/C_α site), and C=0.005 (H_β/C_β site).

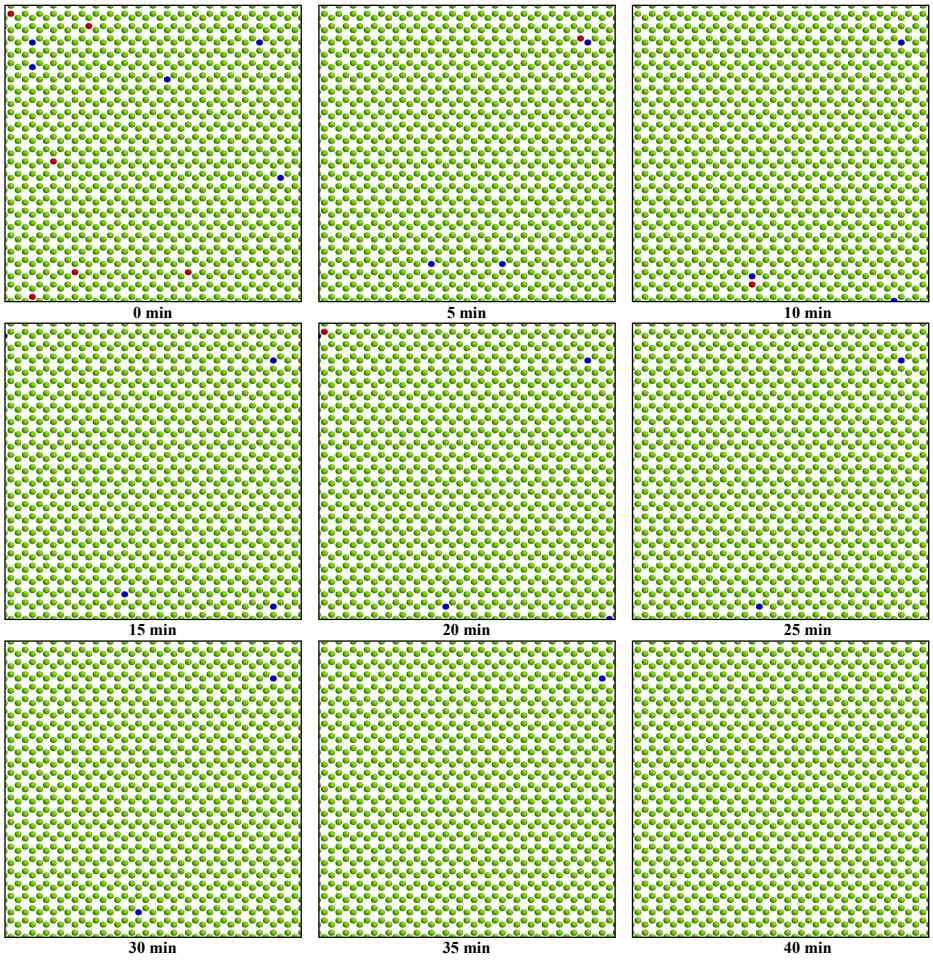

Fig. 5.16 Screenshot of hydrogen lifetime distribution over graphite surface at 300 K with C=0.010 (H_α/C_α site), and C=0.010 (H_β/C_β site).

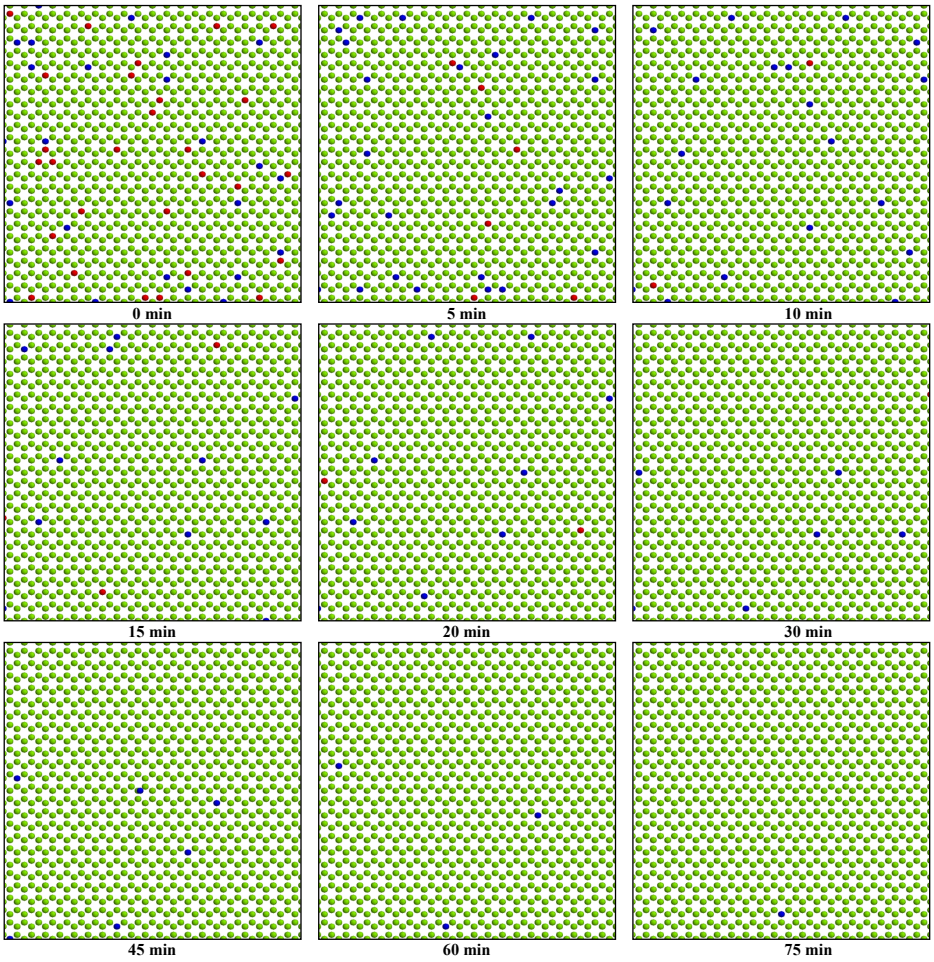

Fig. 5.17 Screenshot of hydrogen lifetime distribution over graphite surface at 300 K with C=0.050 (H_α/C_α site), and C=0.050 (H_β/C_β site).

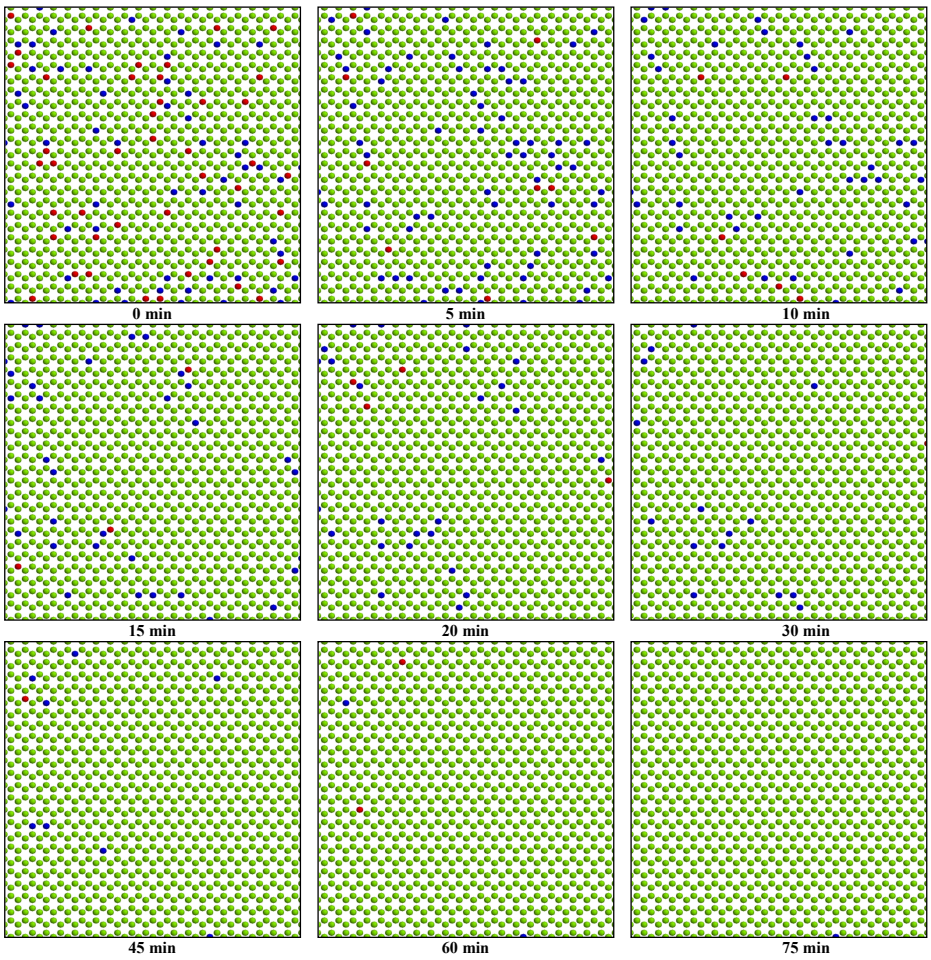

Fig. 5.18 Screenshot of hydrogen lifetime distribution over graphite surface at 300 K with C=0.100 (H_α/C_α site), and C=0.100 (H_β/C_β site).

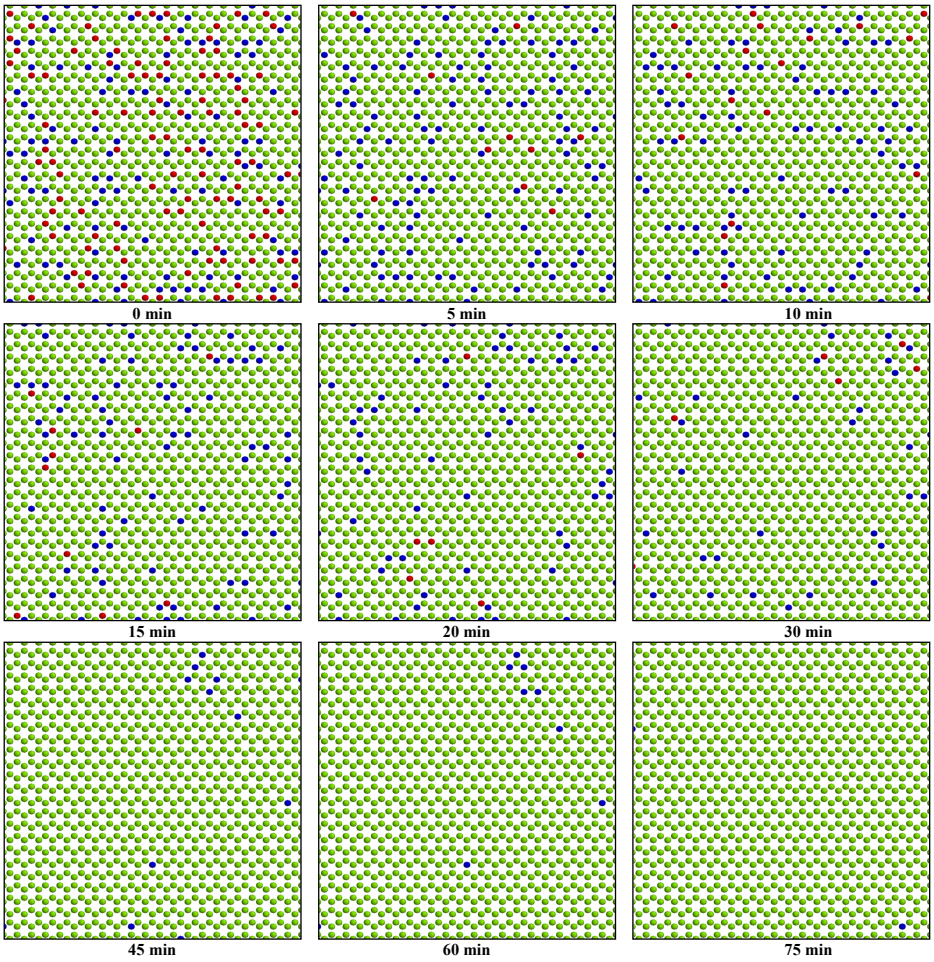

Fig. 5.19 Screenshot of hydrogen lifetime distribution over graphite surface at 300 K with C=0.200 (H_α/C_α site), and C=0.200 (H_β/C_β site).

5.3 Kinetic Monte Carlo results

The conclusion that can be drawn from the previous calculations is that H atoms can migrate from α to β sites with a significantly different probability which will certainly favour a higher concentration of H atoms on one sublattice over the other. The question that needs to be addressed is how long it takes and whether or not this occurs before all H atoms desorb or group together forming clusters which are very stable. This question can be answered through OKMC calculations. In order to study the dynamics of H atoms on graphite, we have implemented a kinetic Monte Carlo algorithm that includes a total of seven events, as shown in table 5.2. Initially, a random distribution of H atoms for the concentration to be studied is created on a graphene lattice. A H atom can either jump to a neighboring location or desorbe from the graphene layer. The rate of migration is given by the migration energies calculated using DFT, as explained above, and by the attempt frequency, calculated from the energy curves near the minima. Both the migration energy as well as the attempt frequency for migration will depend on the location of the H atom, an α or a β site. The values used in the calculations presented here are given in table 5.2.

After every H jump it is necessary to check if other H atoms are located in the vicinity. We consider the formation of a H-H cluster when two H atoms are located first or second nearest neighbours from each other on different sublattices. These H-H clusters are considered immobile in the calculation and also can not desorb from the surface. However, they can dissociate by a H jumping to a neighboring site. The dissociation energy would be the sum of the binding energy between the two H atoms and the migration energy. We consider the possibility of a H atom migrating to an α site or to a β site, as shown in table 5.2.

The second type of event that a H atom can perform is the desorption from the surface. The activation energy for desorption, as well as the attempt frequency are also given in table 5.2.

This algorithm allows us to follow the concentration of H atoms in alpha and beta sites as a function of time, the number of H atoms that are being desorbed from the graphene layer and the number of clusters formed. We have performed calculations for different initial H concentrations and different temperatures.

Table 5.2 Events included in the kinetic Monte Carlo calculation. Activation energy (in eV) and attempt frequencies (in s^{-1}) for each type of event, as obtained from the DFT calculations.

Migration from A site	0.80	3×3.5e13
Migration from B site	0.89	3×3.5e13
Desorption from a A site	0.95	7e13
Desorption form a B site	1.04	7e13
Formation of a H-H cluster	diffusion limited	
Dissociation of a H-H to A	2.20	3.5e13
Dissociation of a H-H to B	2.29	3.5e13

Appendix A

The description of the parameters used in the SIESTA code

Our calculations are based on the density functional theory (DFT) [108, 109] framework using the SIESTA code [147, 148]. We are mostly interested here in multilayer graphene and graphite where dispersion (van der Waals) forces due to long-range electron correlation effects play a key role in the binding of the graphene layers. Therefore we use the exchange and correlation nonlocal van der Waals density functional (vdW-DF) of Dion et al. [149] as implemented by Román-Pérez and Soler [150, 151].

To describe the interaction between the valence and core electrons we used norm-conserved Troullier-Martins pseudopotentials . The cutoff radii were 1.56 for both the s and p components in C, and 1.25 for the s component in H [152]. The pseudopotentials were generated using the following reference

configurations: $2s^2\ 2p^2$ for C, and $1s^1$ for H

To expand the wavefunctions of the valence electrons, a double-ζ plus polarization (DZP) basis set was used [153]. We experimented with a variety of LCAO basis sets and found that, for both graphene and graphite, the DZP produced high-quality results.

The plane-wave cutoff energy for the wavefunctions was set to 500 Ryd. For the Brillouin zone sampling we use $4 \times 4 \times 2$ Monkhorst-Pack k-mesh for the $12 \times 12 \times 1$ single-layer and bilayer graphene supercells. And we use the Brillouin zone sampling $100 \times 100 \times 2$ Monkhorst-Pack k-mesh for the $2 \times 2 \times 1$ single-layer and bilayer graphene supercells.

We have also checked that the results are well converged with respect to the real space grid. Regarding the atomic structure, the atoms are allowed to relax down to force tolerance of 0.005 eV/Å.

For charged systems, all supercells are large enough to ensure that the vacuum space is at

least 99 Å so that the interaction between functionalized graphene layers and their periodic images can be safely avoided [154]. The amount of charging is positive charging, i.e. electron depletion (Q $>$ 0), in units of electron (e) per unit cell. Average surface charge is specified as (σ = Q/no. of atoms), i.e the charge per the number of atoms in the surface layer (the charged layers).

For the hydrogen-graphitic system, the spin polarization was included in the calculations because, as discussed in the introduction, hydrogenation is expected to induce magnetism in the single-layer and bilayer graphene. All supercells are large enough to ensure that the vacuum space is at least 25 Å so that the interaction between functionalized graphene layers and their periodic images can be safely avoided.

References

[1] P.Y. Bruice. *Organic chemistry*. Prentice Hall, 2001. ISBN 9780130178589. URL http://books.google.es/books?id=llwvAQAAIAAJ. 1

[2] Linus. Pauling. The nature of the chemical bond. application of results obtained from the quantum mechanics and from a theory of paramagnetic susceptibility to the structure of molecules. *Journal of the American Chemical Society*, 53(4):1367–1400, 1931. doi: 10.1021/ja01355a027. URL http://pubs.acs.org/doi/abs/10.1021/ja01355a027.

[3] R. Saito, G. Dresselhaus, and S. Dresselhaus. *Physical Properties of Carbon Nanotubes*. Imperial College Press, 1998. ISBN 9781860940934. URL http://books.google.fr/books?id=w5oHCWhA2EQC. 1, 20, 23

[4] S. Dresselhaus, G. Dresselhaus, and P.C. Eklund. *Science of Fullerenes and Carbon Nanotubes*. Academic Press, 1996. ISBN 9780122218200. URL http://books.google.fr/books?id=YpOYYbquYgYC. 2

[5] J. Steinbeck, G. Braunstein, M. S. Dresselhaus, T. Venkatesan, and D. C. Jacobson. A model for pulsed laser melting of graphite. *Journal of Applied Physics*, 58(11):4374, 1985. ISSN 00218979. doi: 10.1063/1.335527. URL http://link.aip.org/link/JAPIAU/v58/i11/p4374/s1&Agg=doi. 2

[6] JM Zazula. On graphite transformations at high temperature and pressure induced by absorption of the LHC beam. *CERN-LHC-Project-Note-78*, 1997. URL http://cern.ch/lbruno/documents/Bibliography/LHC_Note_78.pdf. 3

[7] David M. Haaland. Graphite-liquid-vapor triple point pressure and the density of liquid carbon. *Carbon*, 14(6):357 – 361, 1976. ISSN 0008-6223. doi: 10.1016/0008-6223(76)90010-5. URL http://www.sciencedirect.com/science/article/pii/0008622376900105. 3

[8] A.I. Savvatimskiy. Measurements of the melting point of graphite and the properties of liquid carbon (a review for 1963–2003). *Carbon*, 43(6):1115 – 1142, May 2005. ISSN 0008-6223. doi: 10.1016/j.carbon.2004.12.027. URL http://www.sciencedirect.com/science/article/pii/S0008622305000291. 3

[9] A. GREENVILLE WHITTAKER. The controversial carbon solid–liquid–vapour triple point. *Nature*, 276:695–696, December 1978. doi: 10.1038/276695a0. URL http://dx.doi.org/10.1038/276695a0. 3

References

[10] M.J. O'Connell. *Carbon Nanotubes: Properties And Applications*. CRC/Taylor & Francis, 2006. ISBN 9780849327483. URL http://books.google.fr/books?id=xdhh0ryJRc8C. 3, 4, 5

[11] C. Kittel. *Introduction To Solid State Physics*. Wiley, 2005. ISBN 9780471415268. URL http://books.google.fr/books?id=kym4QgAACAAJ. 3, 4

[12] L.S. Pan and D.R. Kania. *Diamond: Electronic Properties and Applications*. Electronic Materials: Science and Technology Series. Kluwer Academic, 1994. ISBN 9780792395249. URL http://books.google.es/books?id=ZtfFEoXkU8wC. 4

[13] G. Davies and INSPEC (Information service). *Properties and growth of diamond*. EMIS datareviews series. INSPEC, the Institution of Electrical Engineers, 1994. ISBN 9780852968758. URL http://books.google.es/books?id=RkFRAAAAMAAJ. 4

[14] P. Morgan. *Carbon Fibers and Their Composites*. Materials Engineering Series. Taylor & Francis, 2005. ISBN 9780824709839. URL http://books.google.es/books?id=-WSRxqMJcCoC. 4

[15] Stefan Hembacher, Franz J. Giessibl, Jochen Mannhart, and Calvin F. Quate. Revealing the hidden atom in graphite by low-temperature atomic force microscopy. *Proceedings of the National Academy of Sciences*, 100(22):12539–12542, 2003. doi: 10.1073/pnas.2134173100. URL http://www.pnas.org/content/100/22/12539.abstract. 4

[16] M. Meyyappan, editor. *Carbon Nanotubes: Science and Applications*. Taylor & Francis, 2004. ISBN 9780203494936. URL http://books.google.es/books?id=MgEJgwgyFBkC. 4

[17] J.-C. Charlier, J.-P. Michenaud, and X. Gonze. First-principles study of the electronic properties of simple hexagonal graphite. *Phys. Rev. B*, 46:4531–4539, Aug 1992. doi: 10.1103/PhysRevB.46.4531. URL http://link.aps.org/doi/10.1103/PhysRevB.46.4531. 4, 5

[18] A. W. Hull. A new method of x-ray crystal analysis. *Phys. Rev.*, 10:661–696, Dec 1917. doi: 10.1103/PhysRev.10.661. URL http://link.aps.org/doi/10.1103/PhysRev.10.661. 5

[19] J. D. Bernal. The structure of graphite. *Proceedings of the Royal Society of London. Series A*, 106(740):749–773, 1924. doi: 10.1098/rspa.1924.0101. URL http://rspa.royalsocietypublishing.org/content/106/740/749.short. 5

[20] R.W.G. Wyckoff. *Crystal Structures*. Number v. 4 in Crystal Structures. Interscience Publishers, 1960. URL http://books.google.es/books?id=jNwgAAAAMAAJ. 5, 10

[21] D. D. L. Chung. *Physics of graphite* by B. T. Kelly. *Acta Crystallographica Section A*, 39(1):192, Jan 1983. doi: 10.1107/S0108767383000422. URL http://dx.doi.org/10.1107/S0108767383000422. 5, 9, 10

[22] W.N. Reynolds. *Physical properties of graphite*. Elsevier materials science series. Elsevier Pub. Co., 1968. URL http://books.google.es/books?id=0vDvAAAAMAAJ. 5, 10

[23] Y. Miyajima, G. Adamopoulos, S. J. Henley, V. Stolojan, Y. Tison, E. Garcia-Caurel, B. Drevillon, J. M. Shannon, and S. R. P. Silva. Electronic state modification in laser deposited amorphous carbon films by the inclusion of nitrogen. *Journal of Applied Physics*, 104(6):063701, 2008. doi: 10.1063/1.2977718. URL http://link.aip.org/link/?JAP/104/063701/1. 5

[24] P. R. Wallace. The band theory of graphite. *Phys. Rev.*, 71:622–634, May 1947. doi: 10.1103/PhysRev.71.622. URL http://link.aps.org/doi/10.1103/PhysRev.71.622. 5, 20, 42

[25] A. H. Castro Neto, F. Guinea, N. M. R. Peres, K. S. Novoselov, and A. K. Geim. The electronic properties of graphene. *Rev. Mod. Phys.*, 81:109–162, Jan 2009. doi: 10.1103/RevModPhys.81.109. URL http://link.aps.org/doi/10.1103/RevModPhys.81.109. 5, 19

[26] P. Blaha, K. Schwarz, P. Sorantin, and S.B. Trickey. Full-potential, linearized augmented plane wave programs for crystalline systems. *Computer Physics Communications*, 59(2):399 – 415, 1990. ISSN 0010-4655. doi: http://dx.doi.org/10.1016/0010-4655(90)90187-6. URL http://www.sciencedirect.com/science/article/pii/0010465590901876. 7, 8

[27] David Tománek, Steven G. Louie, H. Jonathon Mamin, David W. Abraham, Ruth Ellen Thomson, Eric Ganz, and John Clarke. Theory and observation of highly asymmetric atomic structure in scanning-tunneling-microscopy images of graphite. *Phys. Rev. B*, 35:7790–7793, May 1987. doi: 10.1103/PhysRevB.35.7790. URL http://link.aps.org/doi/10.1103/PhysRevB.35.7790. 8

[28] M.P. Marder. *Condensed Matter Physics*. Wiley, 2010. ISBN 9780470949948. URL http://books.google.es/books?id=ijloadAt4BQC. 9

[29] Kazuhiko Izui and F. Eiichi Fujita. Observation of lattice defects in fission fragment-irradiated graphite. *Journal of the Physical Society of Japan*, 16(5):1032–1033, 1961. doi: 10.1143/JPSJ.16.1032. URL http://jpsj.ipap.jp/link?JPSJ/16/1032/. 9

[30] Toshihiro Tsuji, Hiroshi Irihama, and Kazushi Yamanaka. Observation of anomalous dislocation behavior in graphite
using ultrasonic atomic force microscopy. *Japanese Journal of Applied Physics*, 41 (Part 1, No. 2A):832–835, 2002. doi: 10.1143/JJAP.41.832. URL http://jjap.jsap.jp/link?JJAP/41/832/. 10

[31] P. A. Thrower and R. M. Mayer. Point defects and self-diffusion in graphite. *physica status solidi (a)*, 47(1):11–37, 1978. ISSN 1521-396X. doi: 10.1002/pssa.2210470102. URL http://dx.doi.org/10.1002/pssa.2210470102. 10

[32] Atsushi Ito, Ying Wang, Stephan Irle, Keiji Morokuma, and Hiroaki Nakamura. Molecular dynamics simulation of hydrogen atom sputtering on the surface of graphite with defect and edge. *Journal of Nuclear Materials*, 390–391(0):183 – 187, 2009. ISSN 0022-3115. doi: http://dx.doi.org/10.1016/j.jnucmat.2009.01.163. URL http://www.sciencedirect.com/science/article/pii/S0022311509000919. Proceedings

of the 18th International Conference on Plasma-Surface Interactions in Controlled Fusion Device Proceedings of the 18th International Conference on Plasma-Surface Interactions in Controlled Fusion Device. 10

[33] Cesare Pisani, Roberto Dovesi, and Paolo Carosso. Moderately-large-embedded-cluster approach to the study of local defects in solids. vacancy and substitutional impurities in graphite. *Phys. Rev. B*, 20:5345–5357, Dec 1979. doi: 10.1103/PhysRevB.20.5345. URL http://link.aps.org/doi/10.1103/PhysRevB.20.5345. 12

[34] Mattias Hjort and Sven Stafström. Modeling vacancies in graphite via the hückel method. *Phys. Rev. B*, 61:14089–14094, May 2000. doi: 10.1103/PhysRevB.61.14089. URL http://link.aps.org/doi/10.1103/PhysRevB.61.14089. 12

[35] C. H. Xu, C. L. Fu, and D. F. Pedraza. Simulations of point-defect properties in graphite by a tight-binding-force model. *Phys. Rev. B*, 48:13273–13279, Nov 1993. doi: 10.1103/PhysRevB.48.13273. URL http://link.aps.org/doi/10.1103/PhysRevB.48.13273. 12

[36] Efthimios Kaxiras and K. C. Pandey. Energetics of defects and diffusion mechanisms in graphite. *Phys. Rev. Lett.*, 61:2693–2696, Dec 1988. doi: 10.1103/PhysRevLett.61.2693. URL http://link.aps.org/doi/10.1103/PhysRevLett.61.2693. 12

[37] C D Latham, M I Heggie, M Alatalo, S Oberg, and P R Briddon. The contribution made by lattice vacancies to the wigner effect in radiation-damaged graphite. *Journal of Physics: Condensed Matter*, 25(13):135403, 2013. URL http://stacks.iop.org/0953-8984/25/i=13/a=135403. 12

[38] K.H. Lee, M. Causá, S.S. Park, C. Lee, Y. Suh, H.M. Eun, and D. Kim. Interpretation of scanning probe microscope image of the structure of atomic vacancy on graphite: ab initio periodic hartree–fock calculations. *Journal of Molecular Structure: {THEOCHEM}*, 506(1–3):297 – 301, 2000. ISSN 0166-1280. doi: http://dx.doi.org/10.1016/S0166-1280(00)00421-8. URL http://www.sciencedirect.com/science/article/pii/S0166128000004218. 12

[39] A. V. Krasheninnikov, K. Nordlund, M. Sirviö, E. Salonen, and J. Keinonen. Formation of ion-irradiation-induced atomic-scale defects on walls of carbon nanotubes. *Phys. Rev. B*, 63:245405, May 2001. doi: 10.1103/PhysRevB.63.245405. URL http://link.aps.org/doi/10.1103/PhysRevB.63.245405. 12

[40] Yuchen Ma, P O Lehtinen, A S Foster, and R M Nieminen. Magnetic properties of vacancies in graphene and single-walled carbon nanotubes. *New Journal of Physics*, 6 (1):68, 2004. URL http://stacks.iop.org/1367-2630/6/i=1/a=068. 12, 23

[41] P. O. Lehtinen, A. S. Foster, Yuchen Ma, A. V. Krasheninnikov, and R. M. Nieminen. Irradiation-induced magnetism in graphite: A density functional study. *Phys. Rev. Lett.*, 93:187202, Oct 2004. doi: 10.1103/PhysRevLett.93.187202. URL http://link.aps.org/doi/10.1103/PhysRevLett.93.187202. 12

[42] E. Rokuta, Y. Hasegawa, A. Itoh, K. Yamashita, T. Tanaka, S. Otani, and C. Oshima. Vibrational spectra of the monolayer films of hexagonal boron nitride and graphite on faceted ni(755). *Surface Science*, 427–428(0):97 – 101, 1999. ISSN

0039-6028. doi: http://dx.doi.org/10.1016/S0039-6028(99)00241-1. URL http://www.sciencedirect.com/science/article/pii/S0039602899002411. 12

[43] H Shioyama. Cleavage of graphite to graphene. *Journal of materials science letters*, 20(6):499–500, 2001. ISSN 0261-8028. doi: 10.1023/A:1010907928709. URL http://www.springerlink.com/index/V05U4GWN53826U1H.pdf.

[44] K. S. Novoselov, D. Jiang, F. Schedin, T. J. Booth, V. V. Khotkevich, S. V. Morozov, and A. K. Geim. Two-dimensional atomic crystals. *Proceedings of the National Academy of Sciences of the United States of America*, 102(30):10451–10453, 2005. doi: 10.1073/pnas.0502848102. URL http://www.pnas.org/content/102/30/10451.abstract. 39

[45] Y. H. Wu, T. Yu, and Z. X. Shen. Two-dimensional carbon nanostructures: Fundamental properties, synthesis, characterization, and potential applications. *Journal of Applied Physics*, 108(7):071301, 2010. ISSN 00218979. doi: 10.1063/1.3460809. URL http://link.aip.org/link/JAPIAU/v108/i7/p071301/s1&Agg=doi.

[46] Lisa M. Viculis, Julia J. Mack, and Richard B. Kaner. A chemical route to carbon nanoscrolls. *Science*, 299(5611):1361, 2003. doi: 10.1126/science.1078842. URL http://www.sciencemag.org/content/299/5611/1361.short.

[47] Rodney S. Ruoff. Chemically modified graphenes. *J. Mater. Chem.*, 21:3272–3272, 2011. doi: 10.1039/C1JM90012A. URL http://dx.doi.org/10.1039/C1JM90012A.

[48] Walt A. de Heer, Claire Berger, Xiaosong Wu, Phillip N. First, Edward H. Conrad, Xuebin Li, Tianbo Li, Michael Sprinkle, Joanna Hass, Marcin L. Sadowski, Marek Potemski, and Gérard Martinez. Epitaxial graphene. *Solid State Communications*, 143(1–2):92 – 100, 2007. ISSN 0038-1098. doi: http://dx.doi.org/10.1016/j.ssc.2007.04.023. URL http://www.sciencedirect.com/science/article/pii/S0038109807002980. Exploring graphene Recent research advances.

[49] You Min Chang, Hyungseok Kim, Ju Han Lee, and Yong-Won Song. Multilayered graphene efficiently formed by mechanical exfoliation for nonlinear saturable absorbers in fiber mode-locked lasers. *Applied Physics Letters*, 97(21):211102, 2010. ISSN 00036951. doi: 10.1063/1.3521257. URL http://link.aip.org/link/APPLAB/v97/i21/p211102/s1&Agg=doi.

[50] C-L Wong, M Annamalai, Z-Q Wang, and M Palaniapan. Characterization of nanomechanical graphene drum structures. *Journal of Micromechanics and Microengineering*, 20(11):115029, 2010. URL http://stacks.iop.org/0960-1317/20/i=11/a=115029.

[51] Zhihong Tang, Jing Zhuang, and Xun Wang. Exfoliation of graphene from graphite and their self-assembly at the oil-water interface. *Langmuir*, 26(11):9045–9049, 2010. doi: 10.1021/la9049082. URL http://pubs.acs.org/doi/abs/10.1021/la9049082. PMID: 20170133.

[52] Abhay Shukla, Rakesh Kumar, Javed Mazher, and Adrian Balan. Graphene made easy: High quality, large-area samples. *Solid State Communications*, 149(17–18):718 – 721, 2009. ISSN 0038-1098. doi: http://dx.doi.org/10.1016/j.ssc.2009.02.007. URL http://www.sciencedirect.com/science/article/pii/S0038109809000829.

[53] H Hiura, TW Ebbesen, J Fujita, K Tanigaki, and T Takada. Role of sp3 defect structures in graphite and carbon nanotubes. *Nature*, 367(6459):148 – 151, 1994. doi: http://dx.doi.org/10.1038/367148a0. URL http://www.nature.com/nature/journal/v367/n6459/abs/367148a0.html.

[54] Kostya Novoselov. Beyond the wonder material. *Physics World*, 22(August 2009): 27–30, 2009. URL http://www.condmat.physics.manchester.ac.uk/fullpub/PhysicsWorld_2009beyondthewondermaterial.pdf.

[55] H.-V. Roy, C. Kallinger, B. Marsen, and K. Sattler. Manipulation of graphitic sheets using a tunneling microscope. *Journal of Applied Physics*, 83(9):4695–4699, 1998. doi: 10.1063/1.367257. URL http://link.aip.org/link/?JAP/83/4695/1.

[56] Sungjin Park, Jinho An, Jeffrey R. Potts, Aruna Velamakanni, Shanthi Murali, and Rodney S. Ruoff. Hydrazine-reduction of graphite- and graphene oxide. *Carbon*, 49(9):3019 – 3023, 2011. ISSN 0008-6223. doi: http://dx.doi.org/10.1016/j.carbon.2011.02.071. URL http://www.sciencedirect.com/science/article/pii/S0008622311001965.

[57] O. O. Kit, T. Tallinen, L. Mahadevan, J. Timonen, and P. Koskinen. Twisting graphene nanoribbons into carbon nanotubes. *Phys. Rev. B*, 85:085428, Feb 2012. doi: 10.1103/PhysRevB.85.085428. URL http://link.aps.org/doi/10.1103/PhysRevB.85.085428.

[58] Daniel Gunlycke and Paul E. Sheehan. Local peeling of graphene. *Science*, 331(6021): 1146–1147, 2011. doi: 10.1126/science.1200779. URL http://www.sciencemag.org/content/331/6021/1146.short.

[59] Xuekun Lu, Minfeng Yu, Hui Huang, and Rodney S Ruoff. Tailoring graphite with the goal of achieving single sheets. *Nanotechnology*, 10(3):269, 1999. URL http://stacks.iop.org/0957-4484/10/i=3/a=308.

[60] Ayrat Dimiev, Dmitry V. Kosynkin, Alexander Sinitskii, Alexander Slesarev, Zhengzong Sun, and James M. Tour. Layer-by-layer removal of graphene for device patterning. *Science*, 331(6021):1168–1172, 2011. doi: 10.1126/science.1199183. URL http://www.sciencemag.org/content/331/6021/1168.abstract.

[61] S. Basu and P. Bhattacharyya. Recent developments on graphene and graphene oxide based solid state gas sensors. *Sensors and Actuators B: Chemical*, 173(0):1 – 21, 2012. ISSN 0925-4005. doi: http://dx.doi.org/10.1016/j.snb.2012.07.092. URL http://www.sciencedirect.com/science/article/pii/S092540051200785X. 12

[62] K. S. Novoselov, A. K. Geim, S. V. Morozov, D. Jiang, Y. Zhang, S. V. Dubonos, I. V. Grigorieva, and A. A. Firsov. Electric field effect in atomically thin carbon films. *Science*, 306(5696):666–669, 2004. doi: 10.1126/science.1102896. URL http://www.sciencemag.org/content/306/5696/666.abstract. 13, 17, 18, 20, 39

[63] Sungjin Park and Rodney S Ruoff. Chemical methods for the production of graphenes. *Nature nanotechnology*, 4(4):217–24, April 2009. ISSN 1748-3395. doi: 10.1038/nnano.2009.58. URL http://www.ncbi.nlm.nih.gov/pubmed/19350030. 14

[64] Minzhen Cai, Daniel Thorpe, Douglas H. Adamson, and Hannes C. Schniepp. Methods of graphite exfoliation. *J. Mater. Chem.*, 22:24992–25002, 2012. doi: 10.1039/C2JM34517J. URL http://dx.doi.org/10.1039/C2JM34517J. 14, 15

[65] Hannes C. Schniepp, Je-Luen Li, Michael J. McAllister, Hiroaki Sai, Margarita Herrera-Alonso, Douglas H. Adamson, Robert K. Prud'homme, Roberto Car, Dudley A. Saville, and Ilhan A. Aksay. Functionalized single graphene sheets derived from splitting graphite oxide. *The Journal of Physical Chemistry B*, 110(17):8535–8539, 2006. doi: 10.1021/jp060936f. URL http://pubs.acs.org/doi/abs/10.1021/jp060936f. 14, 15

[66] Michael J. McAllister, Je-Luen Li, Douglas H. Adamson, Hannes C. Schniepp, Ahmed A. Abdala, Jun Liu, Margarita Herrera-Alonso, David L. Milius, Roberto Car, Robert K. Prud'homme, and Ilhan A. Aksay. Single sheet functionalized graphene by oxidation and thermal expansion of graphite. *Chemistry of Materials*, 19(18):4396–4404, 2007. doi: 10.1021/cm0630800. URL http://pubs.acs.org/doi/abs/10.1021/cm0630800. 14, 15

[67] Nan Zhu, Wen Liu, Mianqi Xue, Zhuang Xie, Dan Zhao, Meining Zhang, Jitao Chen, and Tingbing Cao. Graphene as a conductive additive to enhance the high-rate capabilities of electrospun li4ti5o12 for lithium-ion batteries. *Electrochimica Acta*, 55(20):5813 – 5818, 2010. ISSN 0013-4686. doi: http://dx.doi.org/10.1016/j.electacta.2010.05.029. URL http://www.sciencedirect.com/science/article/pii/S0013468610007085. 15

[68] M. Lenner, A. Kaplan, Ch. Huchon, and R. E. Palmer. Ultrafast laser ablation of graphite. *Phys. Rev. B*, 79:184105, May 2009. doi: 10.1103/PhysRevB.79.184105. URL http://link.aps.org/doi/10.1103/PhysRevB.79.184105. 16

[69] Ramani K. Raman, Yoshie Murooka, Chong-Yu Ruan, Teng Yang, Savas Berber, and David Tománek. Direct observation of optically induced transient structures in graphite using ultrafast electron crystallography. *Phys. Rev. Lett.*, 101:077401, Aug 2008. doi: 10.1103/PhysRevLett.101.077401. URL http://link.aps.org/doi/10.1103/PhysRevLett.101.077401.

[70] Fabrizio Carbone, Peter Baum, Petra Rudolf, and Ahmed H. Zewail. Structural preablation dynamics of graphite observed by ultrafast electron crystallography. *Phys. Rev. Lett.*, 100:035501, Jan 2008. doi: 10.1103/PhysRevLett.100.035501. URL http://link.aps.org/doi/10.1103/PhysRevLett.100.035501. 16

[71] Yoshiyuki Miyamoto, Hong Zhang, and David Tománek. Photoexfoliation of graphene from graphite: An *Ab Initio* study. *Phys. Rev. Lett.*, 104:208302, May 2010. doi: 10.1103/PhysRevLett.104.208302. URL http://link.aps.org/doi/10.1103/PhysRevLett.104.208302. 16

[72] A.R. Ubbelohde and F.A. Lewis. *Graphite and its crystal compounds*. Clarendon Press, 1960. URL http://books.google.es/books?id=2URCAQAAIAAJ. 17

[73] T.E. Thompson, E.R. Falardeau, and L.R. Hanlon. The electrical conductivity and optical reflectance of graphite-sbf5 compounds. *Carbon*, 15(1):39 – 43, 1977. ISSN

0008-6223. doi: http://dx.doi.org/10.1016/0008-6223(77)90072-0. URL http://www.sciencedirect.com/science/article/pii/0008622377900720. 17

[74] O. A. Shenderova, V. V. Zhirnov, and D. W. Brenner. Carbon nanostructures. *Critical Reviews in Solid State and Materials Sciences*, 27(3-4):227–356, 2002. doi: 10.1080/10408430208500497. URL http://www.tandfonline.com/doi/abs/10.1080/10408430208500497. 17

[75] a K Geim and K S Novoselov. The rise of graphene. *Nature materials*, 6(3):183–91, March 2007. ISSN 1476-1122. doi: 10.1038/nmat1849. URL http://www.ncbi.nlm.nih.gov/pubmed/17330084. 18, 19

[76] Andrey K. Geim and Allan H. MacDonald. Graphene: Exploring carbon flatland. *Physics Today*, 60(8):35–41, 2007. doi: 10.1063/1.2774096. URL http://link.aip.org/link/?PTO/60/35/1.

[77] A. K. Geim. Graphene: Status and prospects. *Science*, 324(5934):1530–1534, 2009. doi: 10.1126/science.1158877. URL http://www.sciencemag.org/content/324/5934/1530.abstract.

[78] S. Reich, C. Thomsen, and J. Maultzsch. *Carbon Nanotubes: Basic Concepts and Physical Properties*. Wiley, 2004. ISBN 9783527403868. URL http://books.google.es/books?id=w_xpdFx0C4MC. 19

[79] D.S.L. Abergel, V. Apalkov, J. Berashevich, K. Ziegler, and Tapash Chakraborty. Properties of graphene: a theoretical perspective. *Advances in Physics*, 59(4):261–482, 2010. doi: 10.1080/00018732.2010.487978. URL http://www.tandfonline.com/doi/abs/10.1080/00018732.2010.487978. 19

[80] F. Guinea, A. H. Castro Neto, and N. M. R. Peres. Electronic states and landau levels in graphene stacks. *Phys. Rev. B*, 73:245426, Jun 2006. doi: 10.1103/PhysRevB.73.245426. URL http://link.aps.org/doi/10.1103/PhysRevB.73.245426. 21

[81] Johan Nilsson, A. H. Castro Neto, F. Guinea, and N. M. R. Peres. Electronic properties of bilayer and multilayer graphene. *Phys. Rev. B*, 78:045405, Jul 2008. doi: 10.1103/PhysRevB.78.045405. URL http://link.aps.org/doi/10.1103/PhysRevB.78.045405.

[82] Z. Q. Li, E. A. Henriksen, Z. Jiang, Z. Hao, M. C. Martin, P. Kim, H. L. Stormer, and D. N. Basov. Band structure asymmetry of bilayer graphene revealed by infrared spectroscopy. *Phys. Rev. Lett.*, 102:037403, Jan 2009. doi: 10.1103/PhysRevLett.102.037403. URL http://link.aps.org/doi/10.1103/PhysRevLett.102.037403. 21

[83] E. McCann and M. Koshino. The electronic properties of bilayer graphene. *Reports on Progress in Physics*, 76(5):056503, May 2013. doi: 10.1088/0034-4885/76/5/056503. 21

[84] M. S. Dresselhaus and G. Dresselhaus. Intercalation compounds of graphite. *Advances in Physics*, 51(1):1–186, 2002. doi: 10.1080/00018730110113644. URL http://www.tandfonline.com/doi/abs/10.1080/00018730110113644. 21

[85] A. Matulis and F. M. Peeters. Quasibound states of quantum dots in single and bilayer graphene. *Phys. Rev. B*, 77:115423, Mar 2008. doi: 10.1103/PhysRevB.77.115423. URL http://link.aps.org/doi/10.1103/PhysRevB.77.115423. 21

[86] Eduardo V. Castro, K. S. Novoselov, S. V. Morozov, N. M. R. Peres, J. M. B. Lopes dos Santos, Johan Nilsson, F. Guinea, A. K. Geim, and A. H. Castro Neto. Biased bilayer graphene: Semiconductor with a gap tunable by the electric field effect. *Phys. Rev. Lett.*, 99:216802, Nov 2007. doi: 10.1103/PhysRevLett.99.216802. URL http://link.aps.org/doi/10.1103/PhysRevLett.99.216802. 22

[87] Taisuke Ohta, Aaron Bostwick, Thomas Seyller, Karsten Horn, and Eli Rotenberg. Controlling the electronic structure of bilayer graphene. *Science*, 313(5789):951–954, 2006. doi: 10.1126/science.1130681. URL http://www.sciencemag.org/content/313/5789/951.abstract. 22

[88] Keun Su Kim, Andrew L Walter, Luca Moreschini, Thomas Seyller, Karsten Horn, Eli Rotenberg, and Aaron Bostwick. Coexisting massive and massless Dirac fermions in symmetry-broken bilayer graphene. *Nature materials*, 12(10):887–892, July 2013. ISSN 1476-1122. doi: 10.1038/nmat3717. URL http://www.ncbi.nlm.nih.gov/pubmed/23892785. 22

[89] J. J. Palacios, J. Fernández-Rossier, and L. Brey. Vacancy-induced magnetism in graphene and graphene ribbons. *Phys. Rev. B*, 77:195428, May 2008. doi: 10.1103/PhysRevB.77.195428. URL http://link.aps.org/doi/10.1103/PhysRevB.77.195428. 23, 63

[90] Oleg V. Yazyev and Lothar Helm. Defect-induced magnetism in graphene. *Phys. Rev. B*, 75:125408, Mar 2007. doi: 10.1103/PhysRevB.75.125408. URL http://link.aps.org/doi/10.1103/PhysRevB.75.125408. 23

[91] David Soriano, Nicolas Leconte, Pablo Ordejón, Jean-Christophe Charlier, Juan-Jose Palacios, and Stephan Roche. Magnetoresistance and magnetic ordering fingerprints in hydrogenated graphene. *Phys. Rev. Lett.*, 107:016602, Jun 2011. doi: 10.1103/PhysRevLett.107.016602. URL http://link.aps.org/doi/10.1103/PhysRevLett.107.016602. 23

[92] Hong-Xin Yang, Mairbek Chshiev, Danil W. Boukhvalov, Xavier Waintal, and Stephan Roche. Inducing and optimizing magnetism in graphene nanomeshes. *Phys. Rev. B*, 84:214404, Dec 2011. doi: 10.1103/PhysRevB.84.214404. URL http://link.aps.org/doi/10.1103/PhysRevB.84.214404. 23

[93] Paolo Sessi, Jeffrey R Guest, Matthias Bode, and Nathan P Guisinger. Patterning graphene at the nanometer scale via hydrogen desorption. *Nano letters*, 9(12):4343–7, December 2009. ISSN 1530-6992. doi: 10.1021/nl902605t. URL http://www.ncbi.nlm.nih.gov/pubmed/19883050. 23

[94] D Haberer, D V Vyalikh, S Taioli, B Dora, M Farjam, J Fink, D Marchenko, T Pichler, K Ziegler, S Simonucci, M S Dresselhaus, M Knupfer, B Büchner, and a Grüneis. Tunable band gap in hydrogenated quasi-free-standing graphene. *Nano letters*, 10(9):3360–6, September 2010. ISSN 1530-6992. doi: 10.1021/nl101066m. URL http://www.ncbi.nlm.nih.gov/pubmed/20695447.

[95] Ming Yang, Argo Nurbawono, Chun Zhang, and Yuan Ping Feng. Two-dimensional graphene superlattice made with partial hydrogenation. *Applied Physics Letters*, 96 (19):193115, 2010. ISSN 00036951. doi: 10.1063/1.3425664. URL http://link.aip.org/link/APPLAB/v96/i19/p193115/s1&Agg=doi.

[96] Richard Balog, Bjarke Jø rgensen, Louis Nilsson, Mie Andersen, Emile Rienks, Marco Bianchi, Mattia Fanetti, Erik Laegsgaard, Alessandro Baraldi, Silvano Lizzit, Zeljko Sljivancanin, Flemming Besenbacher, Bjø rk Hammer, Thomas G Pedersen, Philip Hofmann, and Liv Hornekaer. Bandgap opening in graphene induced by patterned hydrogen adsorption. *Nature materials*, 9(4):315–9, April 2010. ISSN 1476-1122. doi: 10.1038/nmat2710. URL http://www.ncbi.nlm.nih.gov/pubmed/20228819. 23

[97] J Zhou, Q Wang, Q Sun, X S Chen, Y Kawazoe, and P Jena. Ferromagnetism in semihydrogenated graphene sheet. *Nano letters*, 9(11):3867–70, November 2009. ISSN 1530-6992. doi: 10.1021/nl9020733. URL http://www.ncbi.nlm.nih.gov/pubmed/19719081. 23

[98] D. Soriano, F. Muñoz Rojas, J. Fernández-Rossier, and J. J. Palacios. Hydrogenated graphene nanoribbons for spintronics. *Phys. Rev. B*, 81:165409, Apr 2010. doi: 10.1103/PhysRevB.81.165409. URL http://link.aps.org/doi/10.1103/PhysRevB.81.165409. 23

[99] P. O. Lehtinen, A. S. Foster, A. Ayuela, A. Krasheninnikov, K. Nordlund, and R. M. Nieminen. Magnetic properties and diffusion of adatoms on a graphene sheet. *Phys. Rev. Lett.*, 91:017202, Jun 2003. doi: 10.1103/PhysRevLett.91.017202. URL http://link.aps.org/doi/10.1103/PhysRevLett.91.017202. 23

[100] D. W. Boukhvalov, M. I. Katsnelson, and A. I. Lichtenstein. Hydrogen on graphene: Electronic structure, total energy, structural distortions and magnetism from first-principles calculations. *Phys. Rev. B*, 77:035427, Jan 2008. doi: 10.1103/PhysRevB.77.035427. URL http://link.aps.org/doi/10.1103/PhysRevB.77.035427. 23

[101] Simone Casolo, Ole Martin Lvvik, Rocco Martinazzo, and Gian Franco Tantardini. Understanding adsorption of hydrogen atoms on graphene. *The Journal of chemical physics*, 130(5):054704, February 2009. ISSN 1089-7690. doi: 10.1063/1.3072333. URL http://www.ncbi.nlm.nih.gov/pubmed/19206986. 23, 59

[102] Elliott H. Lieb. Two theorems on the hubbard model. *Phys. Rev. Lett.*, 62:1201–1204, Mar 1989. doi: 10.1103/PhysRevLett.62.1201. URL http://link.aps.org/doi/10.1103/PhysRevLett.62.1201. 23, 59

[103] P. Esquinazi, D. Spemann, R. Höhne, A. Setzer, K.-H. Han, and T. Butz. Induced magnetic ordering by proton irradiation in graphite. *Phys. Rev. Lett.*, 91:227201, Nov 2003. doi: 10.1103/PhysRevLett.91.227201. URL http://link.aps.org/doi/10.1103/PhysRevLett.91.227201. 24

[104] M. A. Ramos, J. Barzola-Quiquia, P. Esquinazi, A. Muñoz Martin, A. Climent-Font, and M. García-Hernández. Magnetic properties of graphite irradiated with mev ions. *Phys. Rev. B*, 81:214404, Jun 2010. doi: 10.1103/PhysRevB.81.214404. URL http://link.aps.org/doi/10.1103/PhysRevB.81.214404.

[105] M. M. Ugeda, I. Brihuega, F. Guinea, and J. M. Gómez-Rodríguez. Missing atom as a source of carbon magnetism. *Phys. Rev. Lett.*, 104:096804, Mar 2010. doi: 10.1103/PhysRevLett.104.096804. URL http://link.aps.org/doi/10.1103/PhysRevLett.104.096804. 24

[106] L. Pauling. *The Nature of the Chemical Bond and the Structure of Molecules and Crystals: An Introduction to Modern Structural Chemistry*. George Fisher Baker Non-resident Lectureship in Chemistry at Cornell University. Cornell University Press, 1960. ISBN 9780801403330. URL http://books.google.es/books?id=L-1K9HmKmUUC. 24

[107] Oleg V. Yazyev. Magnetism in disordered graphene and irradiated graphite. *Phys. Rev. Lett.*, 101:037203, Jul 2008. doi: 10.1103/PhysRevLett.101.037203. URL http://link.aps.org/doi/10.1103/PhysRevLett.101.037203. 24

[108] P. Hohenberg and W. Kohn. Inhomogeneous electron gas. *Phys. Rev.*, 136:B864–B871, Nov 1964. doi: 10.1103/PhysRev.136.B864. URL http://link.aps.org/doi/10.1103/PhysRev.136.B864. 25, 26, 71, 101

[109] W. Kohn and L. J. Sham. Self-consistent equations including exchange and correlation effects. *Phys. Rev.*, 140:A1133–A1138, November 1965. doi: 10.1103/PhysRev.140.A1133. URL http://link.aps.org/doi/10.1103/PhysRev.140.A1133. 28, 32, 71, 101

[110] R.G. Parr and W. Yang. *Density-Functional Theory of Atoms and Molecules*. International Series of Monographs on Chemistry. Oxford University Press, 1994. ISBN 9780195092769. URL http://books.google.fr/books?id=mGOpScSIwU4C. 25

[111] R.M. Martin. *Electronic Structure: Basic Theory and Practical Methods*. Cambridge University Press, 2004. ISBN 9780521782852. URL http://books.google.es/books?id=dmRTFLpSGNsC. 27, 30, 32, 35

[112] Yingkai Zhang and Weitao Yang. Comment on "generalized gradient approximation made simple". *Phys. Rev. Lett.*, 80:890–890, Jan 1998. doi: 10.1103/PhysRevLett.80.890. URL http://link.aps.org/doi/10.1103/PhysRevLett.80.890. 32, 33

[113] M. Dion, H. Rydberg, E. Schröder, D. C. Langreth, and B. I. Lundqvist. Van der waals density functional for general geometries. *Phys. Rev. Lett.*, 92(24):246401, June 2004. doi: 10.1103/PhysRevLett.92.246401. 33, 35

[114] D C Langreth, B I Lundqvist, S D Chakarova-Käck, V R Cooper, M Dion, P Hyldgaard, a Kelkkanen, J Kleis, Lingzhu Kong, Shen Li, P G Moses, E Murray, a Puzder, H Rydberg, E Schröder, and T Thonhauser. A density functional for sparse matter. *Journal of physics. Condensed matter : an Institute of Physics journal*, 21(8): 084203, February 2009. ISSN 0953-8984. doi: 10.1088/0953-8984/21/8/084203. URL http://www.ncbi.nlm.nih.gov/pubmed/21817355. 33

[115] T. Thonhauser, Valentino R. Cooper, Shen Li, Aaron Puzder, Per Hyldgaard, and David C. Langreth. Van der waals density functional: Self-consistent potential and the nature of the van der waals bond. *Phys. Rev. B*, 76:125112, Sep 2007. doi: 10.1103/PhysRevB.76.125112. URL http://link.aps.org/doi/10.1103/PhysRevB.76.125112. 34

[116] Kristian Berland. *Bound by long-range interactions: Molecular crystals and benzene on Cu(111)*. Chalmers University of Technology, 2009. 35

[117] ArthurF. Voter. Introduction to the kinetic monte carlo method. In KurtE. Sickafus, EugeneA. Kotomin, and BlasP. Uberuaga, editors, *Radiation Effects in Solids*, volume 235 of *NATO Science Series*, pages 1–23. Springer Netherlands, 2007. ISBN 978-1-4020-5293-4. doi: 10.1007/978-1-4020-5295-8_1. URL http://dx.doi.org/10.1007/978-1-4020-5295-8_1. 36

[118] A.B. Bortz, M.H. Kalos, and J.L. Lebowitz. A new algorithm for monte carlo simulation of ising spin systems. *Journal of Computational Physics*, 17(1):10 – 18, 1975. ISSN 0021-9991. doi: http://dx.doi.org/10.1016/0021-9991(75)90060-1. URL http://www.sciencedirect.com/science/article/pii/0021999175900601. 36

[120] Guohong Li, Adina Luican, and Eva Y. Andrei. Scanning tunneling spectroscopy of graphene on graphite. *Phys. Rev. Lett.*, 102:176804, Apr 2009. doi: 10.1103/PhysRevLett.102.176804. URL http://link.aps.org/doi/10.1103/PhysRevLett.102.176804. 39

[121] T. R. Albrecht, M. M. Dovek, M. D. Kirk, C. A. Lang, C. F. Quate, and D. P. E. Smith. Nanometerscale hole formation on graphite using a scanning tunneling microscope. *Applied Physics Letters*, 55(17), 1989. 40

[122] Seiichi Kondo, Mark Lutwyche, and Yasuo Wada. Nanofabrication of layered materials with the scanning tunneling microscope. *Applied Surface Science*, 75(1–4):39 – 44, 1994. ISSN 0169-4332. doi: http://dx.doi.org/10.1016/0169-4332(94)90133-3. URL http://www.sciencedirect.com/science/article/pii/0169433294901333. 40

[123] Hidefumi Hiura. Tailoring graphite layers by scanning tunneling microscopy. *Applied Surface Science*, 222(1–4):374 – 381, 2004. ISSN 0169-4332. doi: http://dx.doi.org/10.1016/j.apsusc.2003.09.004. URL http://www.sciencedirect.com/science/article/pii/S0169433203011383. 40

[124] D. M. Eigler and E. K. Schweizer. Positioning single atoms with a scanning tunnelling microscope. *Nature*, 344(6266):524–526, 1990. doi: 10.1038/344524a0. URL http://dx.doi.org/10.1038/344524a0. 40

[125] P. Xu, Yurong Yang, D. Qi, S. D. Barber, J. K. Schoelz, M. L. Ackerman, L. Bellaiche, and P. M. Thibado. Electronic transition from graphite to graphene via controlled movement of the top layer with scanning tunneling microscopy. *Phys. Rev. B*, 86:085428, Aug 2012. doi: 10.1103/PhysRevB.86.085428. URL http://link.aps.org/doi/10.1103/PhysRevB.86.085428. 40

[126] D.E. Sands. *Introduction to Crystallography*. Dover Classics of Science and Mathematics. Dover Publications, 1994. ISBN 9780486678399. URL http://books.google.es/books?id=h_A5u5sczJoC. 42

[127] J. W. McClure. Band structure of graphite and de haas-van alphen effect. *Phys. Rev.*, 108:612–618, Nov 1957. doi: 10.1103/PhysRev.108.612. URL http://link.aps.org/doi/10.1103/PhysRev.108.612. 42

[128] S. Reich, J. Maultzsch, C. Thomsen, and P. Ordejón. Tight-binding description of graphene. *Phys. Rev. B*, 66:035412, Jul 2002. doi: 10.1103/PhysRevB.66.035412. URL http://link.aps.org/doi/10.1103/PhysRevB.66.035412. 42

[129] Sylvain Latil and Luc Henrard. Charge carriers in few-layer graphene films. *Phys. Rev. Lett.*, 97:036803, Jul 2006. doi: 10.1103/PhysRevLett.97.036803. URL http://link.aps.org/doi/10.1103/PhysRevLett.97.036803. 43

[130] Hongki Min, Bhagawan Sahu, Sanjay K. Banerjee, and A. H. MacDonald. *Ab initio* theory of gate induced gaps in graphene bilayers. *Phys. Rev. B*, 75:155115, Apr 2007. doi: 10.1103/PhysRevB.75.155115. URL http://link.aps.org/doi/10.1103/PhysRevB.75.155115. 43

[131] R. C. Tatar and S. Rabii. Electronic properties of graphite: A unified theoretical study. *Phys. Rev. B*, 25:4126–4141, Mar 1982. doi: 10.1103/PhysRevB.25.4126. URL http://link.aps.org/doi/10.1103/PhysRevB.25.4126. 43

[132] R. Ahuja, S. Auluck, J. M. Wills, M. Alouani, B. Johansson, and O. Eriksson. Optical properties of graphite from first-principles calculations. *Phys. Rev. B*, 55:4999–5005, Feb 1997. doi: 10.1103/PhysRevB.55.4999. URL http://link.aps.org/doi/10.1103/PhysRevB.55.4999. 43

[133] Xianwei Sha and Bret Jackson. First-principles study of the structural and energetic properties of H atoms on a graphite () surface. *Surface Science*, 496(3):318–330, January 2002. ISSN 00396028. doi: 10.1016/S0039-6028(01)01602-8. URL http://linkinghub.elsevier.com/retrieve/pii/S0039602801016028. 59

[134] V. V. Ivanovskaya, a. Zobelli, D. Teillet-Billy, N. Rougeau, V. Sidis, and P. R. Briddon. Hydrogen adsorption on graphene: a first principles study. *The European Physical Journal B*, 76(3):481–486, August 2010. ISSN 1434-6028. doi: 10.1140/epjb/e2010-00238-7. URL http://www.springerlink.com/index/10.1140/epjb/e2010-00238-7. 59

[135] Z Sljivancanin, E Rauls, L Hornekaer, W Xu, F Besenbacher, and B Hammer. Extended atomic hydrogen dimer configurations on the graphite(0001) surface. *The Journal of chemical physics*, 131(8):084706, August 2009. ISSN 1089-7690. doi: 10.1063/1.3187941. URL http://www.ncbi.nlm.nih.gov/pubmed/19725620. 59

[136] Jay Kerwin and Bret Jackson. The sticking of H and D atoms on a graphite (0001) surface: the effects of coverage and energy dissipation. *The Journal of chemical physics*, 128(8):084702, February 2008. ISSN 0021-9606. doi: 10.1063/1.2868771. URL http://www.ncbi.nlm.nih.gov/pubmed/18315067. 59

[137] Pablo a. Denis and Federico Iribarne. On the hydrogen addition to graphene. *Journal of Molecular Structure: THEOCHEM*, 907(1-3):93–103, August 2009. ISSN 01661280. doi: 10.1016/j.theochem.2009.04.028. URL http://linkinghub.elsevier.com/retrieve/pii/S0166128009002930. 59

[138] Elizabeth J. Duplock, Matthias Scheffler, and Philip J. D. Lindan. Hallmark of perfect graphene. *Phys. Rev. Lett.*, 92:225502, Jun 2004. doi: 10.1103/PhysRevLett.92.225502. URL http://link.aps.org/doi/10.1103/PhysRevLett.92.225502. 59

[139] L. Hornekær, E. Rauls, W. Xu, Ž. Šljivančanin, R. Otero, I. Stensgaard, E. Lægsgaard, B. Hammer, and F. Besenbacher. Clustering of chemisorbed h(d) atoms on the graphite (0001) surface due to preferential sticking. *Phys. Rev. Lett.*, 97:186102, Oct 2006. doi: 10.1103/PhysRevLett.97.186102. URL http://link.aps.org/doi/10.1103/PhysRevLett.97.186102. 59

[140] L. Chen, a.C. Cooper, G.P. Pez, and H. Cheng. Mechanistic Study on Hydrogen Spillover onto Graphitic Carbon Materials. *Journal of Physical Chemistry C*, 111(51): 18995–19000, December 2007. ISSN 1932-7447. doi: 10.1021/jp074920g. URL http://pubs.acs.org/cgi-bin/doilookup/?10.1021/jp074920g. 59

[141] J. J. Palacios and F. Ynduráin. Critical analysis of vacancy-induced magnetism in monolayer and bilayer graphene. *Phys. Rev. B*, 85:245443, Jun 2012. doi: 10.1103/PhysRevB.85.245443. URL http://link.aps.org/doi/10.1103/PhysRevB.85.245443. 60, 69

[142] Robert G. Parr and Weitao Yang. Density-functional theory of the electronic structure of molecules. *Annual Review of Physical Chemistry*, 46(1):701–728, 1995. doi: 10.1146/annurev.pc.46.100195.003413. URL http://www.annualreviews.org/doi/abs/10.1146/annurev.pc.46.100195.003413. PMID: 24341393. 71

[143] Yuji Matsumoto, Makoto Murakami, Tomoji Shono, Tetsuya Hasegawa, Tomoteru Fukumura, Masashi Kawasaki, Parhat Ahmet, Toyohiro Chikyow, Shin-ya Koshihara, and Hideomi Koinuma. Room-temperature ferromagnetism in transparent transition metal-doped titanium dioxide. *Science*, 291(5505):854–856, 2001. doi: 10.1126/science.1056186. URL http://www.sciencemag.org/content/291/5505/854.abstract. 71

[144] K. Binder. Finite size scaling analysis of ising model block distribution functions. *Zeitschrift für Physik B Condensed Matter*, 43(2):119–140, 1981. ISSN 0722-3277. doi: 10.1007/BF01293604. URL http://dx.doi.org/10.1007/BF01293604. 74

[145] K. Binder. Critical properties from monte carlo coarse graining and renormalization. *Phys. Rev. Lett.*, 47:693–696, Aug 1981. doi: 10.1103/PhysRevLett.47.693. URL http://link.aps.org/doi/10.1103/PhysRevLett.47.693. 74

[146] Željko Šljivančanin, Mie Andersen, Liv Hornekær, and Bjørk Hammer. Structure and stability of small h clusters on graphene. *Phys. Rev. B*, 83:205426, May 2011. doi: 10.1103/PhysRevB.83.205426. URL http://link.aps.org/doi/10.1103/PhysRevB.83.205426. 83

[147] Pablo Ordejón, Emilio Artacho, and José M. Soler. Self-consistent order-*n* density-functional calculations for very large systems. *Phys. Rev. B*, 53:R10441–R10444, Apr 1996. doi: 10.1103/PhysRevB.53.R10441. URL http://link.aps.org/doi/10.1103/PhysRevB.53.R10441. 101

[148] José M Soler, Emilio Artacho, Julian D Gale, Alberto García, Javier Junquera, Pablo Ordejón, and Daniel Sánchez-Portal. The siesta method for ab initio order- n materials simulation. *Journal of Physics: Condensed Matter*, 14(11):2745, 2002. URL http://stacks.iop.org/0953-8984/14/i=11/a=302. 101

[149] M. Dion, H. Rydberg, E. Schröder, D. C. Langreth, and B. I. Lundqvist. Van der waals density functional for general geometries. *Phys. Rev. Lett.*, 92:246401, Jun 2004. doi: 10.1103/PhysRevLett.92.246401. URL http://link.aps.org/doi/10.1103/PhysRevLett.92.246401. 101

[150] Guillermo Román-Pérez and José M. Soler. Efficient implementation of a van der waals density functional: Application to double-wall carbon nanotubes. *Phys. Rev. Lett.*, 103: 096102, Aug 2009. doi: 10.1103/PhysRevLett.103.096102. URL http://link.aps.org/doi/10.1103/PhysRevLett.103.096102. 101

[151] Lingzhu Kong, Guillermo Román-Pérez, José M. Soler, and David C. Langreth. Energetics and dynamics of $\mathbf{h}_2$ adsorbed in a nanoporous material at low temperature. *Phys. Rev. Lett.*, 103:096103, Aug 2009. doi: 10.1103/PhysRevLett.103.096103. URL http://link.aps.org/doi/10.1103/PhysRevLett.103.096103. 101

[152] N. Troullier and José Luriaas Martins. Efficient pseudopotentials for plane-wave calculations. *Phys. Rev. B*, 43:1993–2006, Jan 1991. doi: 10.1103/PhysRevB.43.1993. URL http://link.aps.org/doi/10.1103/PhysRevB.43.1993. 101

[153] Javier Junquera, Óscar Paz, Daniel Sánchez-Portal, and Emilio Artacho. Numerical atomic orbitals for linear-scaling calculations. *Phys. Rev. B*, 64:235111, Nov 2001. doi: 10.1103/PhysRevB.64.235111. URL http://link.aps.org/doi/10.1103/PhysRevB.64.235111. 101

[154] G. Makov and M. C. Payne. Periodic boundary conditions in ab initio calculations. *Phys. Rev. B*, 51:4014–4022, Feb 1995. doi: 10.1103/PhysRevB.51.4014. URL http://link.aps.org/doi/10.1103/PhysRevB.51.4014. 102